

Supplementary Materials for

Bimaterial effect and favorable energy ratio enabled supershear rupture in the 2025 Mandalay earthquake

Liuwei Xu *et al.*

Corresponding author: Lingsen Meng, lsmeng@g.ucla.edu

Science **390**, 476 (2025)
DOI: 10.1126/science.ady6100

The PDF file includes:

Materials and Methods
Figs. S1 to S40
Tables S1 to S6
References

Other Supplementary Material for this manuscript includes the following:

Movies S1 to S4

Materials and Methods

Slowness-Enhanced Back-Projection

The Back-Projection (BP) method images earthquake rupture propagation using seismograms recorded by large-aperture arrays with dense station coverage (76, 77, 78). This study employed the Slowness-Enhanced Back-Projection (SEBP) method, following the approach developed by (7, 79). Compared to standard BP, SEBP provided a more accurate reconstruction of the rupture process. For the Mandalay earthquake, the Alaska (AK), Australia (AU), and Europe (EU) arrays, located at teleseismic distances (30° – 90°), were well-suited for SEBP analysis. We collected vertical-component broadband seismograms (BHZ) from 176 AK stations, 349 EU stations, and 151 AU stations. Each array's waveforms were first automatically aligned according to the P-wave travel times from the hypocenter to stations predicted by a 1D Earth model. Residual travel time errors were then manually corrected to ensure the first P arrival corresponded to the hypocenter. In the BP process, the aligned waveforms were band-pass filtered to 0.5–2 Hz, optimizing the balance between resolution and signal-to-noise ratio. The filtered waveforms were then analyzed using the MUSIC BP algorithm (7, 78) to resolve the spatiotemporal evolution of high-frequency (HF) radiators during the mainshock.

The alignment described above accounted for travel time errors caused by deviations of Earth's 3D structure from the simplified 1D Earth model. However, this correction was only valid for the wave path between the hypocenter and the stations. Given that the Mandalay earthquake ruptured over 500 km along the Sagaing Fault, the wave propagation path changed significantly as the rupture extended away from the hypocenter, reducing the effectiveness of the initial alignment. To accurately correct travel time errors across the entire source region, our SEBP method incorporated 5 to 8 aftershocks distributed along the Sagaing Fault (table S4) to derive additional slowness correction terms for the three arrays (figs. S1, S3, and S5). These corrections were then applied to the mainshock BP results to ensure more accurate travel time calibration. After applying the slowness calibrations, the root mean square (RMS) distance between BP-inferred aftershock locations and those in the National Earthquake Information Center (NEIC) catalog decreased from \sim 20 km to \sim 10 km (table S4). We further verified the effectiveness of the slowness calibration by applying the derived correction terms to 3–4 aftershocks not used in the

derivation process (table S5). The spatial mislocations for these aftershocks were also significantly reduced (figs. S7–S9). These reductions indicate that the BP analysis is less affected by travel time errors, resulting in a more accurate depiction of the rupture process (Figs. 1 and S1–S6).

In the BP results from the EU array, several HF radiators in the northern branch extended beyond the mapped fault traces, reaching as far as 23.5°N (fig. S5a). At this latitude, no corresponding radiators were observed in the AU array (fig. S3a), and only weak signals appeared in the AK array (fig. S1a). This discrepancy likely arises from the different azimuths of the arrays: EU is located northwest of the epicenter, AK to the northeast, and AU to the southeast. We propose that these northern radiators may correspond to a coseismically triggered, small-magnitude event that did not produce surface rupture but emitted high-frequency radiation, similar to those observed in the 2011 Tohoku and 2023 Turkey earthquakes (80, 17). To focus on main coseismic features consistently resolved across all arrays and supported by the finite fault inversion results, we excluded radiators north of the epicenter that appeared after 40 seconds in the mainshock BP image. After this adjustment, the distribution of BP radiators became more consistent across the three arrays (Figs. 1 and S1–S6) and aligned well with both the surface rupture traces (Fig. 1) and the joint FFI model. We note that including those northern radiators into the rupture speed estimation increases the inferred speed but still yields a subshear value (2.48 km/s; fig. S33).

The final BP radiators' spatial distribution is depicted in Fig. 1A and figs. S1–S6. To obtain the rupture speeds shown in Fig. 1C, we calculated the BP radiators' along-fault distances while accounting for the strike changes in the fault model of Fig. 2C. The calculations are as follows:

For BP radiators inside segment 1:

Along-fault distance = epicenter distance * cos[radiator's azimuth (relative to the epicenter) - segment 1 azimuth].

For BP radiators inside segment 2:

Along-fault distance = distance to the north edge of segment 2 * cos[radiator's azimuth (relative to the north edge of segment 2) - segment 2 azimuth] + the south edge of segment 1's epicenter distance.

For BP radiators inside segment 3:

Along-fault distance = distance to the north edge of segment 3 * cos[radiator's azimuth (relative to the north edge of segment 3) - segment 3 azimuth] + the south edge of segment 1's epicenter distance + segment 2' length.

In Fig. 1C, we used positive values to indicate distances to the north and negative values to the south. To determine the rupture speed, we merged BP radiators from all arrays into one file,

calculated all radiators' along-fault distances, and identified the leading radiators (the radiators with the furthest along-fault distance at each time) for the north branch and the south branch. The linearly-fitted rupture speeds are 0.9 km/s for the north branch and 5.0 km/s for the south branch, respectively.

Joint Finite Fault Inversion

The joint Finite Fault Inversion (FFI) integrated multiple seismic and geodetic datasets to constrain slip amplitude and distribution, slip rate, rake angles, and rupture progression along the fault. This study adopted the joint FFI method developed by (8, 9, 81). The seismic dataset included recordings from one near-fault station (GE.NPW) along the Sagaing Fault and four regional stations (IU.CHTO, MM.KTN, MM.YGN, MM.NGU; fig. S22), all of which recorded three-component accelerations (vertical-Z, radial-R, transverse-T). These recordings were bandpass filtered to 0.01–0.15 Hz, integrated into velocity seismograms, and incorporated into the inversion (fig. S21). Additionally, the inversion dataset comprised 20 broadband teleseismic P waves (bandpass filtered to 2–333 s; figs. S17-S18), 24 broadband teleseismic S waves (bandpass filtered to 2–333 s; figs. S17-S18), 20 long-period teleseismic Rayleigh waves (bandpass filtered to 166–250 s; figs. S19-S20), and 21 long-period teleseismic Love waves (bandpass filtered to 166–250 s; figs. S19-S20). The geodetic dataset included static ground displacements derived from Sentinel-1, Sentinel-2, ALOS-2, and LuTan-1 satellite images (figs. S14-S16; see SAR Data Processing for further details).

The seismic data were transformed into wavelet domains, enabling simultaneous resolution of high- and low-frequency characteristics while preserving time-domain information (8, 65). Misfits for static ground deformation were calculated using the L₂ norm, with weighted sum-squared residuals quantifying differences between observed and synthetic data. The weighting was inversely proportional to the standard deviation at each data point. Fault surface traces were identified from SAR images (Fig. 2B-C), and the rupture was modeled using three sub-vertical fault planes (segments S1–S3 in Fig. 2C). We initially assigned a uniform dip angle to all three fault segments and assessed how the misfits in both seismic and geodetic datasets varied as a function of dip (fig. S34). Upon inspecting the teleseismic P waveforms, we found that the small initial pulses could only be adequately reproduced using a relatively shallow dipping fault (e.g., dip = 65°; fig. S35). In contrast, the ground deformation near the southern branch was better matched by a steeper dipping fault (fig. S36). Based on the combined analysis of waveform fits and the misfit-versus-dip angle curves (fig. S34), we determined the optimal dip angles to be 65° for segments S1 and S2, and 80° for segment S3. The fault planes were parameterized with 60 subfaults along strike and 15 along dip, with a subfault size of 10 km × 2 km. Laplacian smoothing constraints were applied to fault slip and perturbations in rupture initiation time across subfaults. The hypocenter was set at 21.996°N, 96.026°E, at a depth of 10.0 km, based on the Preliminary Determination of Epicenters by the National Earthquake

Information Center and the surface rupture trace. The rupture velocity was allowed to vary between 1.00 km/s and 6.00 km/s, with a reference speed of 5.1 km/s. The rake angle was constrained within $\pm 40^\circ$ of the reference value of 175.44° , as provided by the Global Centroid Moment Tensor Catalog. Green's functions for local strong motion waveforms and static displacements were computed using the f-k integration approach (82) and the 1-D velocity models. We utilized the shear wave velocity (V_s) models adapted from (5), and estimated the P-wave velocity and rock density using empirical relationships from (83, 84). For this earthquake, the fault lies beneath a sedimentary basin, while two regional strong-motion stations (CHTO and KTN) are located in a mountainous region (fig. S22). Given the high V_s characteristic of the mountainous terrain (5), we computed the Green's functions for these two stations using a high- V_s model (fig. S10b and table S1b). Green's functions for all other strong-motion recordings, teleseismic broadband body waves, and static displacements were calculated using the V_s model presented in fig. S10a and table S1a.

To assess the influence of random seed selection in our simulated annealing inversions and to explore uncertainties arising from multiple optimal solutions within the model space, we performed 10 FFIs for the mainshock, each initialized with a different random seed. All 10 inversions yielded similar results, with negligible standard deviation in objective function values (~0.9% of the average). The mean coseismic slip distribution and the associated standard deviation are shown in fig. S23. Most regions on the fault exhibit minimal variability, except for certain patches on segment 3. Given that all 10 models are plausible, we selected the one with the lowest objective function value as our preferred solution and presented its slip distribution in Fig. 2.

Synthetic Back-Projection

In the SEBP results, the overall supershear rupture speed along the southern branch was consistently confirmed by all three arrays (Fig. 2 and S1b-S6b). However, some small-scale array-dependent variations were observed. For instance, the EU array exhibited apparent back-propagations at ~ 45 and ~ 65 s, while scattered HF radiators appeared in the AU array's results between 60–100 s. As shown in our previous observation and simulation study (13), BP may not accurately recover bilateral rupture branches during the early stages when the separation between branches is insufficient and the signal interference is significant. Moreover, some instances of apparent back-propagation or stagnation could be artifacts (26). To further investigate this, we performed BP on synthetic waveforms generated by summing slip-rate contributions from each subfault and convolving them with the empirical Green's function (EGF). The EGF used was a Mw 5.9 event located in the source region (EGF 1 in table S2). We adopted the fault geometry and slip distribution from the joint inversion model (Fig. 2C), with rupture speeds set at 1 km/s for the northern branch and 5 km/s for the southern branch (figs. S11a and S12a). The slip-rate function followed the Yoffe analytical function (85, 86).

The synthetic BP results (figs. S11–S12) demonstrated that despite a continuous southern rupture in the input model, the HF radiators before 40 s were obscured or distorted in the AU and EU arrays due to interference from the northern rupture. Apparent back-propagations also emerged in these arrays' synthetic results. For the AK array, the southward HF radiators appeared continuous, but their locations before 40 s were offset. Nevertheless, when identifying the leading radiators—those with the greatest epicentral distance at each time—the inferred rupture speeds for the entire process were generally consistent across arrays (fig. S12). For the southern branch, the BP-inferred speeds from the AK, AU, and EU arrays were 4.0 km/s, 4.5 km/s, and 4.6 km/s, respectively. The AK array exhibited the most underestimation, while the EU array provided the most accurate recovery. This underestimation likely results from coda waves emitted by each sub-source, which exhibit gradually decreasing coherence over 5–10 seconds (87). Despite their decay, residual coherence during this window can bias BP source localization. Since BP uses a moving window—typically spanning several cycles of the dominant frequency (e.g., 10 s for the 0.5–2 Hz band)—the imaged source location reflects a spatial average of direct and coda energy. This averaging can cause apparent source positions to lag behind the true rupture front, artificially lowering the inferred rupture speed. The lag trend is consistent with the SEBP results (figs. S2b, S4b, and S6b), where the inferred speeds were 4.8 km/s, 4.9 km/s, and 5.0 km/s for AK, AU, and EU, respectively. These synthetic tests suggest that the EU array yields the most reliable results for the southern branch and confirm its supershear nature, while also implying the actual speed could slightly exceed 5.0 km/s. For the northern branch, the BP-inferred speeds from all three arrays were ~0.7 km/s—lower than the input value of 1 km/s—yet still confirming its subshear character. We also plotted the MUSIC Pseudo-Spectrum (MPS) in fig. S13. This figure was generated by extracting MPS profiles along the fault from all time steps of Movies S1–S3 and ordering them chronologically. The MPS derived from the synthetic BP results closely matches that from the real BP (fig. S13), supporting the validity of our synthetic BP tests.

It is also worth noting that in the early stage of the synthetic BP results (e.g., before 10 or 20 s), both the southern rupture distance and speed were underestimated (fig. S12). This suggests that if supershear rupture is observed during this early stage—such as the ones identified by the EU and AK arrays in actual observations (red diamonds in the first 5 s in fig. S6b and at ~30 s in fig. S2b)—it is highly likely to be genuine. This supports our conclusion that the Mandalay earthquake was a long supershear rupture with an early transition, further corroborated by evidence from finite fault inversion, Mach wave patterns, and GE.NPW station's recordings.

Far-Field Mach Wave Searching

Vallée & Dunham (21) demonstrated that when a rupture propagates faster than the Rayleigh and Love wave speeds, it generates far-field surface wave Mach cones, within which surface waves

from all sections of the supershear rupture arrive simultaneously and interfere constructively. Theoretically, within the Mach cone, bandpassed surface wave seismograms from a large supershear rupture should be identical or highly similar to those from much smaller events with similar focal mechanisms (hereinafter referred to as empirical Green's functions, EGFs). Moreover, the amplitude of observed waveforms from the supershear rupture and the EGF should scale approximately with the ratio of their seismic moments. Since Rayleigh and Love wave speeds are close to the shear wave speed ($V_{\text{Rayleigh}} \approx 0.92V_s$), Mach waves and Mach cones are also considered distinctive features of supershear ruptures.

In this study, the similarities between waveforms are quantitatively measured by standard cross-correlation coefficients (CCs):

$$CC(U, u) = \sum_{i=1}^N U_i u_i / \sqrt{\sum_{i=1}^N U_i U_i \sum_{i=1}^N u_i u_i} \quad (1)$$

, where U and u are the main-shock and EGF event Rayleigh displacement waveforms, respectively. We use θ to denote the angle between the rupture direction and the source-station azimuth. Theory predicts Mach cones at θ_M :

$$\theta_M = \arccos(V_{\text{Rayleigh}}/V_r) \quad (2)$$

, where V_{Rayleigh} is the Rayleigh wave speed and V_r is the rupture speed. The Mach angle θ_M is therefore positively related to V_r . For the rupture with a speed of V_{Rayleigh} , the Mach cone appears in the frontal direction of the rupture with $\theta_M=0$. When V_r increased to $1.5V_{\text{Rayleigh}}$ ($1.38V_s$), θ_M increases to 49° .

One potential complication arises from the fact that the Mach wave theory is based on unilateral rupture models, while the 2025 Mandalay earthquake exhibited bilateral rupture. However, synthetic tests from our prior work on the 2023 Türkiye earthquake (17) demonstrated that for bilateral ruptures, surface waves radiated from the distal rupture branch do not stack constructively at stations located in the proximal direction. Therefore, in the Mandalay earthquake, the northern subshear rupture should have minimal influence on Mach waves recorded at stations south of the epicenter. We collected 76 vertical-component broadband seismic recordings (BHZ) from the IU, II, and AU seismic networks. To satisfy the far-field assumption (21) and avoid waveform simplicity due to small epicentral distances, all selected stations were located beyond 20° (>2200 km). To minimize the effects of surface wave dispersion, seismograms were bandpass filtered to 15–25 s. This period range is shorter than the mainshock duration but longer than the EGF duration, preserving the point-source characteristics of the EGF event while maintaining the finite-source effects of the mainshock rupture. In actual

observations, due to surface wave dispersion and source directivity, highly similar waveforms are observed within an azimuthal range around θ_M . To account for potential travel time errors caused by 3D path effects, we manually picked the Rayleigh wave envelopes for both the mainshock and EGF. CCs were then computed within a 200–300 s window to capture the full envelope of Rayleigh waveforms (Fig. 4C).

SAR Data Processing

We use four pairs of Copernicus Sentinel-1A SAR images (from ascending tracks 70 and 143 and descending tracks 33 and 106; fig. S14a-h), one pair of LuTan-1 SAR images (ascending track 52; fig. S14i-j), two pairs of ALOS-2 ScanSAR images (ascending track 152 and descending track 41; fig. S14k-l), and two pairs of Sentinel-2 optical images (fig. S14m-n) to derive static ground displacements. Detailed data information is summarized in table S6. For Sentinel-1 SAR images, we apply speckle tracking using ISCE-2 (88) to measure the surface deformation in the range direction (radar line-of-sight direction) and azimuth direction (along-track direction). More specifically, we use the “`topsApp.py`” (89) to perform geometric coregistration on the two scenes of Single Look Complex (SLC) images, and refine the azimuth mis-registration through the enhanced spectral diversity technique (90). For the speckle tracking, we first oversample the SLC by a factor of 2, then use a relatively large cross-correlation window of 256 by 128 pixels in the range and azimuth directions (about 1170 by 1800 m on the ground) and an inter-window step size of 64 by 32 pixels, respectively; next we oversample the cross-correlation surface by a factor of 32 to derive the sub-pixel-accuracy displacement and apply a median filter using a window size of 5 pixels (about 1.5 by 2.2 km on the ground) to reduce the estimation noise. We masked out noisy pixels with the following criteria: 1) in the water; 2) offset standard deviation (STD) ≥ 0.5 and 1.5 m in the range and azimuth directions, respectively; 3) offset signal-to-noise ratio (SNR) ≥ 5 and 3 in the range and azimuth directions, respectively. Due to the significant ionospheric influence in this region as observed previously (91, 92) and in the wrapped interferograms (fig. S37), we estimate linear or quadratic ramps using the far-field observation and subtract them from all pixels: we remove a quadratic ramp along the azimuth direction for Sentinel-1 ascending track 70 range offset, a linear ramp along the azimuth direction for Sentinel-1 ascending track 143 range offset, a linear ramp along both range and azimuth directions for Sentinel-1 ascending track 143 azimuth offset, and none for the rest. Finally, we geocode all offsets to a grid with a size of 0.00277778° (~ 300 m) in latitude and longitude.

For LuTan-1 (93) SAR images, we use a modified version of the “`stripmapApp.py`” (94) from ISCE-2 to coregister SLC images using precise orbits and Copernicus DEM. The configuration of speckle tracking is the same as Sentinel-1 data, except that the cross-correlation window size is 64 by 64 (about 107 by 91 m on the ground), and the inter-window step size is 32 by 32, in both range and azimuth directions. We masked out noisy pixels with the following criteria: 1) in

the water; 2) offset standard deviation (STD) ≥ 0.4 and 0.25 m in the range and azimuth directions, respectively; 3) offset signal-to-noise ratio (SNR) ≥ 5 and 8 in the range and azimuth directions, respectively. Due to the larger sensitivity of the L-band LuTan-1 compared to the C-band Sentinel-1 (91), we observed even stronger ionospheric effects (fig. S38), therefore, we remove a linear ramp along the azimuth direction for LuTan-1 ascending track 52 range offset and a linear ramp along the range direction and cubic ramp along the azimuth direction for LuTan-1 ascending track 52 azimuth offset.

For ALOS-2 SAR images, we apply InSAR for deformation in the slant range direction using the “alos2App.py” (95) from ISCE-2. We use the Copernicus DEM, multilook the interferogram by 5 and 28 looks in range and azimuth directions, respectively, then apply the Goldstein filter with a strength of 0.8, and unwrap the interferogram using the minimum cost flow method (96) with near-fault pixels masked out using the surface rupture traces from Sentinel-1 speckle tracking. We correct for ionospheric delay using the range split-spectrum technique (97), for tropospheric delay using the ERA5 global atmospheric model (98) via PyAPS (99), and for solid Earth tides following the 2010 IERS convention (100) via PySolid (91) (fig. S39).

For Sentinel-2 optical images, we utilize the preliminary cross-correlation displacement product from USGS directly (101), which has a grid resolution of 0.000728597° (~ 80 m) and was generated using the COSI-Corr software (102). Considering the non-physical ramp in both the east-west and north-south directions, we estimate a quadratic ramp from the far-field observation and remove it from all pixels for each of the four displacement observations (fig. S40). We also manually shift 6 pixels to the west for the 20250325-20250330 and 20250327-20250401 pair, respectively, to fix their geolocation inconsistency with the SAR speckle tracking result, since SAR satellite imagery usually has much higher geolocation accuracy (91). Due to the noisy artefacts observed in the east-west displacement (fig. S40), we use the north-south displacement only in the analysis afterward, including both the three-dimensional displacement estimation and joint finite fault inversion.

We combine all the above-mentioned displacement observations to derive the three-dimensional co-seismic deformation, including 4 range offsets and 4 azimuth offsets from Sentinel-1, 1 range offset and 1 azimuth offset from LuTan-1, 2 range offsets from ALOS-2, and 2 north-south offsets from Sentinel-2, following the methods of (103, 104), as implemented in the MintPy software (105). We used a weighted method (17) to balance the different uncertainties among the different datasets and propagated the uncertainties to the east, north, and up components of each pixel. More specifically, we used the pixel-wise speckle tracking STD for Sentinel-1 and LuTan-1, and used a fixed value of 0.05 m and 0.8 m as the STD for ALOS-2 interferograms and Sentinel-2 dense offsets. The estimated east, north, and up components were masked using STD thresholds of 0.4 m, 0.8 m, and 0.3 m, respectively (fig. S32).

Seismic Impact Assessment Using Damage Proxy Map

We use the interferometric coherence to quantitatively analyze changes in surface reflection characteristics before and after the earthquake (106). We collect the Sentinel-1A descending images, including acquisitions before and after the earthquake. We use the “topsApp.py” (89) from the ISCE-2 software (88) to coregister the SLC images, form the interferogram, and estimate the coherence via the Cramer-Rao bound relationship as formula (3) :

$$\gamma = \frac{1}{\sqrt{1 + 2N\sigma_{\phi}^2}} \quad (3)$$

where N denotes the estimation window size. This equation translates the phase standard deviation σ_{ϕ} to coherence. Using this procedure, we generate the preseismic and coseismic coherence γ_{pre} and γ_{co} using a pre-/pre-seismic image pair and a pre-/post-seismic image pair, respectively, then normalize their difference as below to produce the DPM_{value} (fig. S25b) in formula (4):

$$DPM_{value} = \frac{\gamma_{pre} - \gamma_{co}}{\gamma_{pre} + \gamma_{co}} \quad (4)$$

To extract anomalous features from the DPM, we apply a minimum threshold of $\mu + 3\sigma$ (μ and σ denote the mean and standard deviation) to identify high-value areas (fig. S25a) (19). The core mechanism is that surface ruptures, fault slips, and secondary hazards triggered by seismic waves alter the scattering properties of surface materials, resulting in high coherence loss areas in the DPM. In Mandalay’s city center near the fault, clusters of high DPM values align with observed structural damage, liquefaction, and surface rupture, as confirmed by Jilin-1 optical imagery (fig. S26a–b). Coherence time series further show a sharp drop during the earthquake and gradual recovery afterward, demonstrating the interpretability of DPM as a seismic damage proxy (fig. S26c).

The Causal Bayesian Network is employed to estimate the probabilities of seismic multi-hazards, including landslides, liquefaction, and building damage, by modeling the causal relationships among these hazards. Detailed workflow, equations, and algorithms are described in (20). In the network, each node represents a random variable (e.g., landslide, liquefaction), and edges represent causal dependencies. For example, ground shaking affects both liquefaction and landslides, which in turn contribute to building damage. The model integrates DPM with prior geospatial hazard models and building footprint data (obtained from OpenStreetMap) to improve prediction accuracy. The input data DPM and USGS hazard models (71; fig. S27a) are fed into the Bayesian network, which then produces refined probability estimates for multiple hazards (fig. S27b), including building damage in densely populated areas (fig. S28), as well as

landslides and liquefaction. Using variational Bayesian inference, the model estimates the posterior probabilities of unobserved variables, generating high-resolution hazard probability maps that support disaster response and recovery.

Energy Ratio Analysis

In our discussion, we analyzed the evolution of the energy ratio using the following logic and equations. The elastic energy release rate on long faults, G_0 , has been theoretically derived and numerically validated as $G_0 = C\mu D^2/W$, where C is a geometric factor of order unity, μ is the shear modulus, D is the final slip, and W is the rupture width (56, 107, 108). Meanwhile, the fracture energy G_c has been proposed based on theoretical considerations (109, 110) as a function of final slip D through the scaling relation $G_c \sim B*D^n$, where the coefficients B and n can be constrained based on the data obtained by dynamic earthquake modeling (111, 112, 113), laboratory experiments (114), and seismological approaches such as kinematic inversions (115). Scale-independent G_c corresponds to $n=0$ (e.g., linear slip-weakening), while scale-dependent G_c corresponds to $n>0$ (e.g., rate-and-state friction). The coefficient n reflects distinct mechanisms of fault friction: $n=1$ for off-fault inelastic dissipation (116, 117), $n=2/3$ for thermal pressurization combined with rate-and-state friction (110). Specifically, for regularized rate-and-state friction that is supposed to control slow nucleation processes (118), fault healing resistance increases logarithmically with the interseismic period, resulting in a scaling relationship with $n < 1$. As a result, the scaling of fracture energy is expected to satisfy the condition $n < 2$. Therefore, although both G_c and G_0 increase over time, G_0 grows faster with increasing slip for $D > 1$. Assuming a linear relationship between the potential slip deficit and interseismic duration, and that the earthquake has released all the potential slip deficit (i.e., D), the energy ratio G_c/G_0 decreases as the interseismic period increases, making the fault increasingly favorable for supershear rupture.

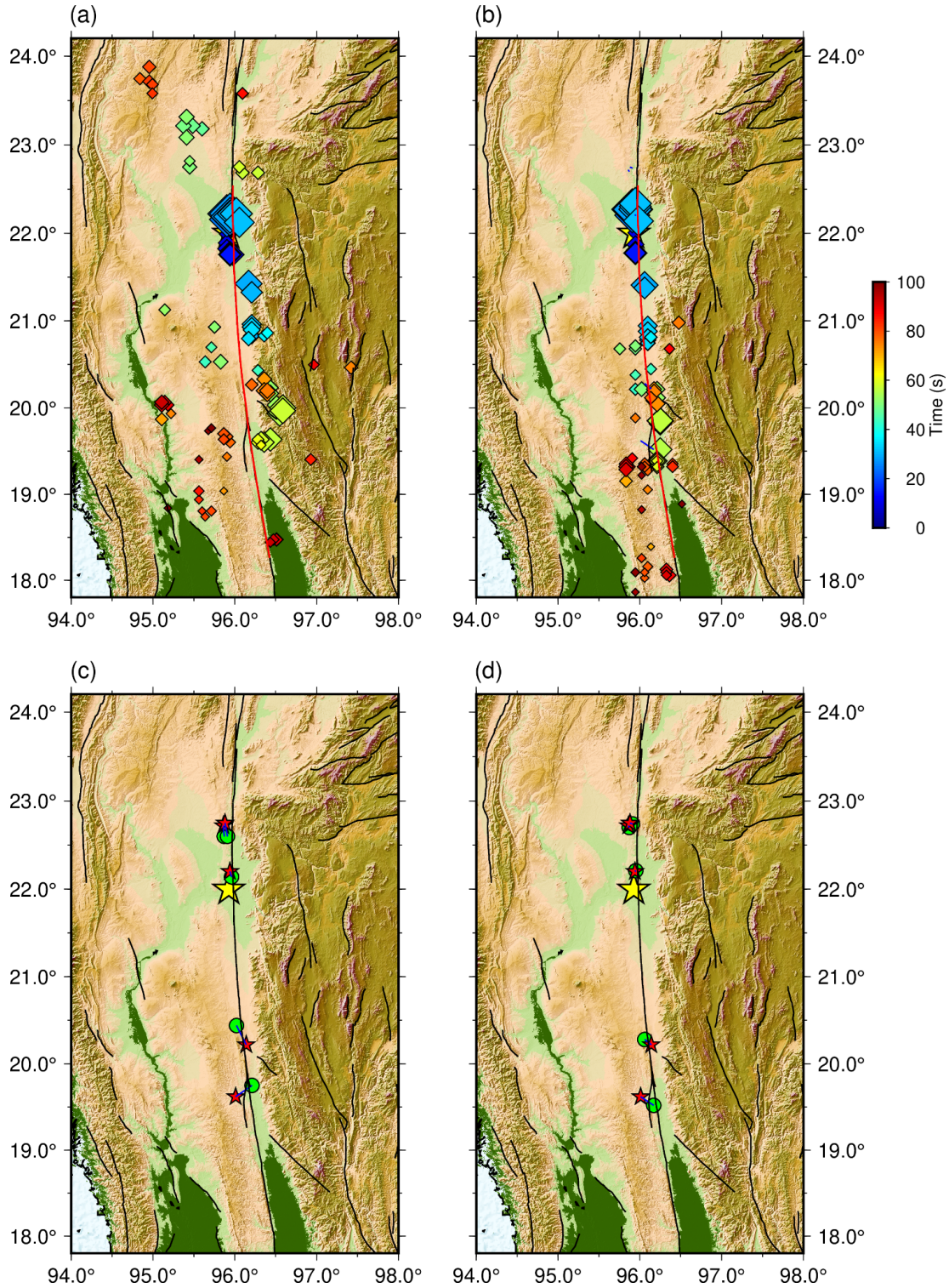


Fig. S1. Comparison of aftershock locations and mainshock BPs by the Alaska array before and after calibration. (a) The AK array's results for the mainshock before slowness calibration. The red line denotes the surface rupture trace identified by USGS according to the ground deformation pattern. The yellow star denotes the epicenter of the mainshock. Diamonds denote the HF radiators for the Mw 7.8 event, color-coded by rupture time relative to the origin time of

the event and with a size proportional to the normalized BP power. (b) The AK array's results for the mainshock after slowness calibration and removal of northern radiators after 40 s. (c) The AK array's results for aftershocks along the rupture path before slowness calibration. Green circles denote the BP-inferred locations of M4.5+ aftershocks spanning the rupture region. The red stars denote the NEIC catalog epicenter of aftershocks. (d) The AK array's results for aftershocks along the rupture path after slowness calibration.

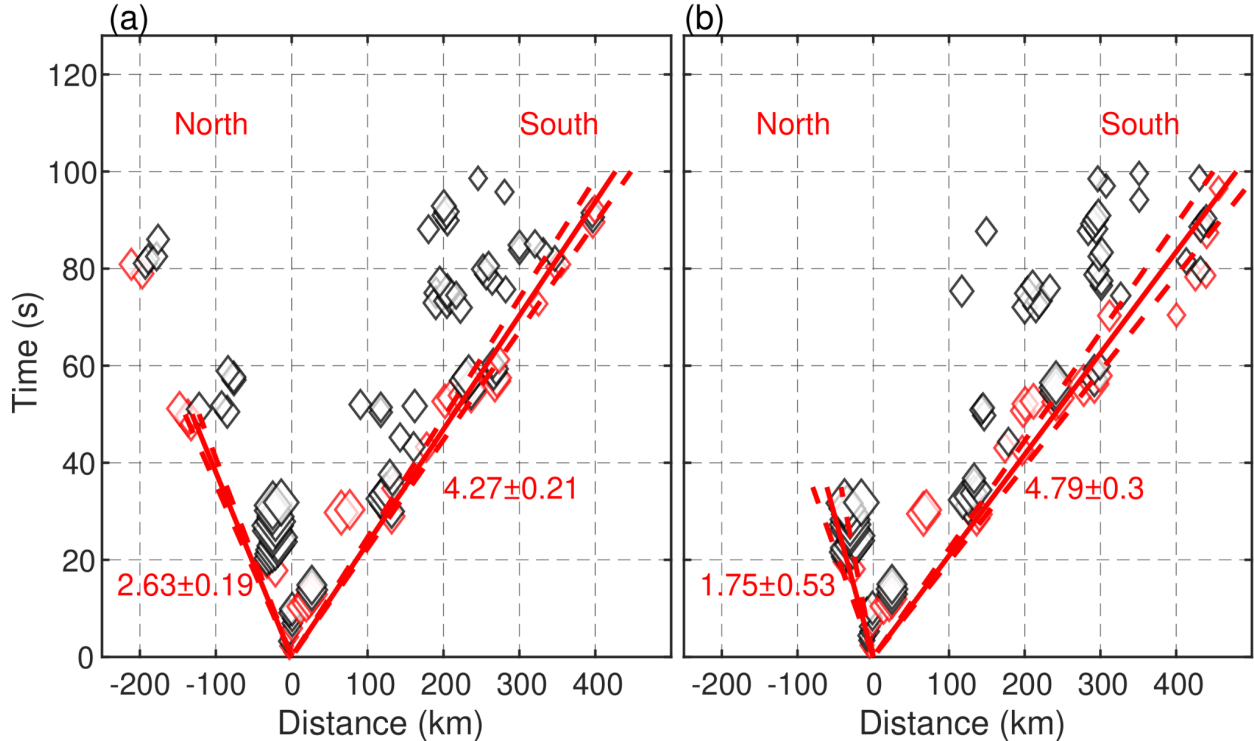


Fig. S2. The rupture speed measurements before calibration (a) and after calibration (b). Symbols mark the timing and location of high-frequency radiators imaged by the AK array. Locations are shown as along-fault distances relative to the hypocenter, with positive values to the south and negative to the north, adjusted for fault strike variations (see fault model in Fig. 2). The red solid line indicates the best-fit steady rupture front, with the average rupture speed and its standard deviation labeled and outlined by red dashed lines.

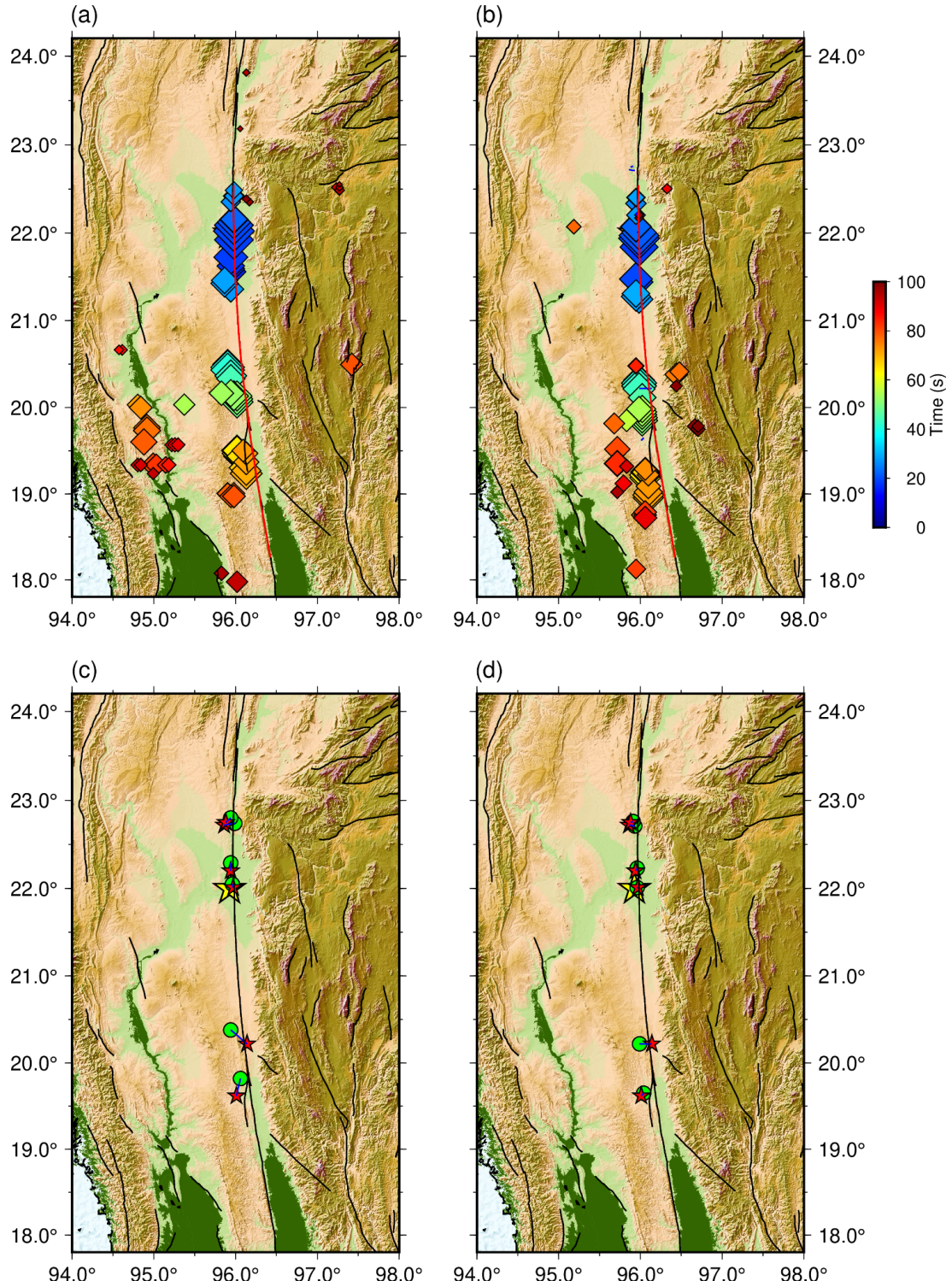


Fig. S3. Comparison of aftershock locations and mainshock BPs by the Australia array before and after calibration. (a) The AU array's results for the mainshock before slowness calibration. The red line denotes the surface rupture trace identified by USGS according to the ground deformation pattern. The yellow star denotes the epicenter of the mainshock. Diamonds denote the HF radiators for the Mw 7.8 event, color-coded by rupture time relative to the origin time of

the event and with a size proportional to the normalized BP power. (b) The AU array's results for the mainshock after slowness calibration and removal of northern radiators after 40 s. (c) The AU array's results for aftershocks along the rupture path before slowness calibration. Green circles denote the BP-inferred locations of M4.5+ aftershocks spanning the rupture region. The red stars denote the NEIC catalog epicenter of aftershocks. (d) The AU array's results for aftershocks along the rupture path after slowness calibration.

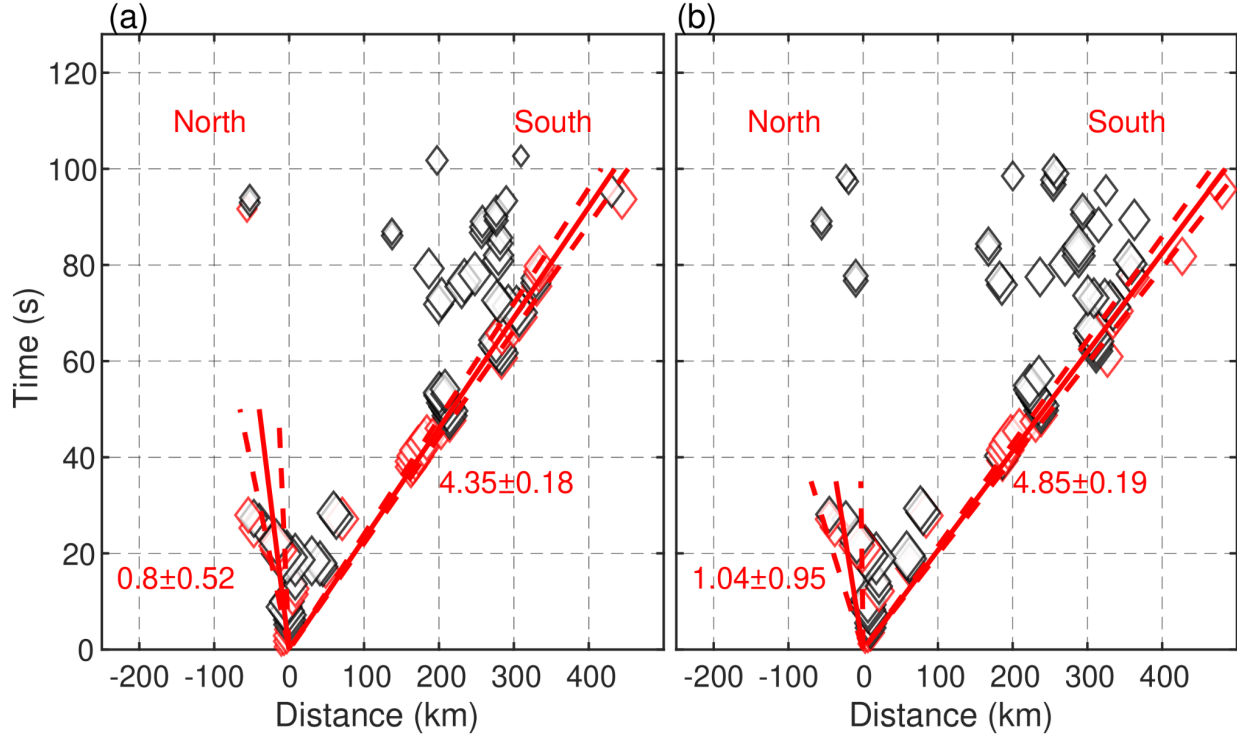


Fig. S4. The rupture speed measurements before calibration (a) and after calibration (b). Symbols mark the timing and location of high-frequency radiators imaged by the AU array. Locations are shown as along-fault distances relative to the hypocenter, with positive values to the south and negative to the north, adjusted for fault strike variations (see fault model in Fig. 2). The red solid line indicates the best-fit steady rupture front, with the average rupture speed and its standard deviation labeled and outlined by red dashed lines.

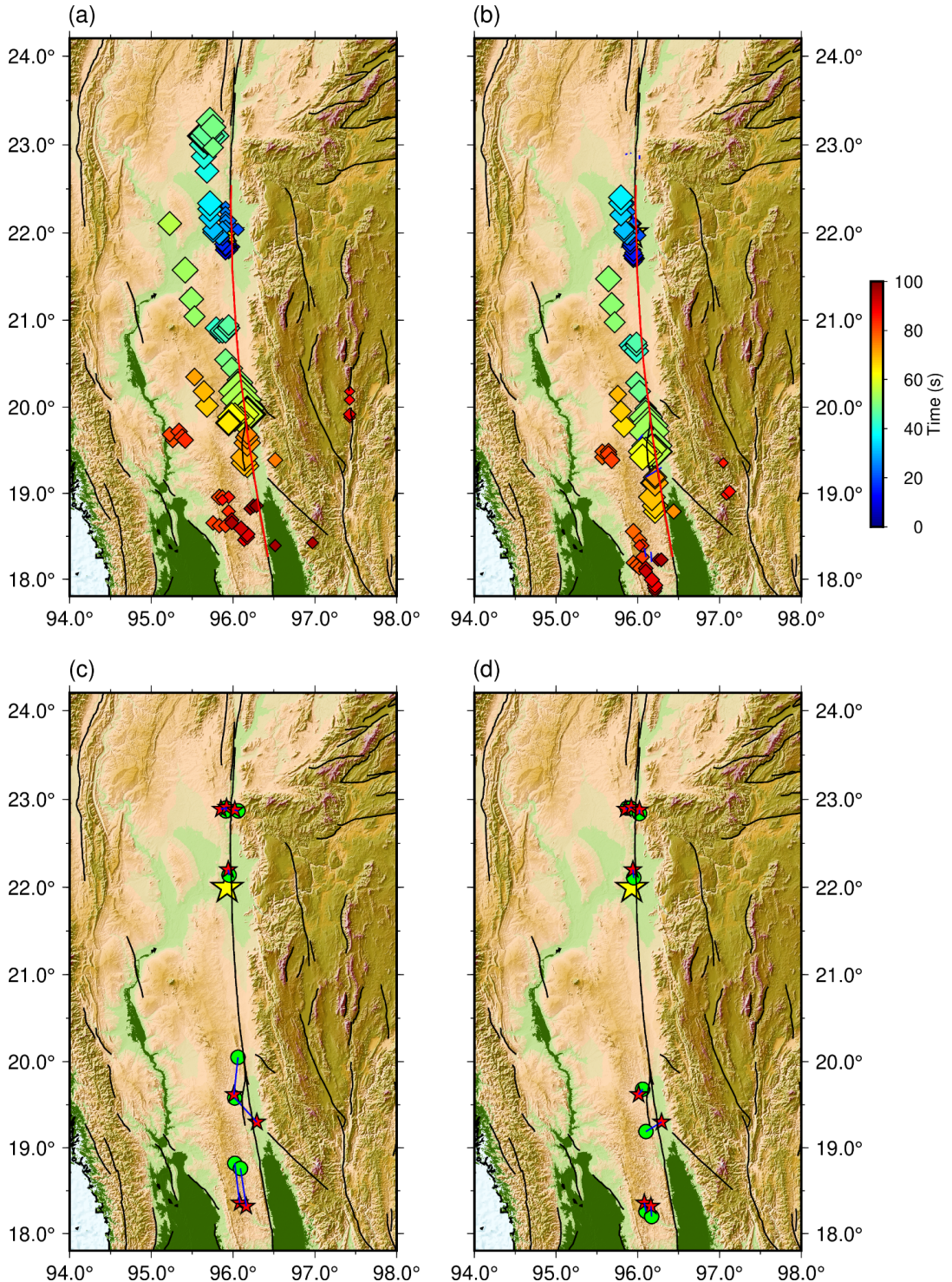


Fig. S5. Comparison of aftershock locations and mainshock BPs by the Europe array before and after calibration. (a) The EU array's results for the mainshock before slowness calibration. The red line denotes the surface rupture trace identified by USGS according to the ground deformation pattern. The yellow star denotes the epicenter of the mainshock. Diamonds denote the HF radiators for the Mw 7.8 event, color-coded by rupture time relative to the origin time of

the event and with a size proportional to the normalized BP power. (b) The EU array's results for the mainshock after slowness calibration and removal of northern radiators after 40 s. (c) The EU array's results for aftershocks along the rupture path before slowness calibration. Green circles denote the BP-inferred locations of M4.5+ aftershocks spanning the rupture region. The red stars denote the NEIC catalog epicenter of aftershocks. (d) The EU array's results for aftershocks along the rupture path after slowness calibration.

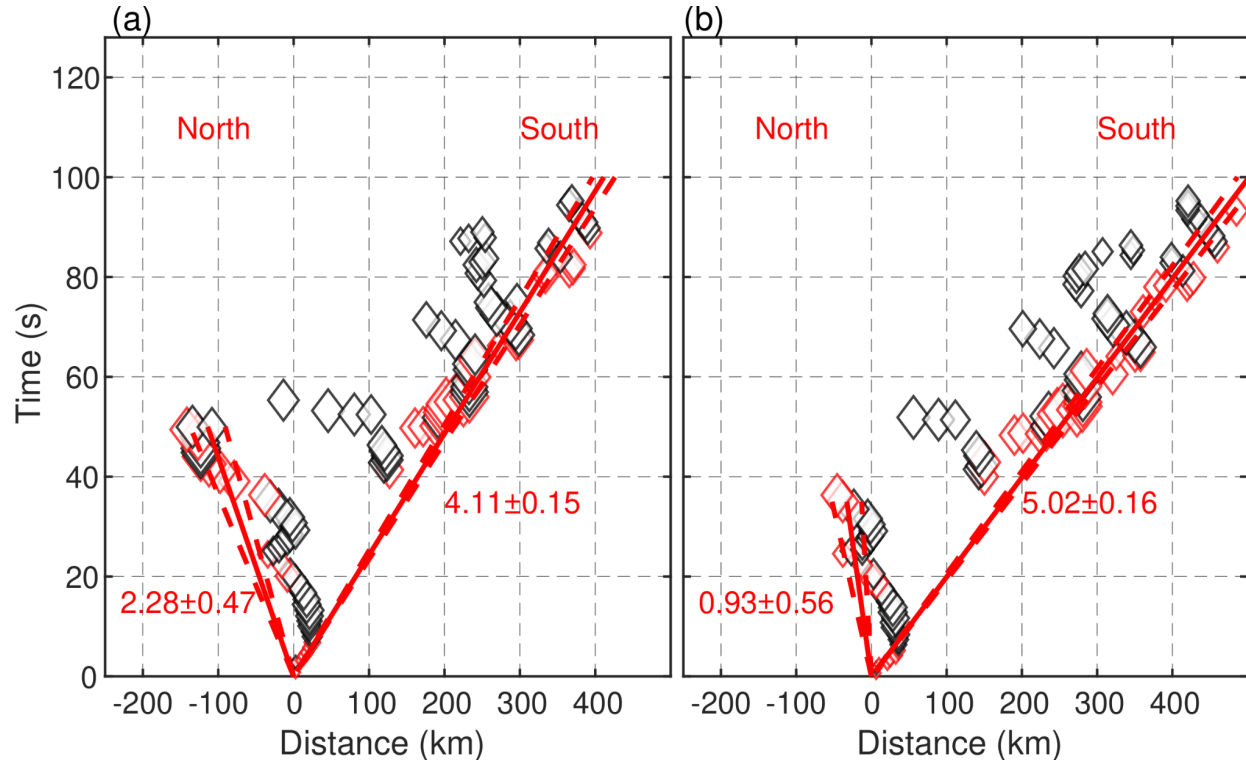


Fig. S6. The rupture speed measurements before calibration (a) and after calibration (b). Symbols mark the timing and location of high-frequency radiators imaged by the EU array. Locations are shown as along-fault distances relative to the hypocenter, with positive values to the south and negative to the north, adjusted for fault strike variations (see fault model in Fig. 2). The red solid line indicates the best-fit steady rupture front, with the average rupture speed and its standard deviation labeled and outlined by red dashed lines.

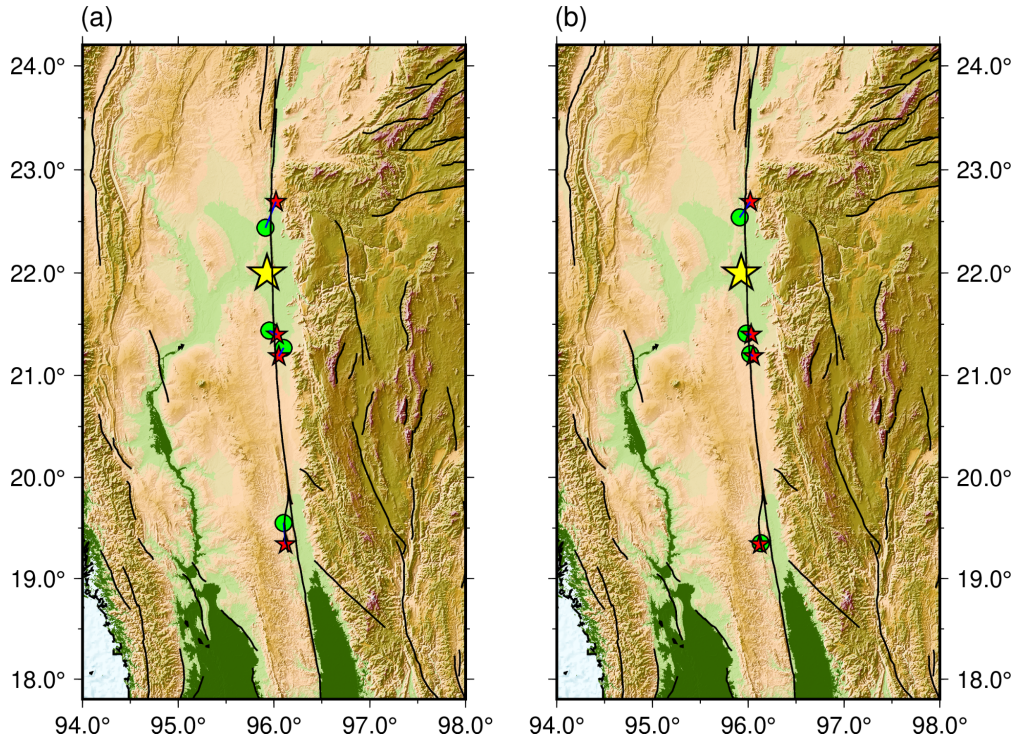


Fig. S7. Validation of slowness calibration for the AK array. (a) BP results from the AK array for M4.5+ aftershocks (table S5a) along the rupture path before slowness calibration. Green circles indicate BP-inferred locations; red stars mark NEIC catalog epicenters. (b) Same as (a), but after applying slowness calibration. Note that these aftershocks were not used to derive the calibration terms, providing an independent validation.

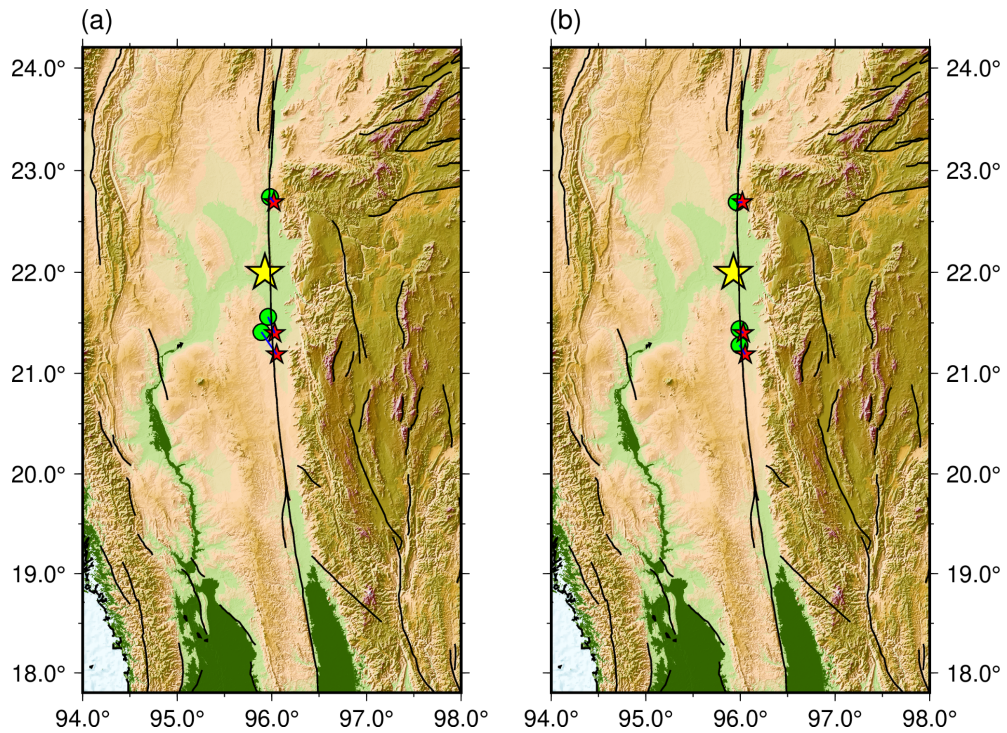


Fig. S8. Validation of slowness calibration for the AU array. (a) BP results from the AU array for M4.5+ aftershocks (table S5b) along the rupture path before slowness calibration. Green circles indicate BP-inferred locations; red stars mark NEIC catalog epicenters. (b) Same as (a), but after applying slowness calibration. Note that these aftershocks were not used to derive the calibration terms, providing an independent validation.

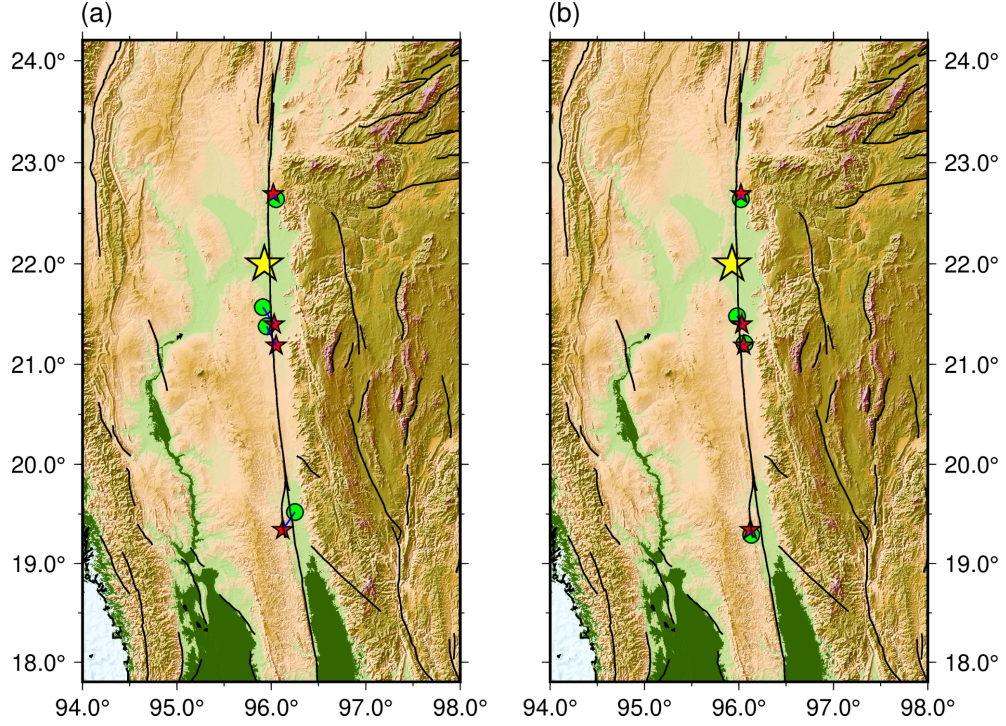


Fig. S9. Validation of slowness calibration for the EU array. (a) BP results from the EU array for M4.5+ aftershocks (table S5c) along the rupture path before slowness calibration. Green circles indicate BP-inferred locations; red stars mark NEIC catalog epicenters. (b) Same as (a), but after applying slowness calibration. Note that these aftershocks were not used to derive the calibration terms, providing an independent validation.

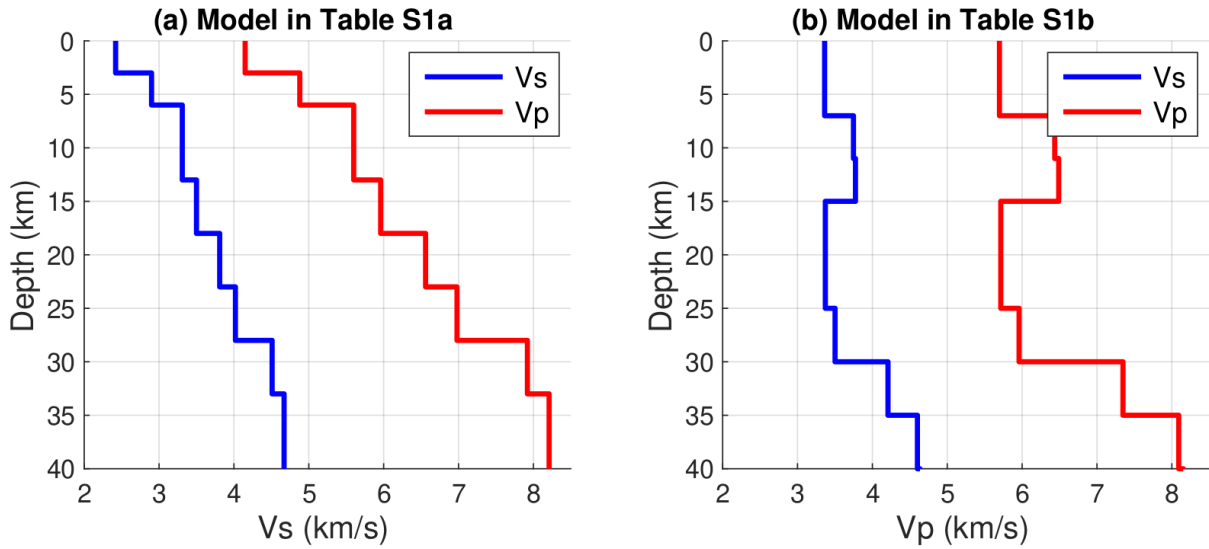


Fig. S10. The seismic velocity model used to compute Green's functions. (a) Vs model used to compute Green's functions for teleseismic broadband P and SH waves, as well as for local

strong-motion stations NPW, NGU, and YGN (fig. S22). This Vs model is also adopted in the calculation of Green's functions for static ground deformation. (b) Vs model used to compute Green's functions for local strong-motion stations CHTO and KTN (fig. S22). Specific values of Vp, Vs, and layer thickness are presented in table S1. Both models are adapted from (5).

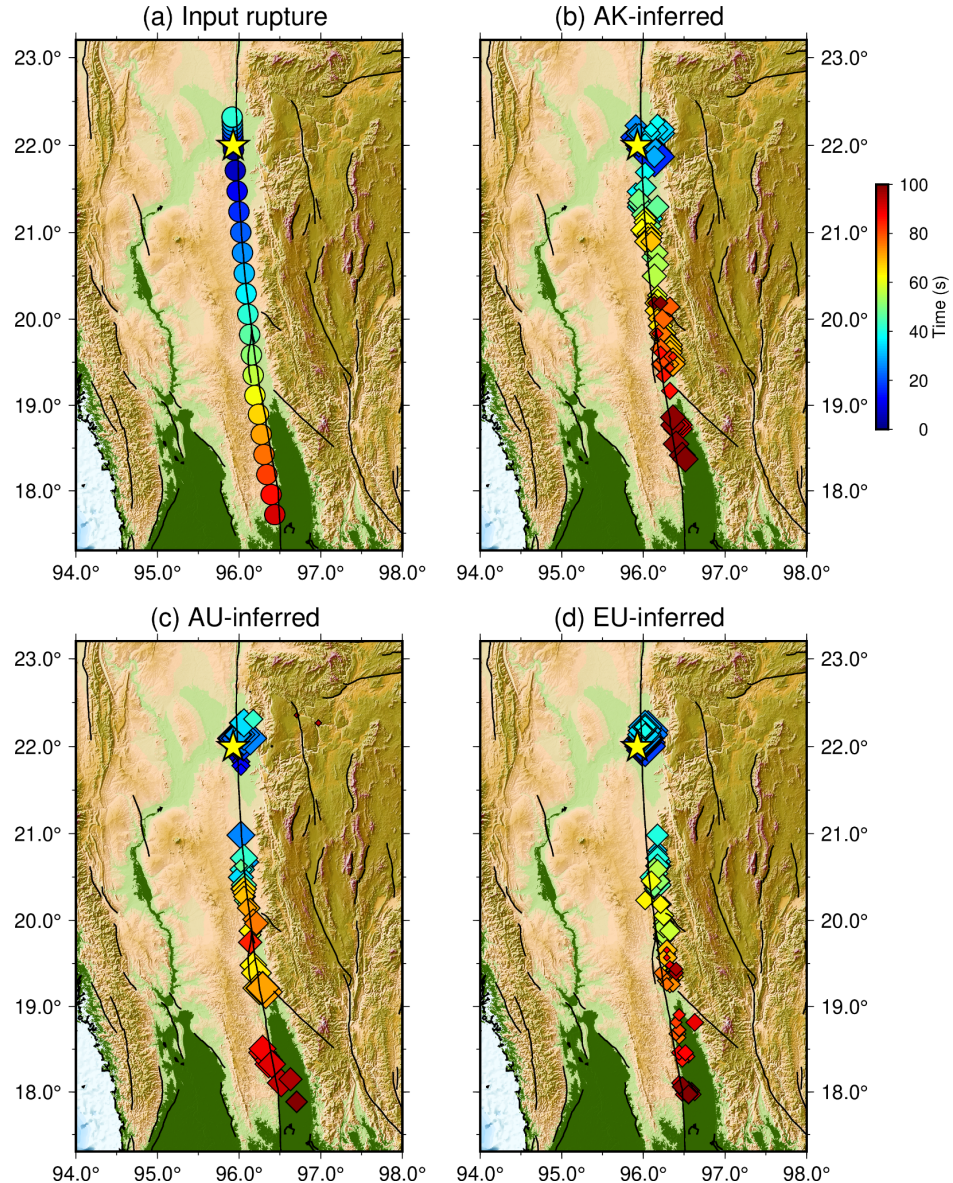


Fig. S11. Synthetic BP. (a) The setup of the synthetic test. The yellow star denotes the epicenter. The color circles denote the input rupture front. The north branch has a rupture speed of 1 km/s, and the south rupture speed is 5 km/s. (b) BP-inferred rupture process by AK array. (c) BP-inferred rupture process by AU array. (d) BP-inferred rupture process by EU array.

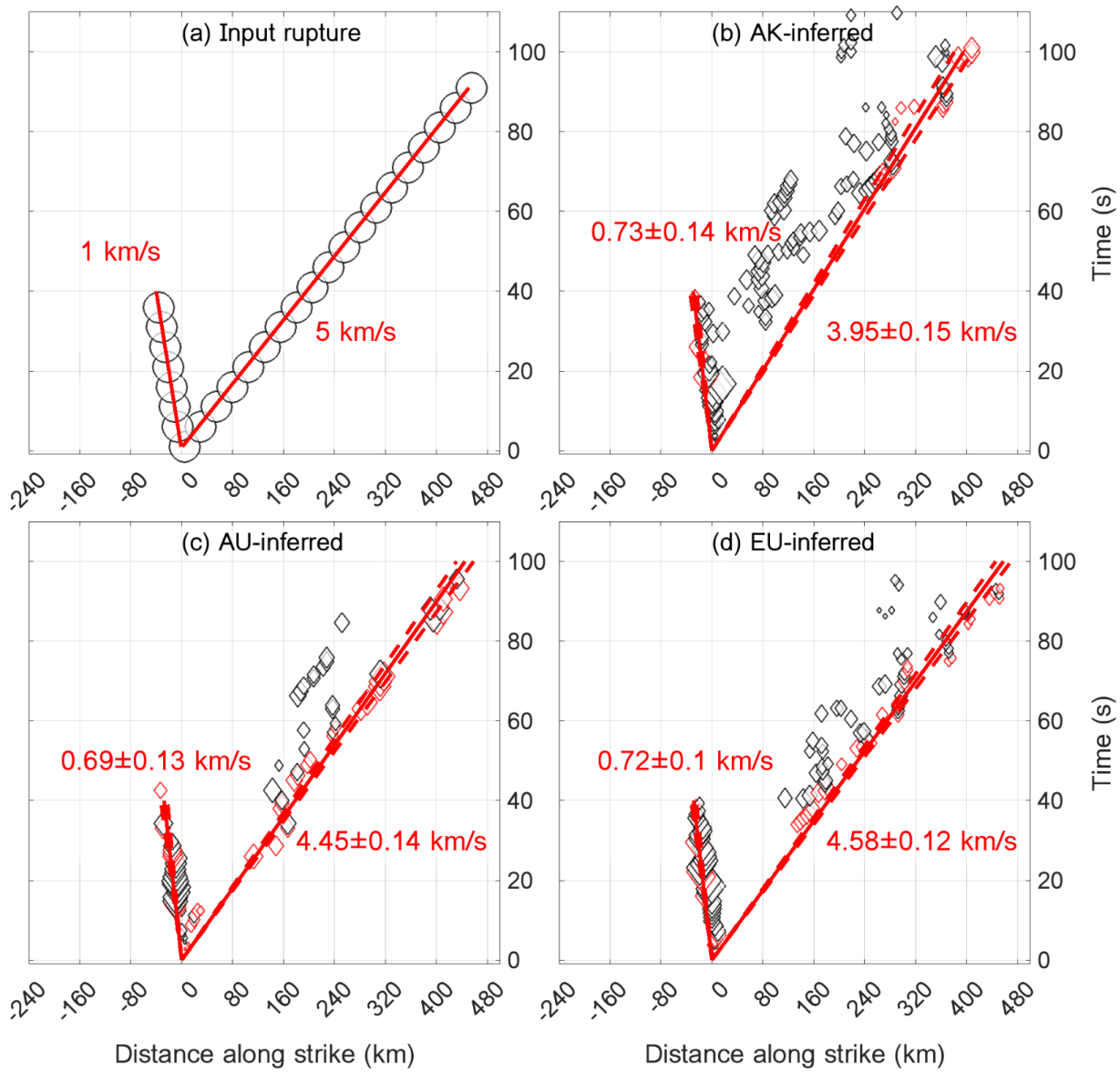


Fig. S12. Along-fault locations and rupture time of synthetic BP radiators. (a) The input rupture front, with positive values to the south and negative to the north. The north branch has a rupture speed of 1 km/s, and the south rupture speed is 5 km/s. (b) BP results resolved by AK array. (c) BP results resolved by AU array. (d) BP results resolved by EU array.

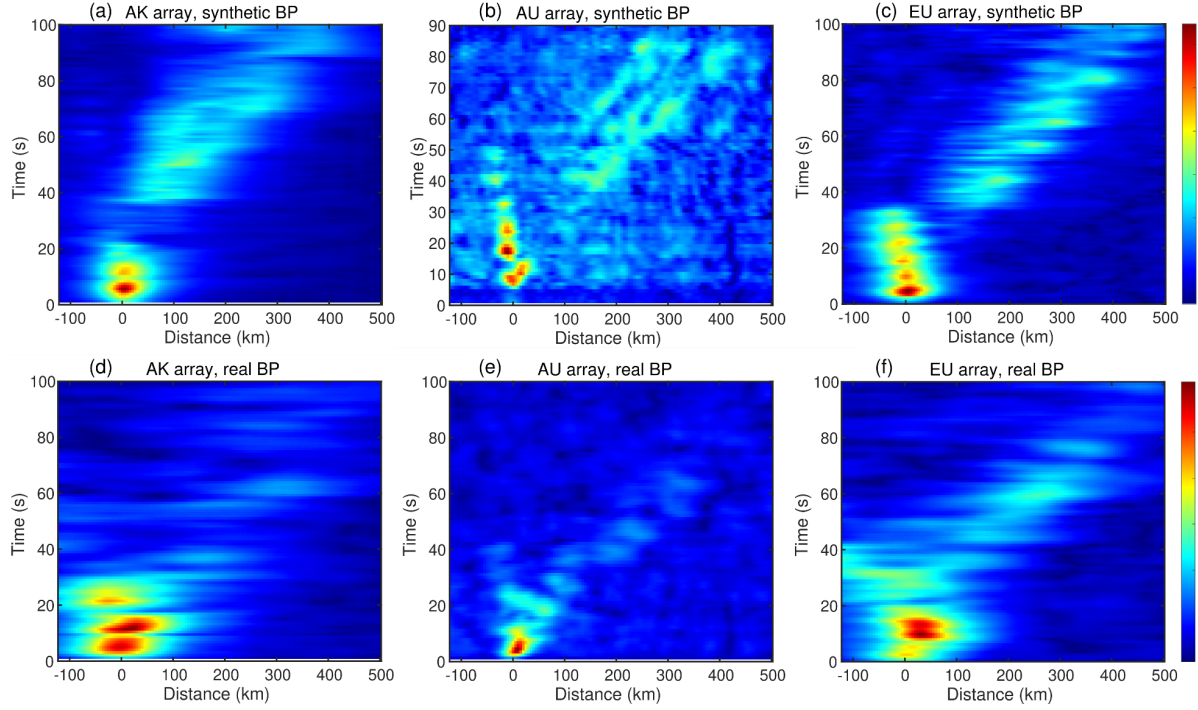
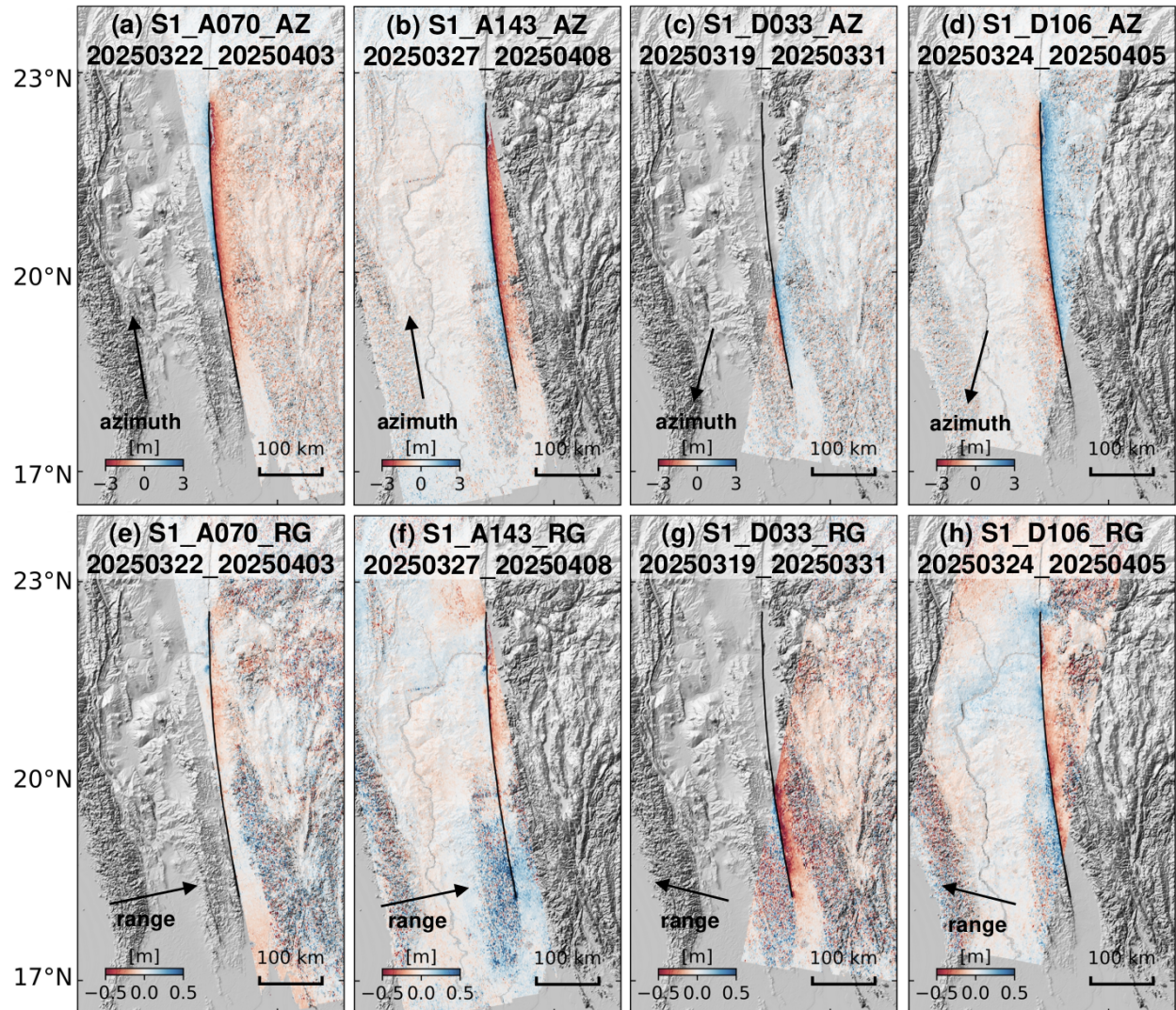


Fig. S13. MUSIC Pseudo-Spectrum (MPS) profiles along the fault over all time steps. (a–c) MPS from synthetic BP results using the AK, AU, and EU arrays, respectively. (d–f) MPS from SEBP results (real observations) for the same arrays. Each panel shows the spatial distribution of MPS along the fault as a function of time, highlighting the consistency between synthetic and real BP results. Note that high-frequency radiators correspond to the MPS peak at each time step, and the MPS values are not directly proportional to beam power or waveform amplitude.



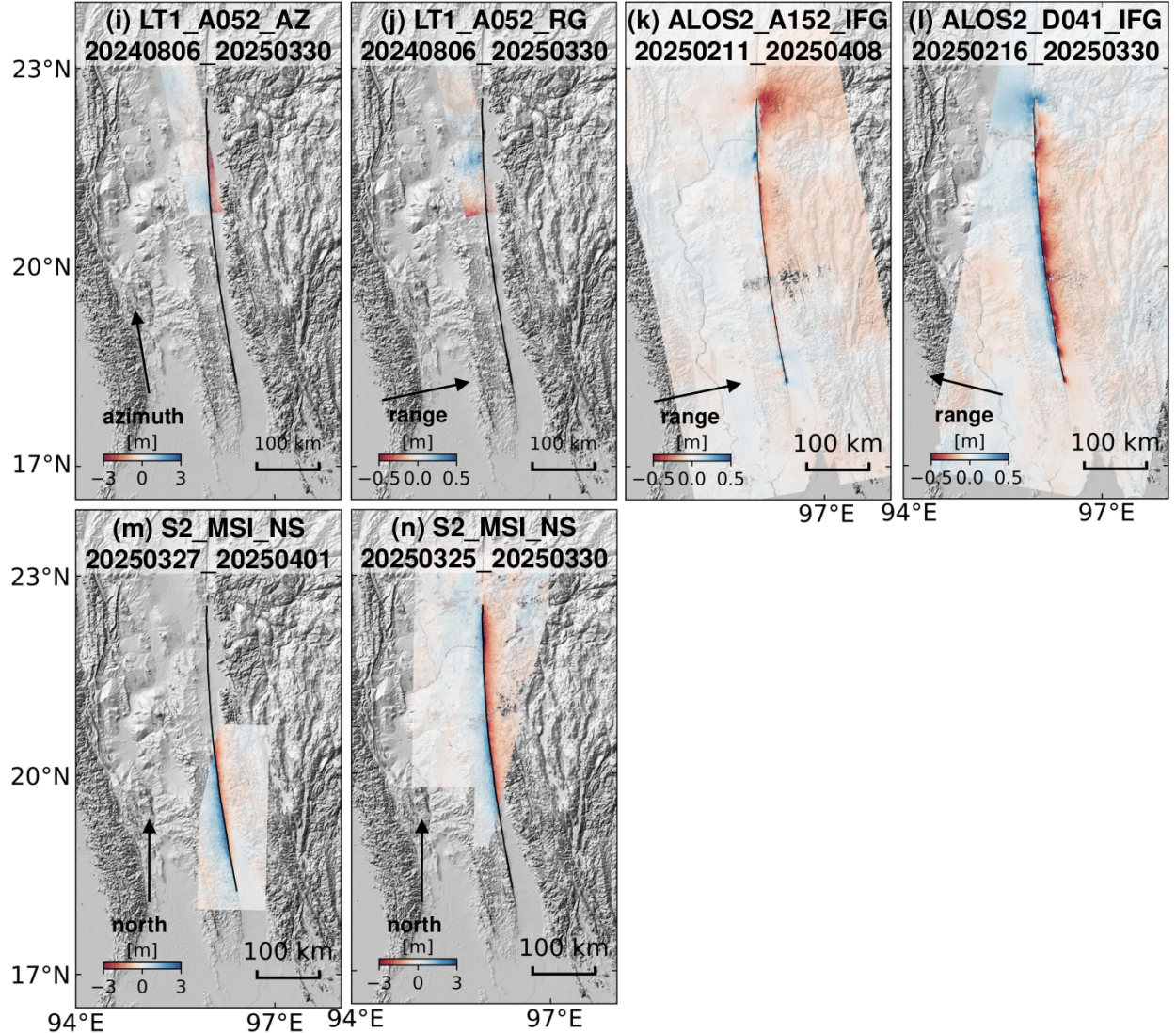
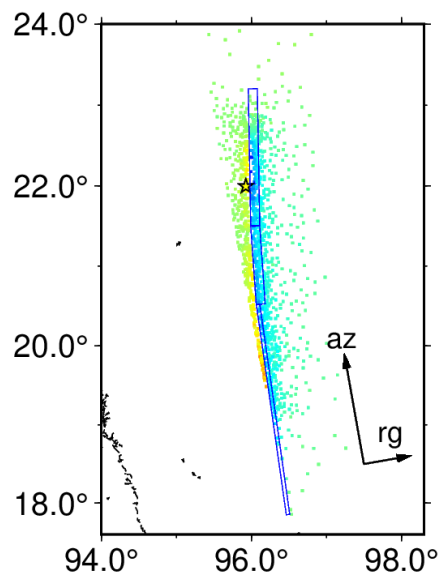
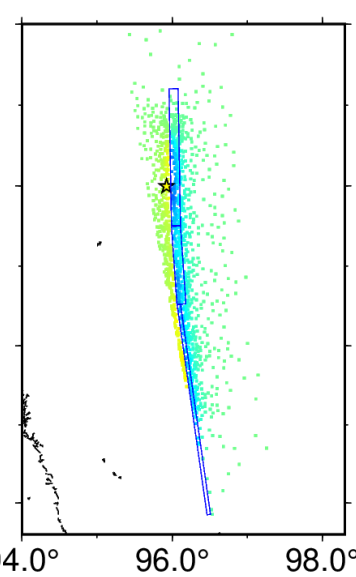


Fig. S14. The original resolution displacement data from all SAR and optical satellites. (a-d) Displacements in the ground azimuth direction from Sentinel-1 ascending track 70 and 143, descending track 33 and 106, respectively. (e-h) Same as (a-d) but for displacements in the slant range direction. (i-j) Displacements in the ground azimuth (i) and slant range (j) directions from LuTan-1 ascending track 52. (k-l) Displacements in the slant range direction from ALOS-2 ScanSAR ascending track 152 and descending track 41, respectively. (m-n) Displacement in the north-south direction from Sentinel-2 imagery, adapted from USGS (101). Figures are named as (subplot index) {sensor name} {orbit direction} {track number} {measure type}, {preseismic date} {postseismic date}. S1: Sentinel-1; S2: Sentinel-2; LT1: LuTan-1; ALOS2: ALOS-2. D: descending; A: ascending. RG: range offset; AZ: azimuth offset. NS: deformation in the north-south direction. MSI: Multispectral Imager; IFG: InSAR interferogram.

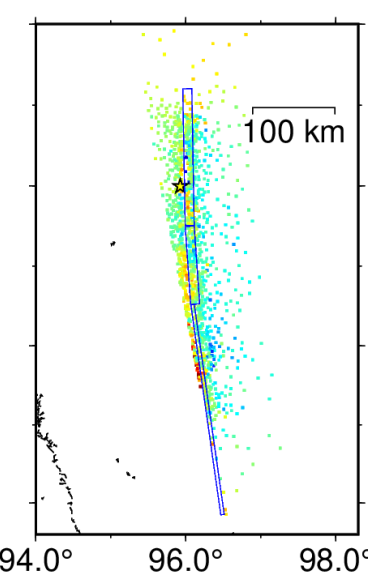
Observation,S1_A070AZ



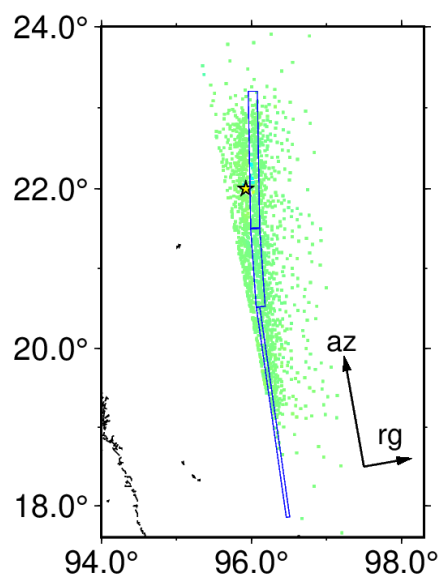
Prediction,S1_A070AZ



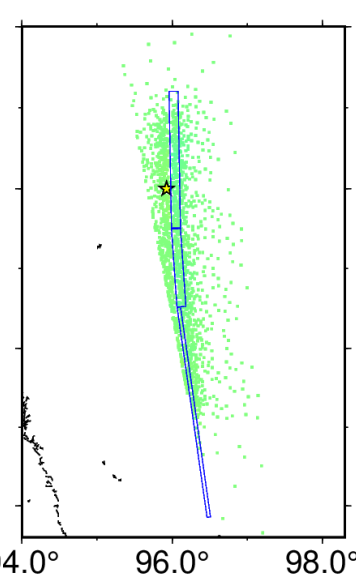
Residuals,S1_A070AZ



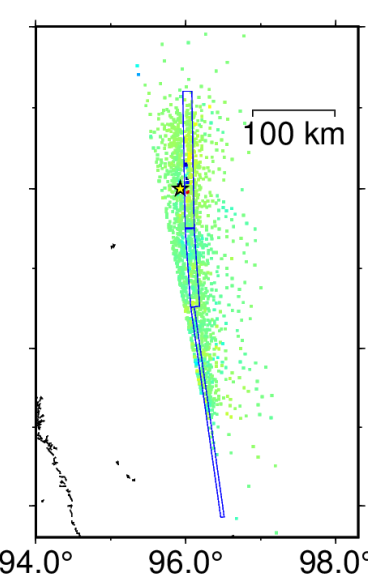
Observation,S1_A070RG



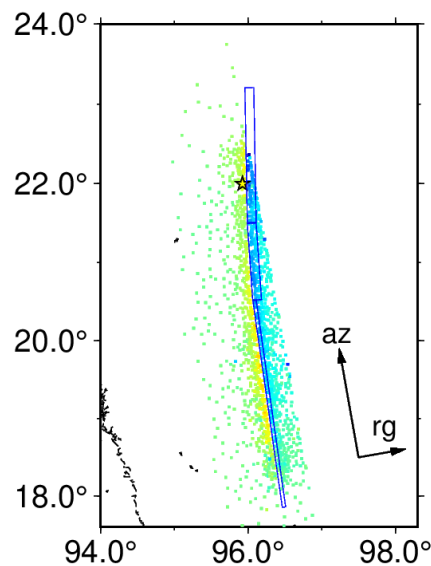
Prediction,S1_A070RG



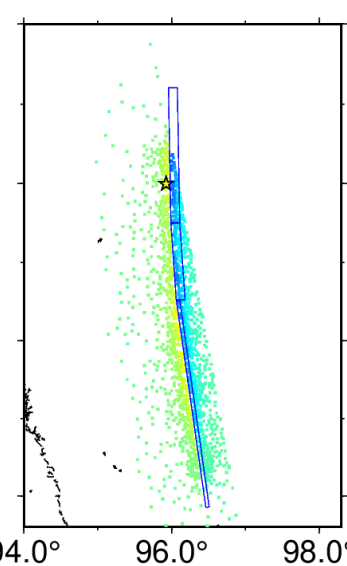
Residuals,S1_A070RG



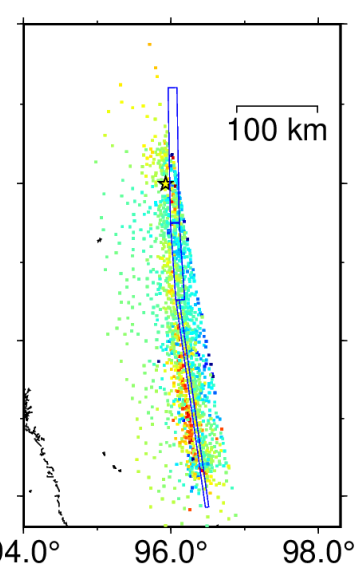
Observation,S1_A143AZ



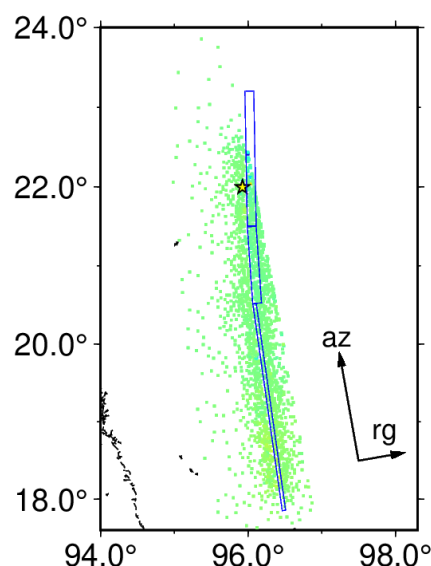
Prediction,S1_A143AZ



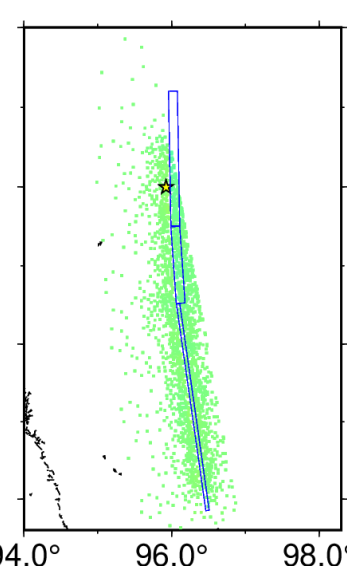
Residuals,S1_A143AZ



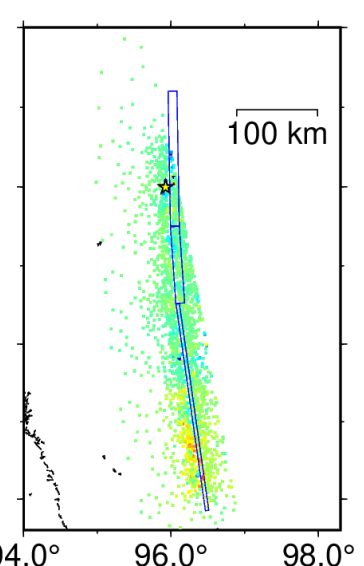
Observation,S1_A143RG



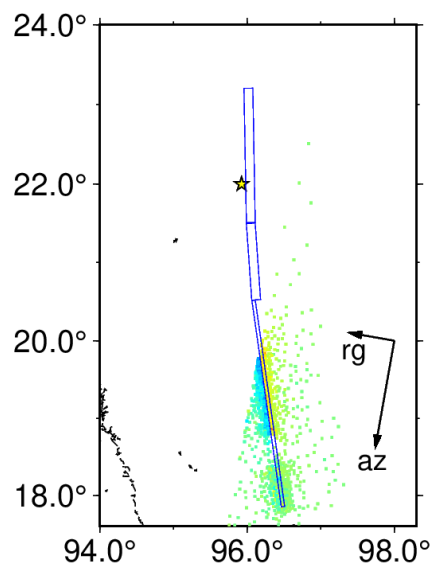
Prediction,S1_A143RG



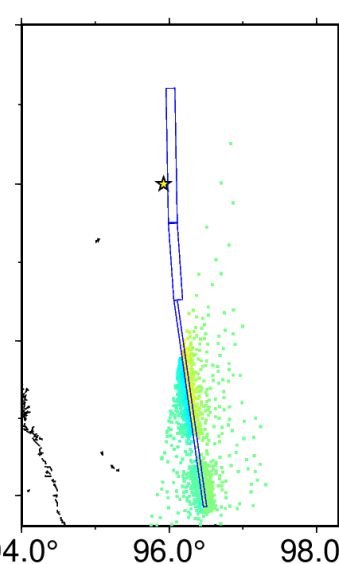
Residuals,S1_A143RG



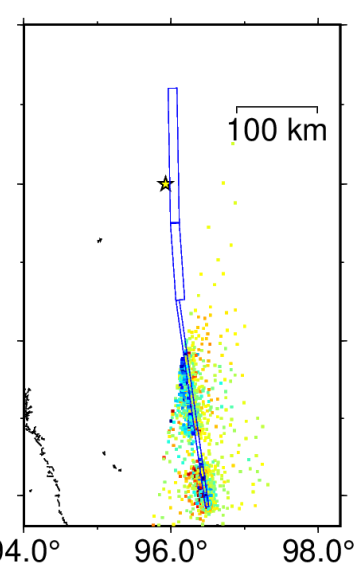
Observation,S1_D033AZ



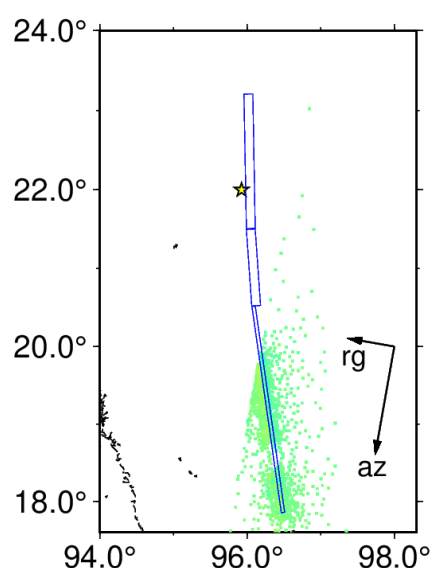
Prediction,S1_D033AZ



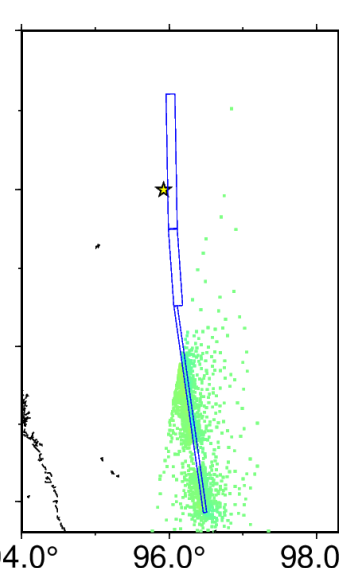
Residuals,S1_D033AZ



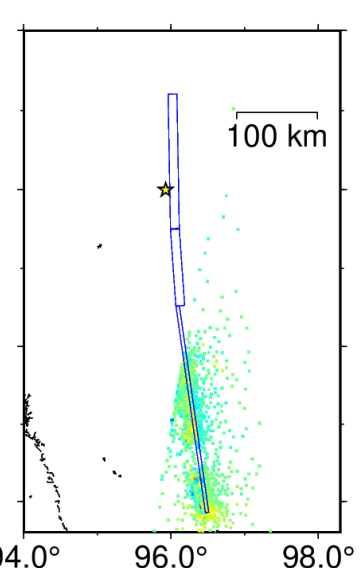
Observation,S1_D033RG



Prediction,S1_D033RG



Residuals,S1_D033RG



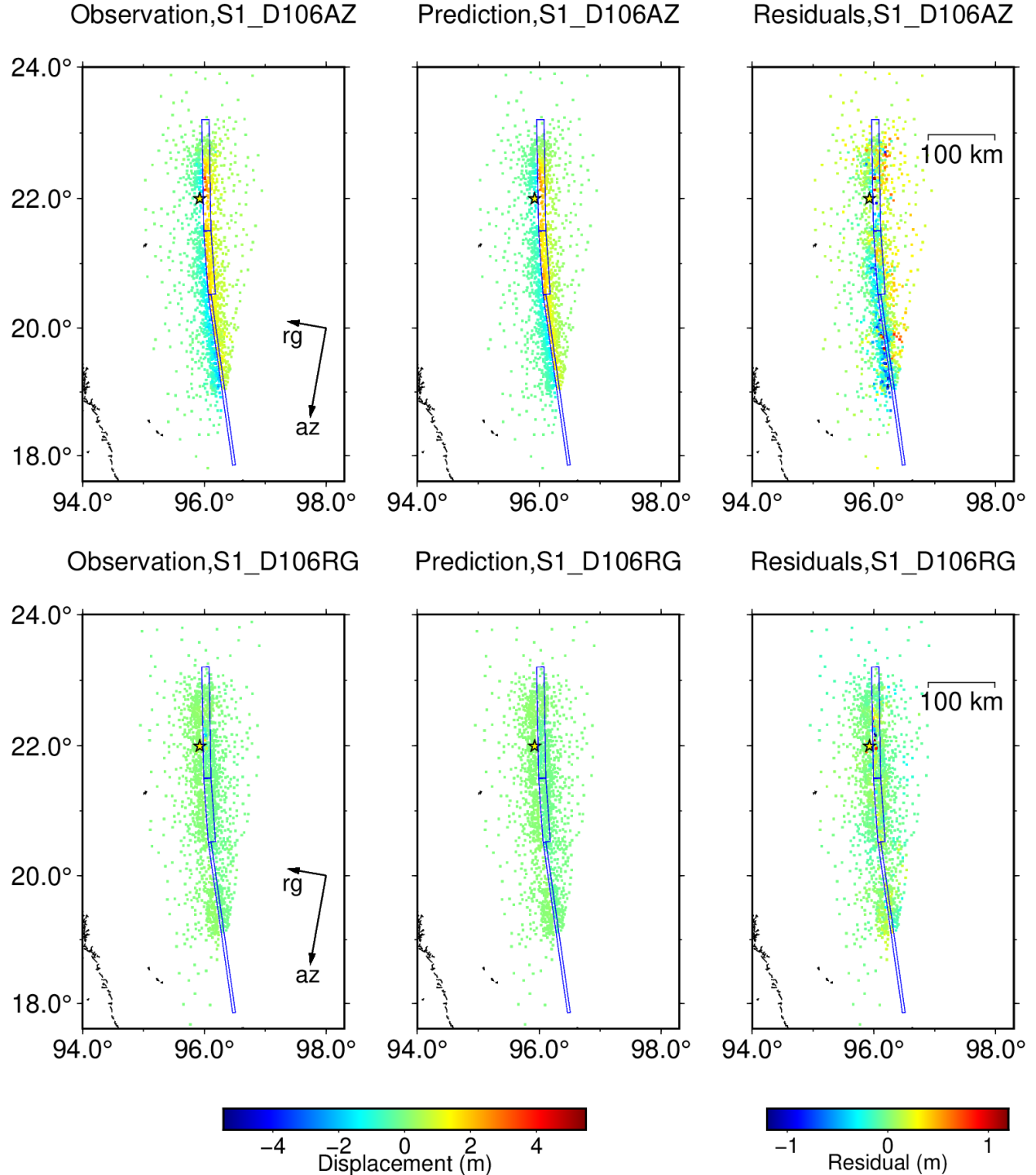
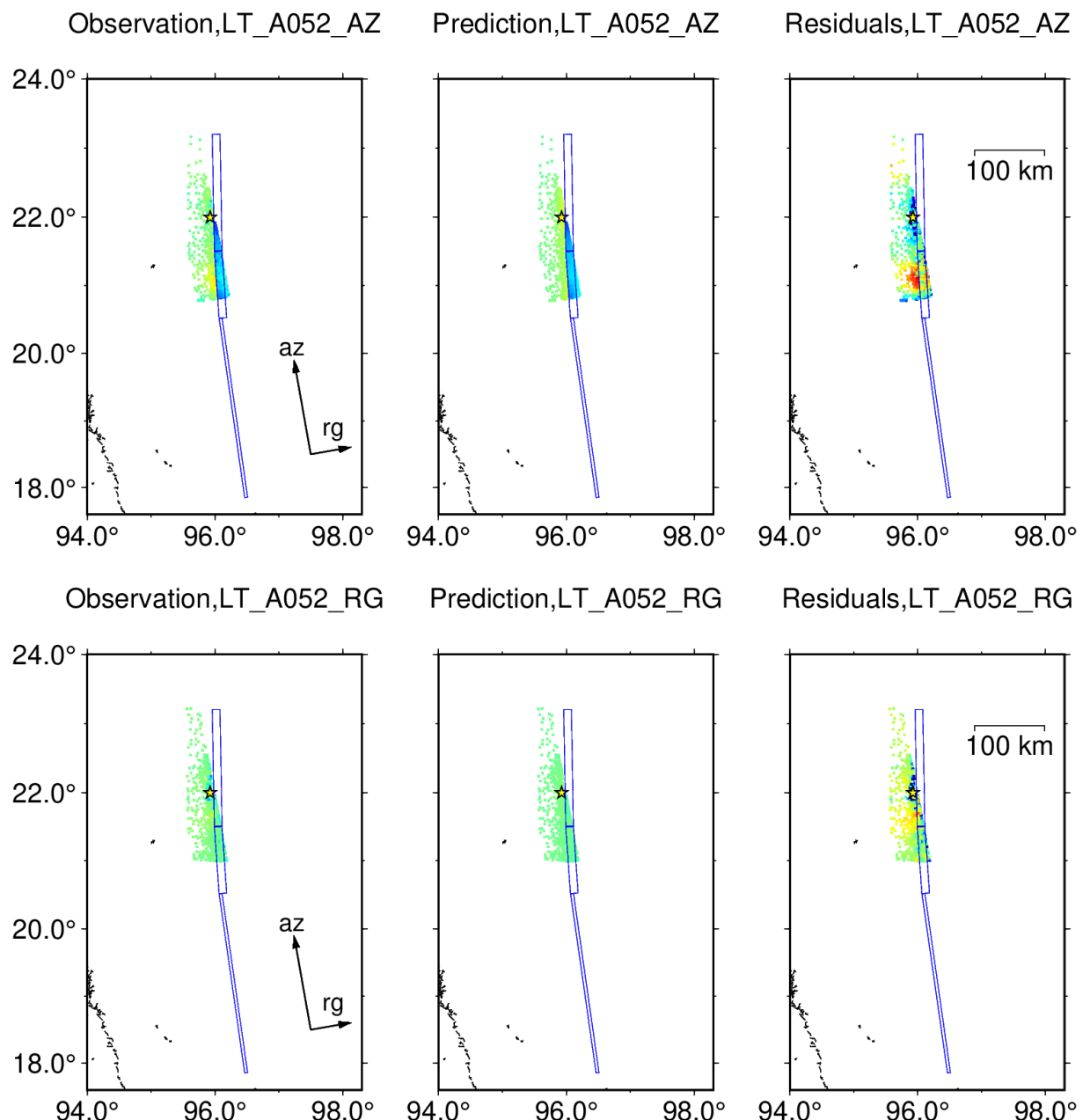
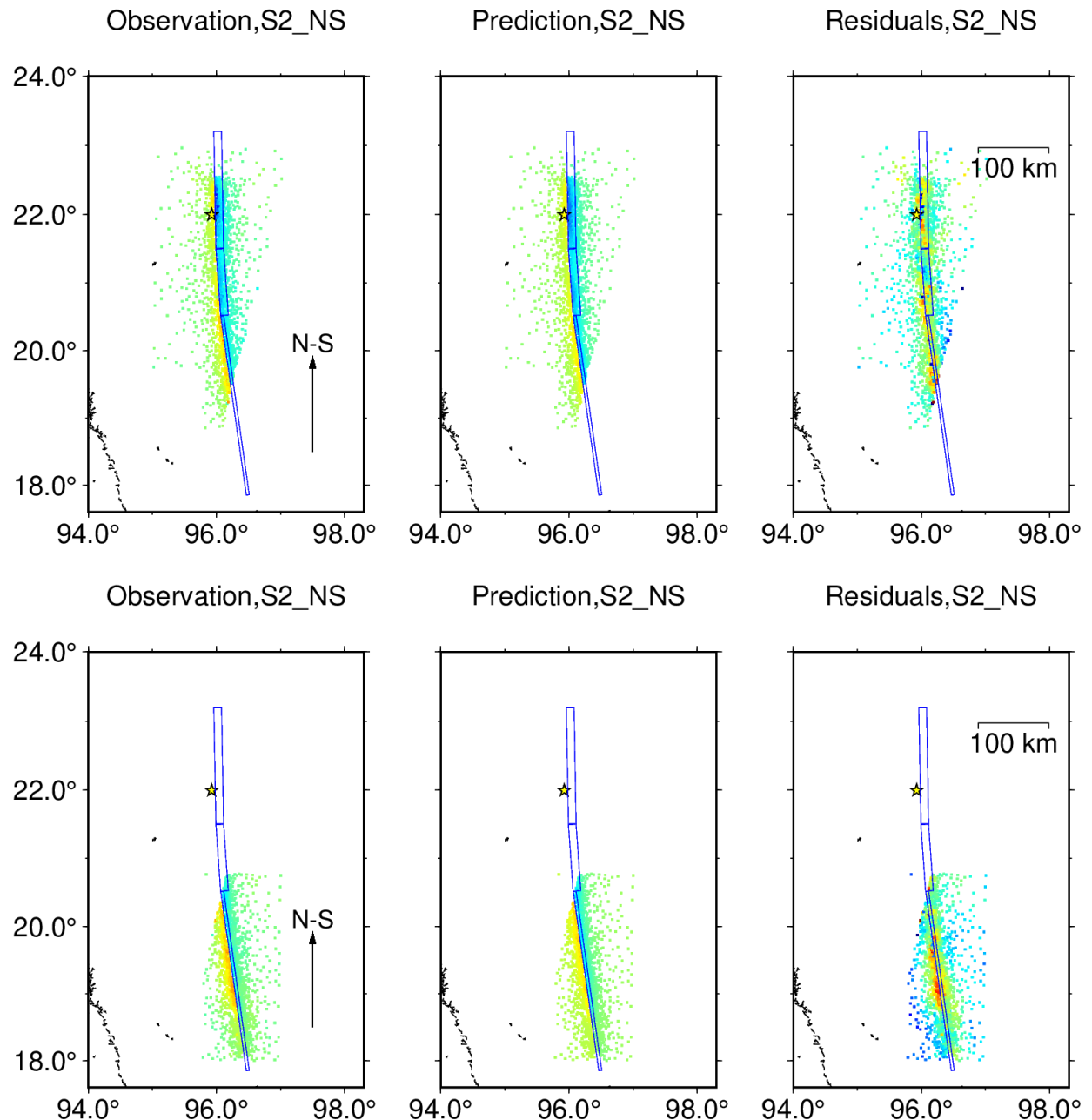


Fig. S15. The sub-sampled Sentinel-1 SAR data fits. The first column is the resampled static displacement (observation). The second column is the prediction by the preferred model. The third column is the residuals obtained by deducting the prediction from the observation. Blue boxes denote the fault planes adopted in joint finite fault inversion. Figures are named as {sensor name} {orbit direction} {track number} {measure type}. S1: Sentinel-1; D: descending; A: ascending; RG: range offset; AZ: azimuth offset.





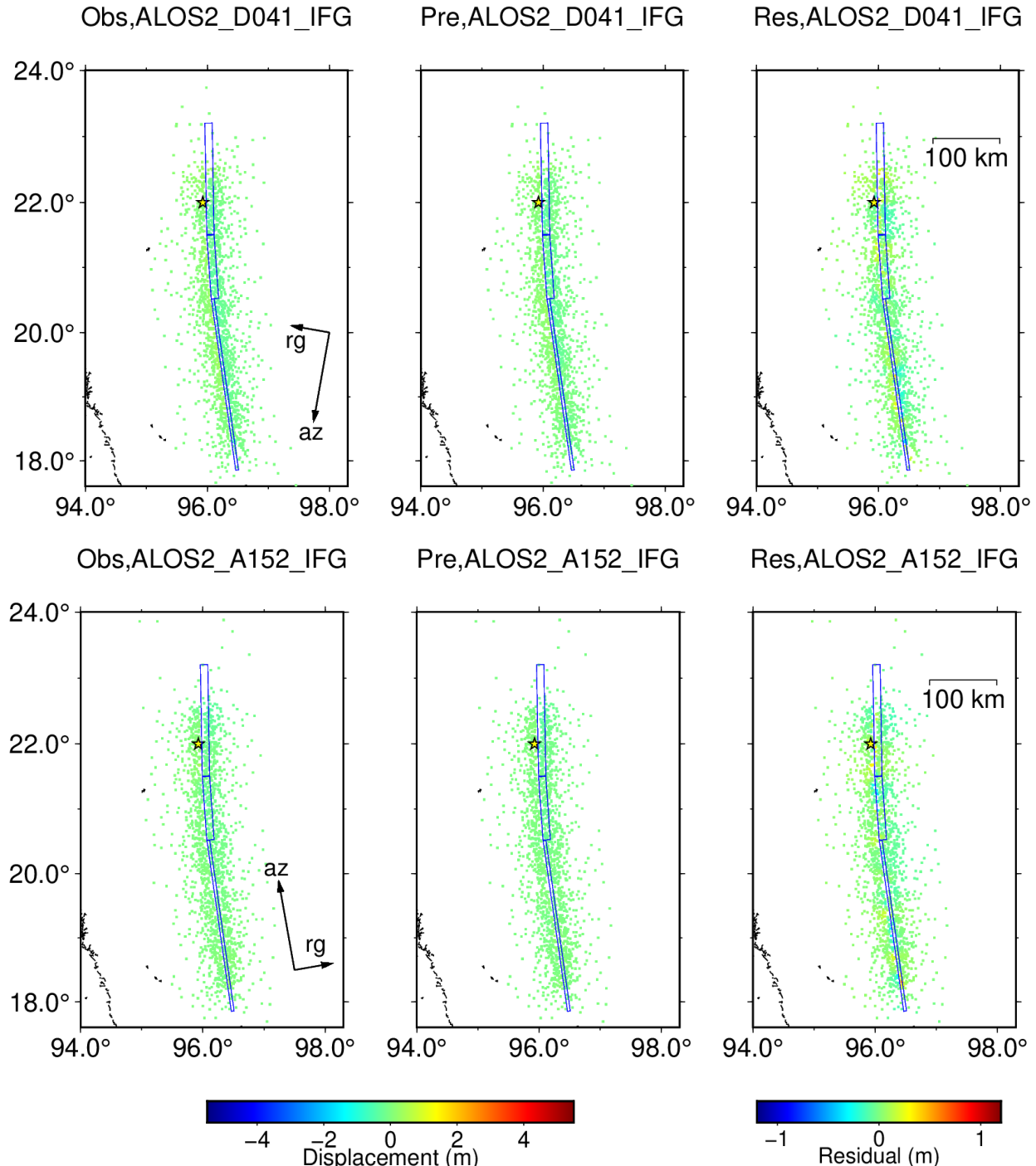
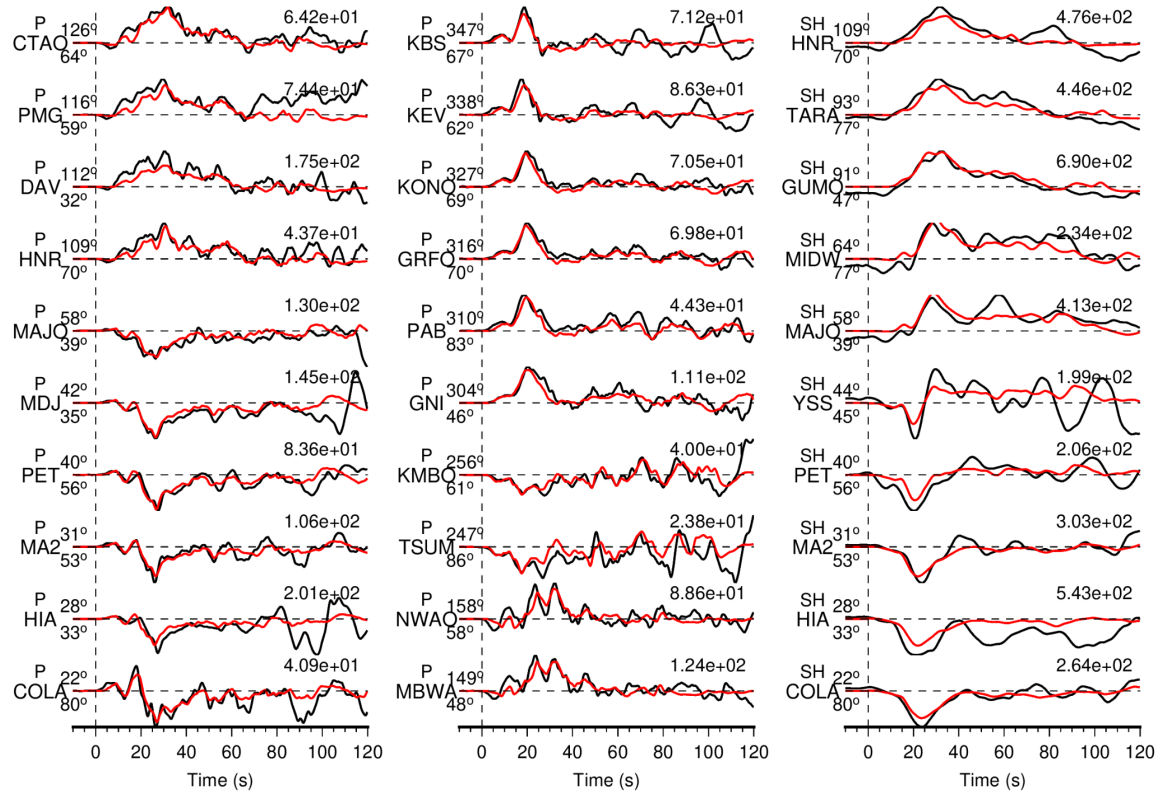


Fig. S16. The sub-sampled LuTan-1 SAR, Sentinel-2 SAR, and ALOS-2 InSAR data fits. The first column is the resampled static displacement (observation). The second column is the prediction by the preferred model. The third column is the residuals obtained by deducting the prediction from the observation. Blue boxes denote the fault planes adopted in joint finite fault inversion. Figures are named as {sensor name}_{orbit direction}{track number}_{measure}

type}. S2: Sentinel-2; LT: LuTan-1; ALOS2: ALOS-2; D: descending; A: ascending; RG: range offset; AZ: azimuth offset; NS: deformation in north-south direction; IFG: InSAR interferogram.



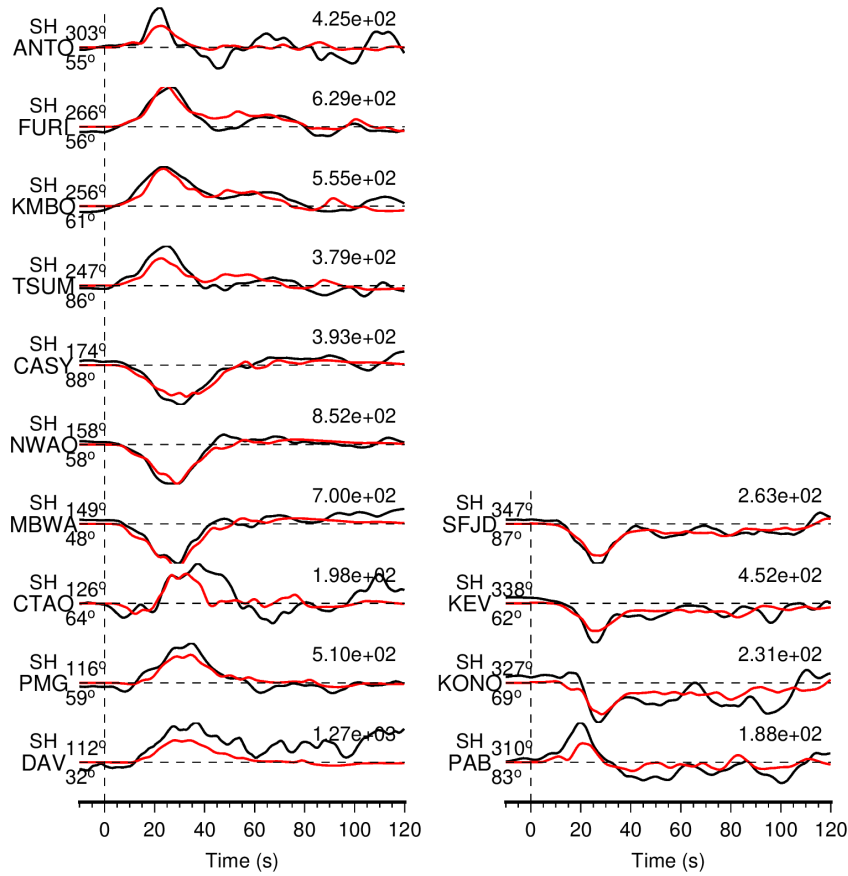


Fig. S17. Comparison between observed teleseismic broadband body wave waveforms (black lines) and synthetic seismograms (red lines) generated by the preferred model of the Mw 7.8 event. The wave type and the station name are shown to the left of each trace, along with azimuth (upper) and epicenter distance (lower) in degrees. The observed peak displacement in 10^{-6} m is denoted above the end of each trace.

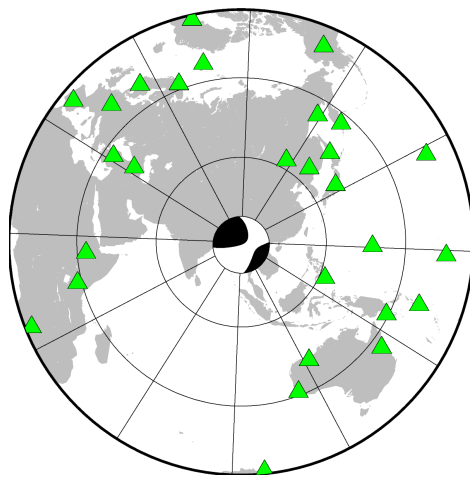


Fig. S18. Teleseismic stations recording broad-band body waves used in the joint FFI.

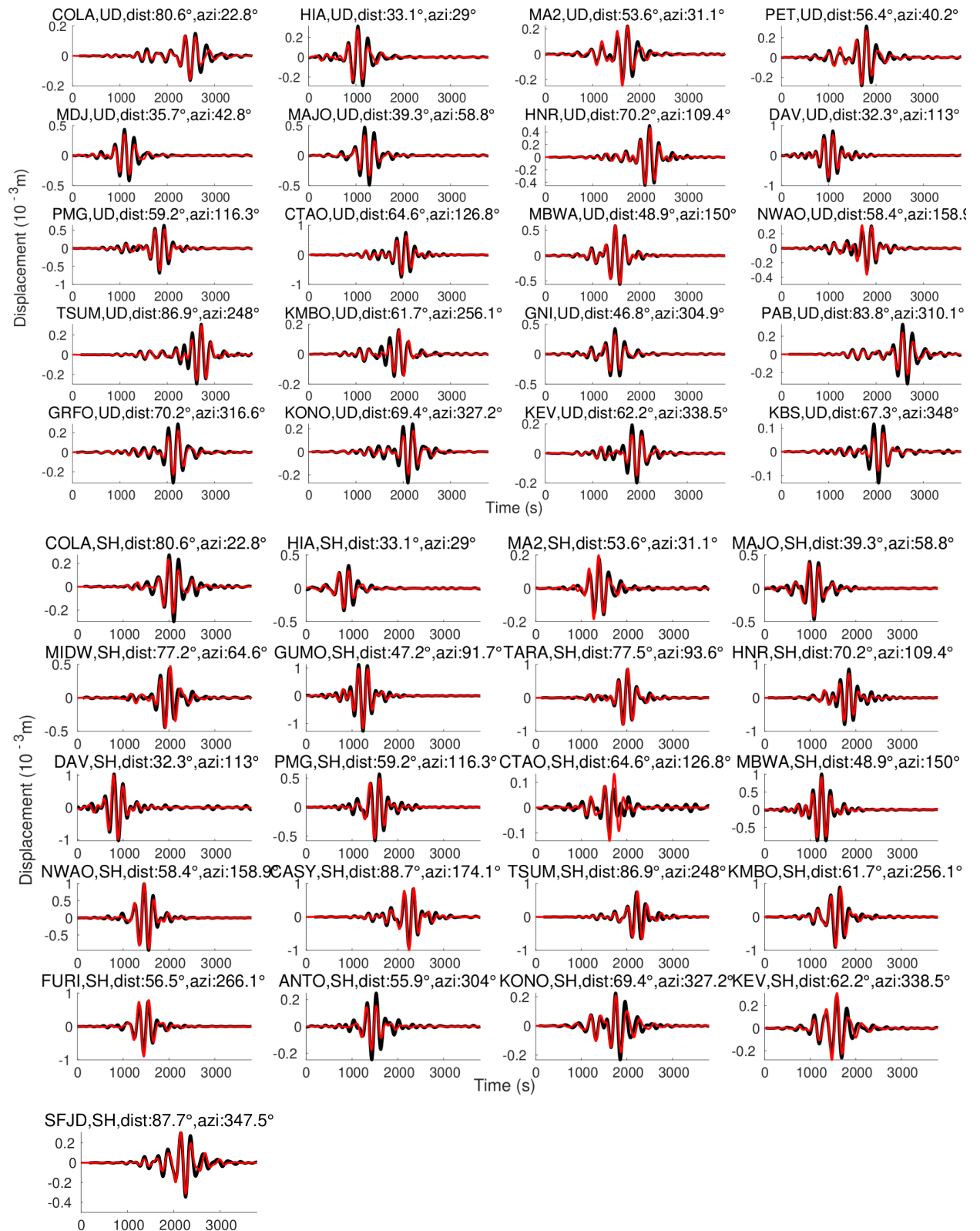


Fig. S19. Comparison between observed teleseismic long-period surface wave waveforms (black lines) and synthetic seismograms (red lines) generated by the preferred model of the Mw 7.8 event. The wave type and the station name are shown at the top of each trace, along with azimuth and epicenter distance in degree.

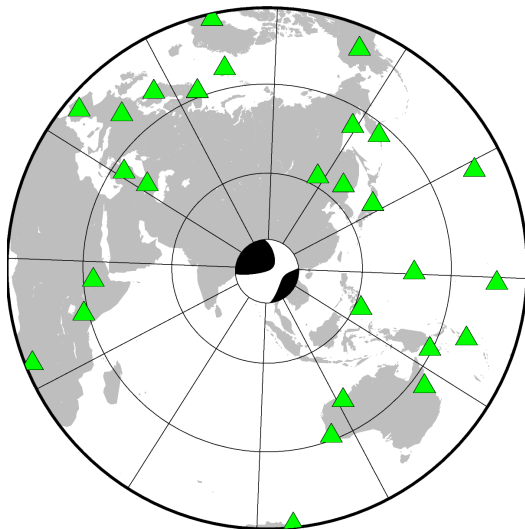


Fig. S20. Teleseismic stations recording long-period surface waves used in the joint FFI.

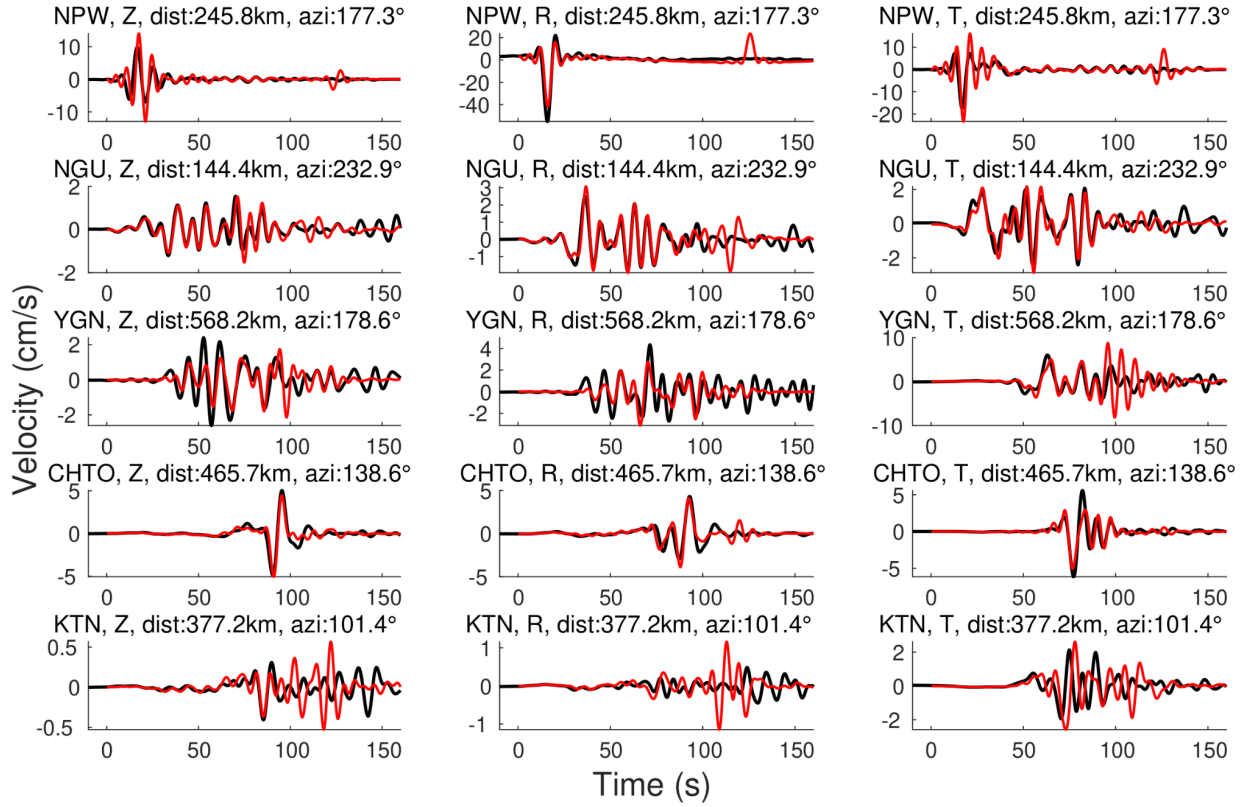


Fig. S21. Comparison between observed near-field strong motion station waveforms (black lines) and synthetic seismograms (red lines). The component and the station name are shown at the top of each trace, accompanied by azimuth in degree and epicenter distance in km. The unit of velocity waveforms is cm/s.

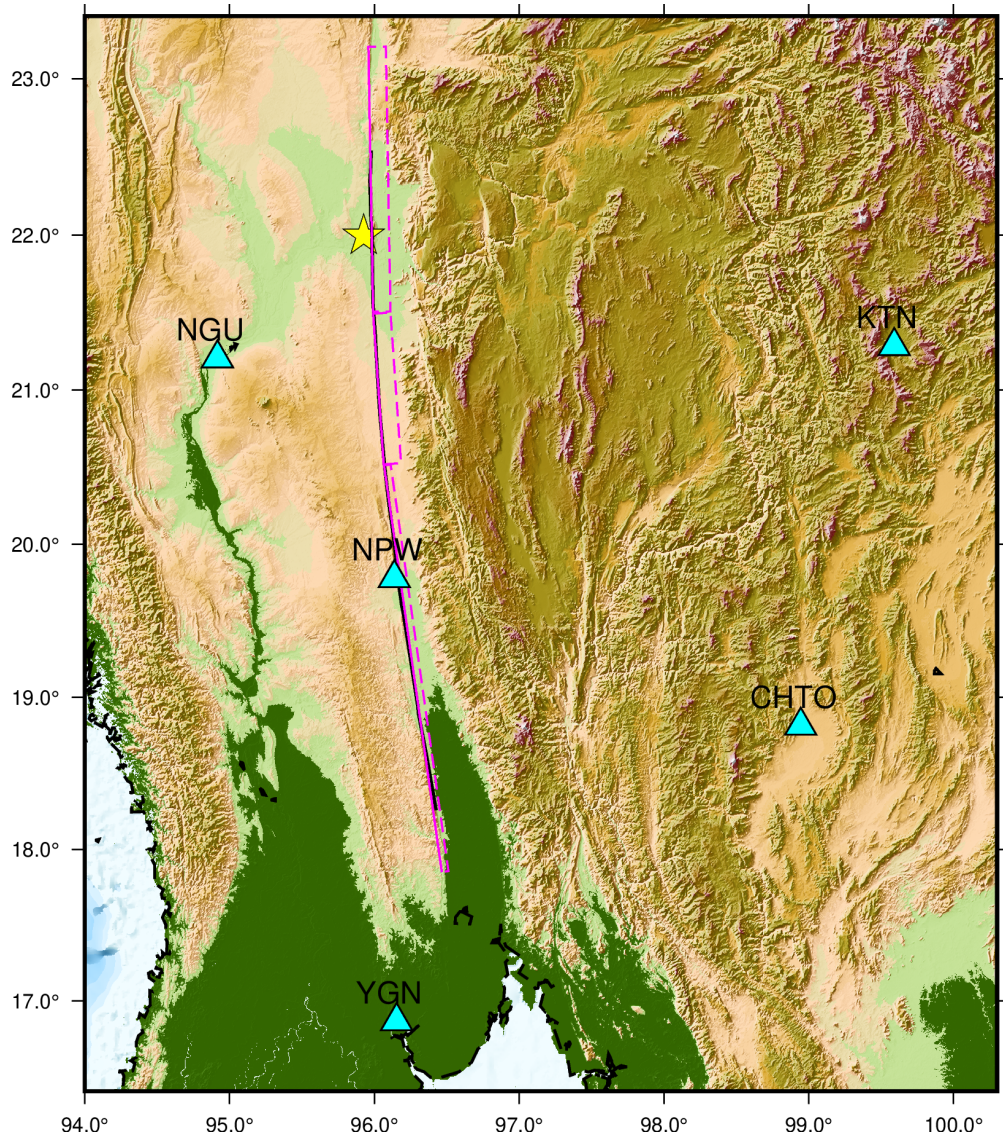


Fig. S22. The strong motion stations used in this study, with corresponding names. The thin blue line denotes the fault surface trace. The magenta boxes denote the finite fault model's boundaries.

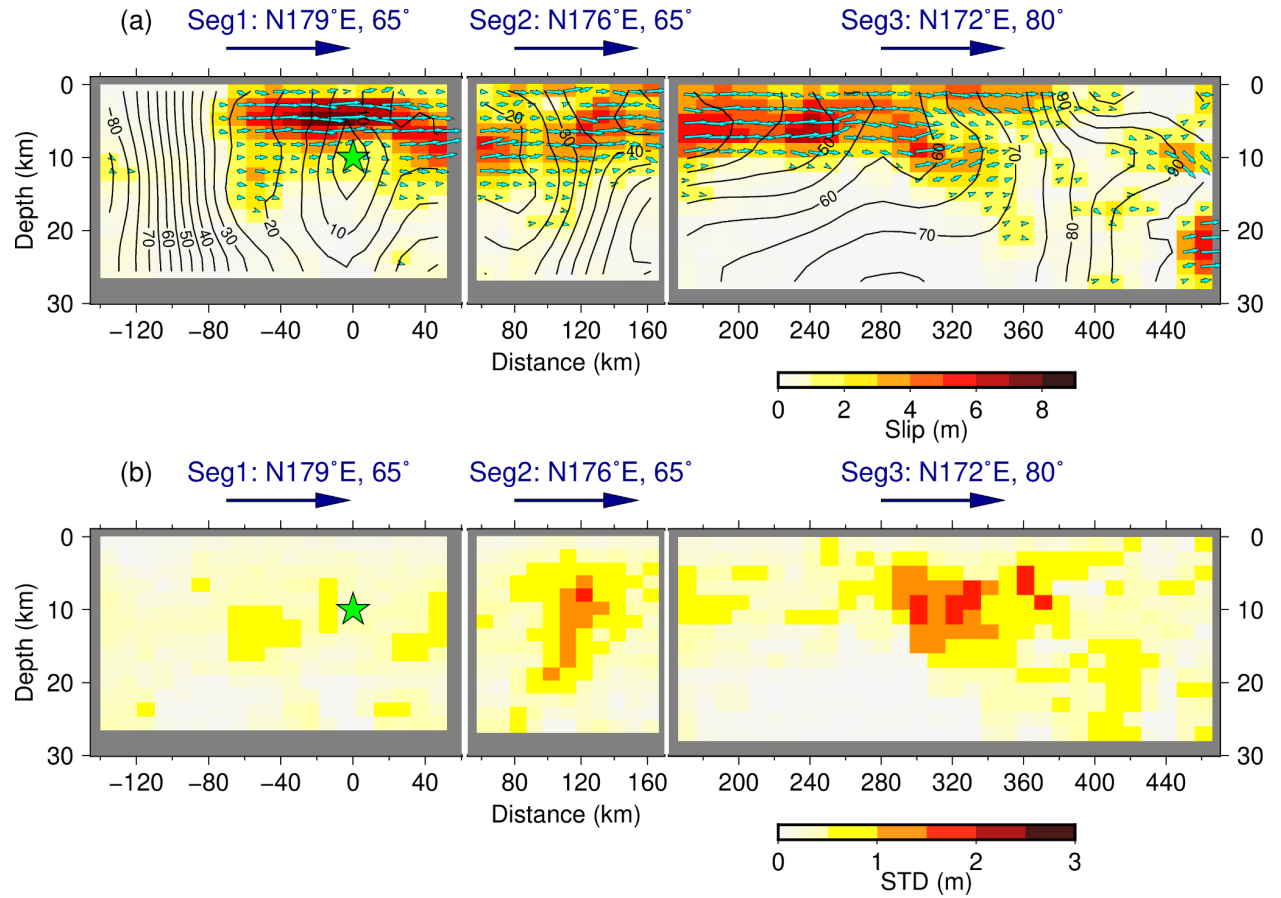


Fig. S23. Inversion results with ten different random seeds. (a) The average slip model of 10 plausible solutions. The segment index and orientation are shown on the top of each segment. The black contours denote the slip initiation time. The cyan arrows indicate the rake angle of each subfault. (b) The standard deviation of the fault slip among the 10 plausible slip models.

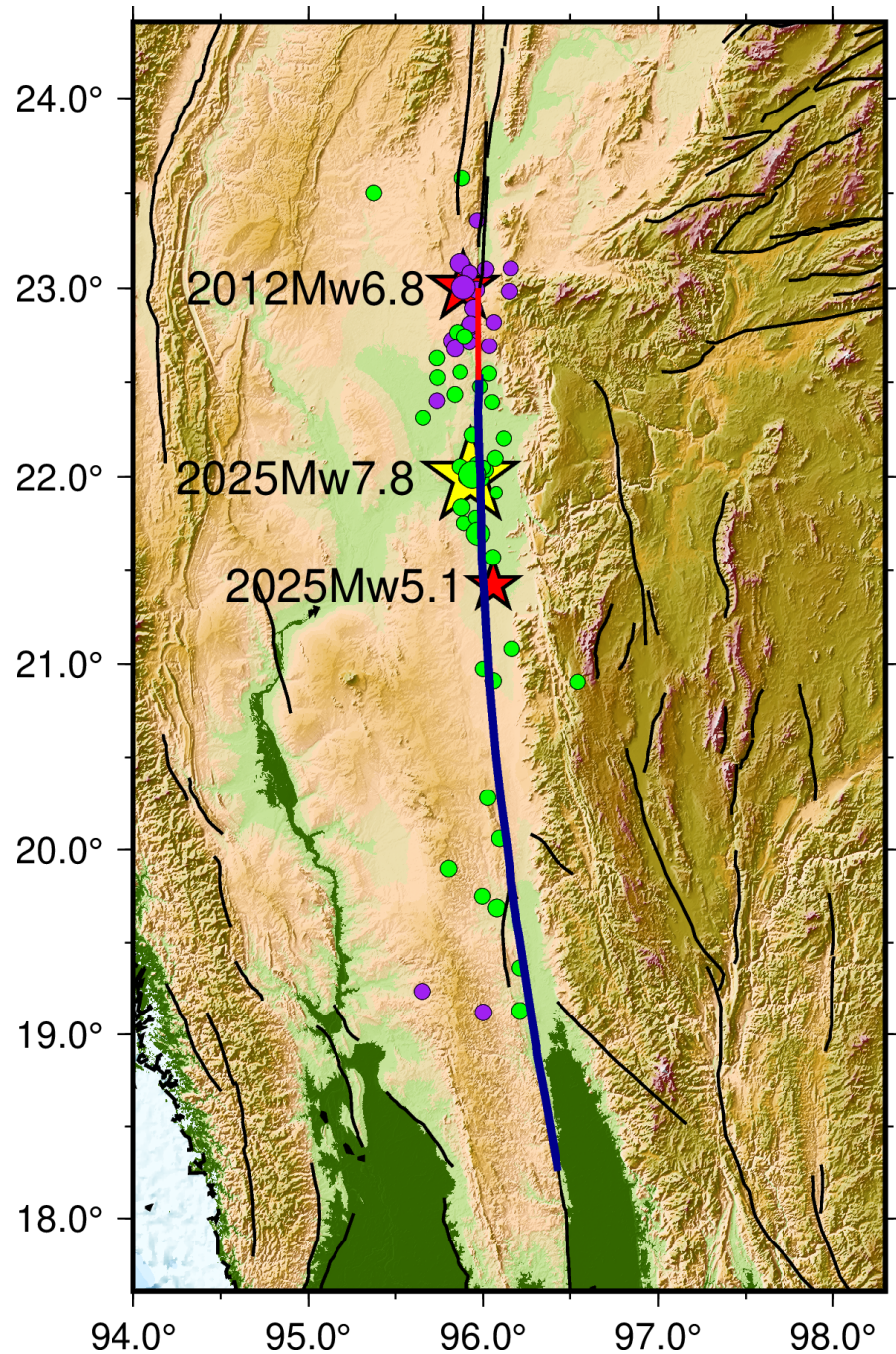


Fig. S24. The locations of aftershocks occurred between 2025.3.28 and 2025.4.07 (green dots, NEIC catalog), the 2025 mainshock surface rupture (dark blue line), the 2012 Mw 6.8 event (upper red star), and the 2025 Mw 5.1 aftershock (lower red star). Purple dots indicate aftershocks of the 2012 Mw 6.8 event (2012.11.11 to 2012.12.11). The red line denotes the southern rupture extent of the 2012 Mw 6.8 event documented by the field investigation (18). The 2025 Mw 5.1 event is also the EGF we used for Mach wave and Mach cone searching.

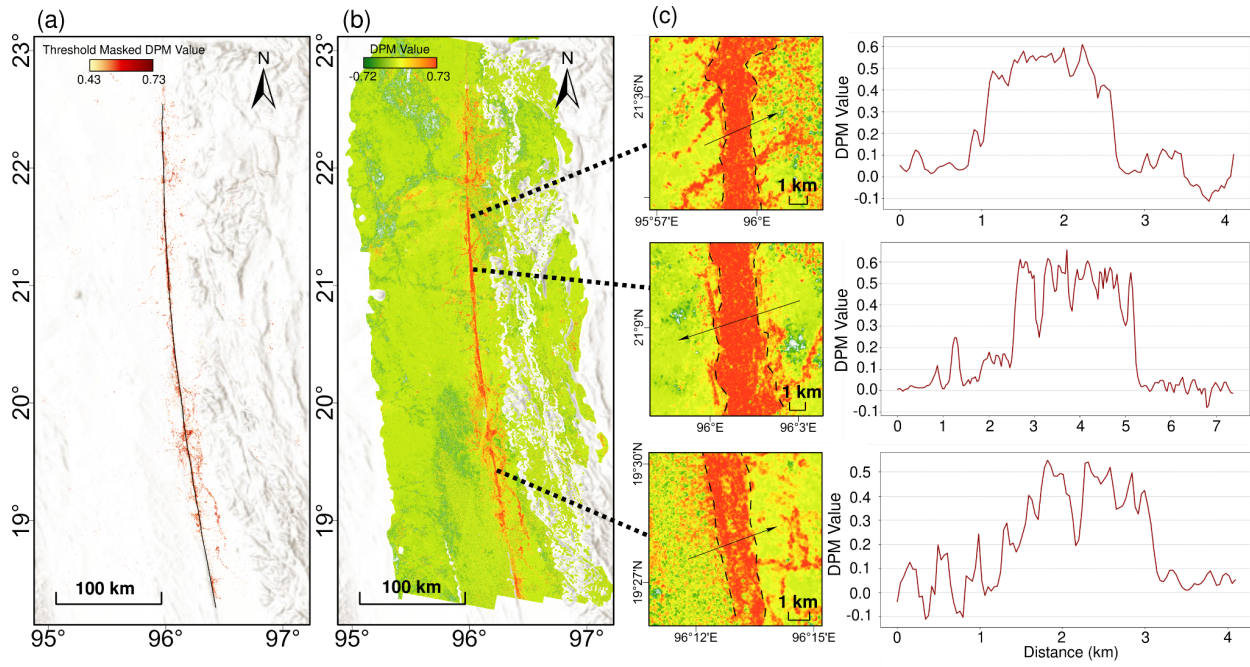


Fig. S25. Spatial correlation between high DPM values and Sagaing Fault traces, illustrating the extent of off-fault damage. (a) Distribution of high DPM values overlaid with mapped surface fault traces, showing a consistent 2–3 km wide damage zone aligned with the fault. Areas with DPM values below 0.43 are shown in white. (b) Regional-scale DPM distribution across the earthquake source area, highlighting widespread surface impacts. (c) DPM value profiles extracted from three selected subregions, illustrating cross-fault damage gradients and the spatial extent of off-fault destruction.

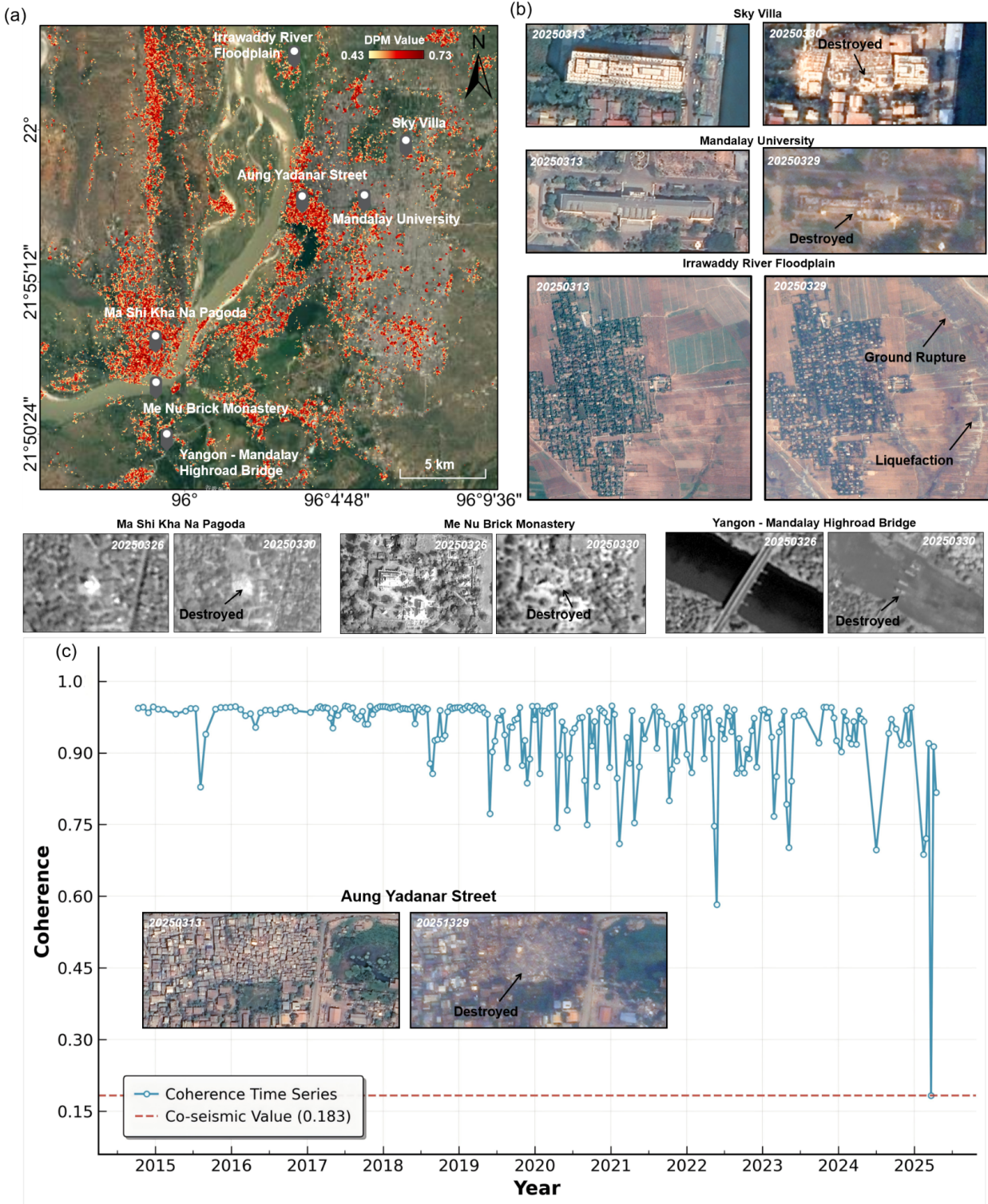
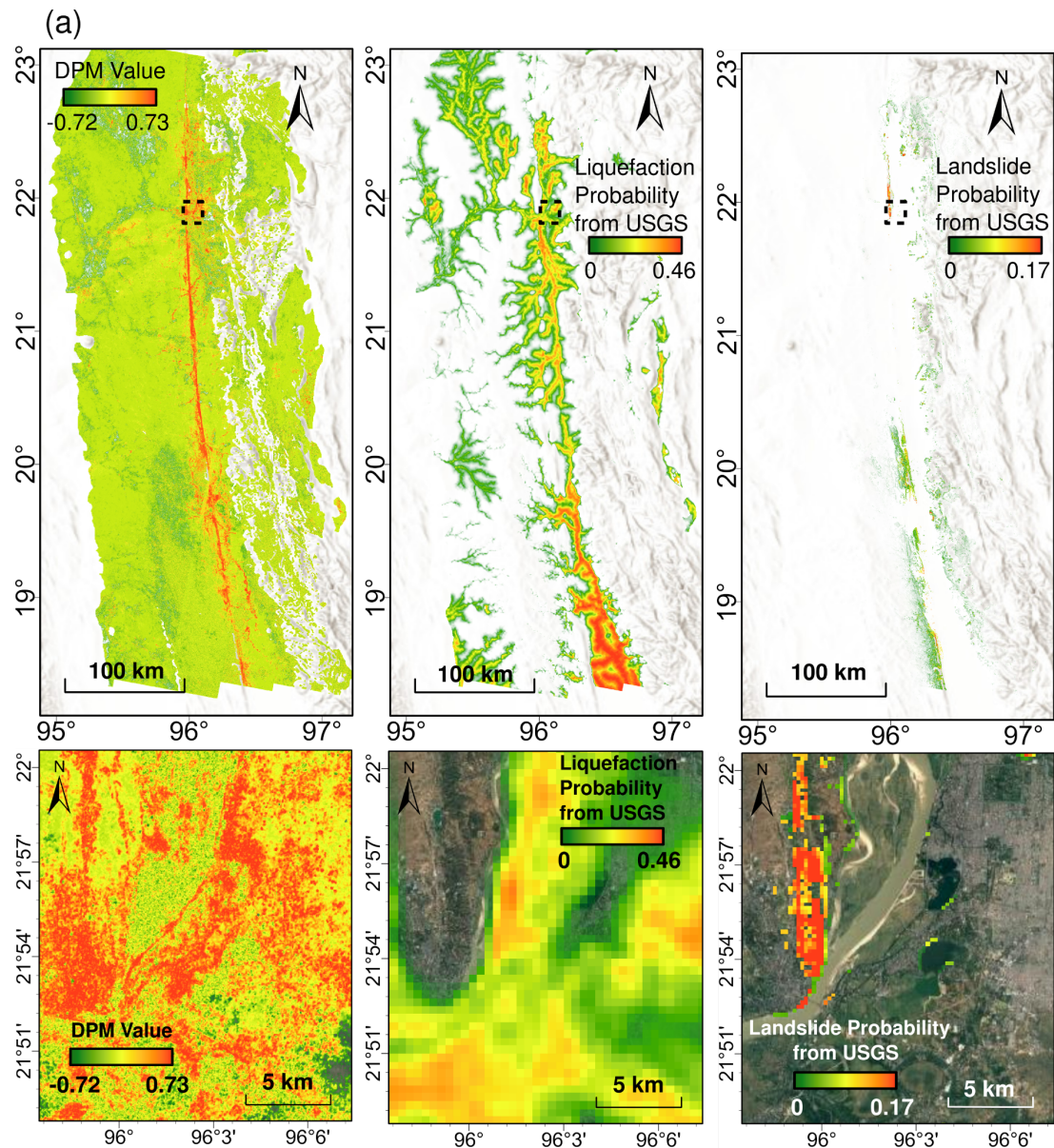


Fig. S26. Validation of DPM as an accurate and interpretable damage proxy using high-resolution optical imagery and Sentinel-1 InSAR coherence time series. (a) Spatial distribution of high DPM values in Mandalay city center and selected representative points. (b) Pre- and post-earthquake observations from Jilin-1, Gaofen-1/2/6 satellite imagery at the points

marked in (a), confirming building damage, liquefaction, and surface rupture. (c) Coherence time series for damaged buildings, showing high pre-event stability, a sharp drop during the earthquake, and gradual post-event recovery—characteristic of permanent scatterer response to seismic impact.



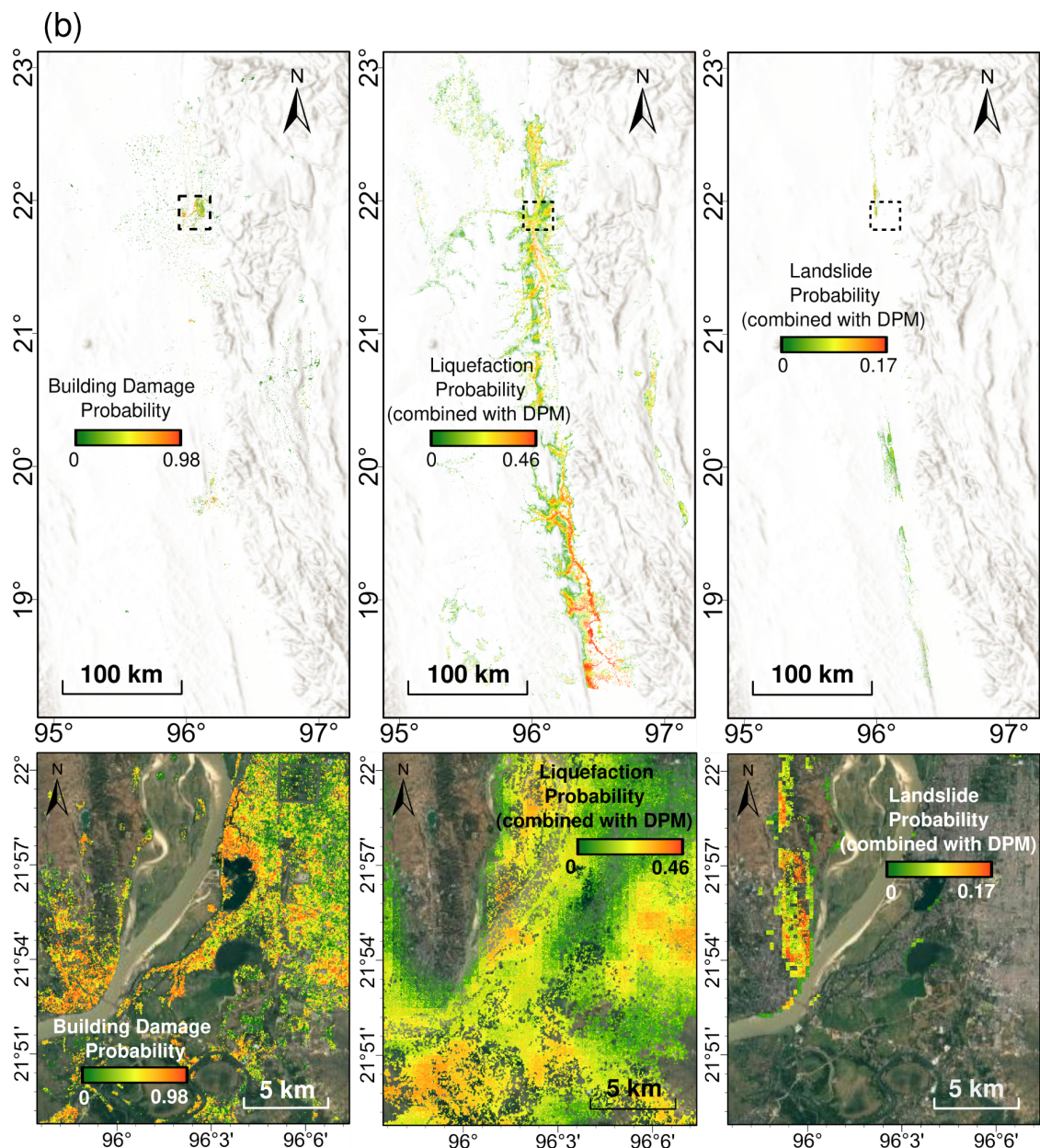


Fig. S27. Seismic multi-hazard and impact estimates before and after applying causal inference, illustrating enhanced resolution and improved hazard differentiation. (a) DPM results alongside original USGS landslide and liquefaction hazard models (upper panels), with zoomed-in views of Mandalay city to highlight the initial hazard distributions (lower panels). Dashed open boxes in the upper panels indicate the zoom-in areas. (b) Hazard probability maps after causal inference, showing improved detail and resolution in liquefaction and landslide features, with clearer separation between different hazard types.

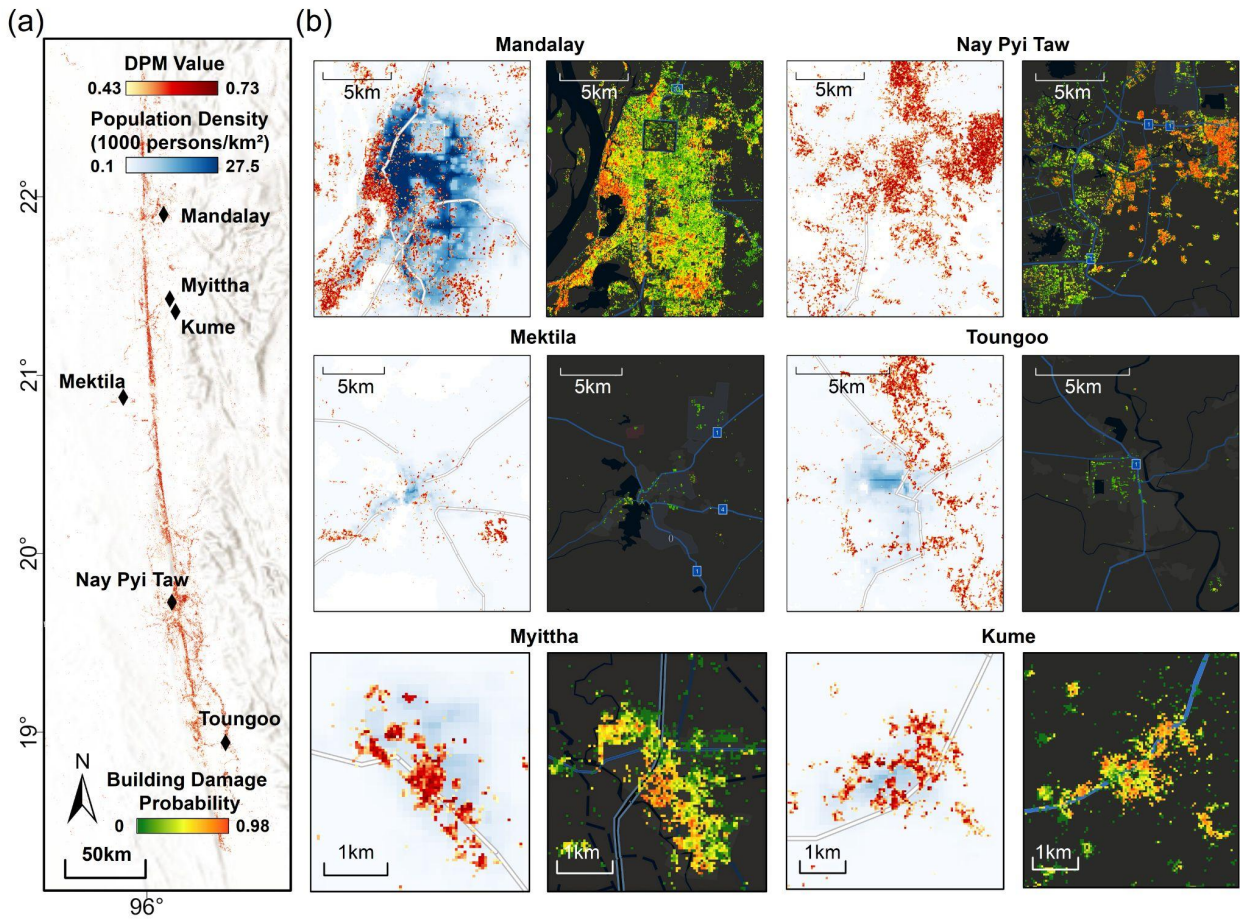


Fig. S28. Urban damage assessment near the fault zone, utilizing high-value DPM and building damage probability maps. (a) Overview of the DPM in the city center near the fault zone. (b) High-value DPM distribution and building damage probability map after causal inference, highlighting areas of high-probability damage in cities located near fault zones, as marked in (a). In each panel, the left column shows the DPM with a base map of population distribution, while the right column presents the building damage probability with a base map from OpenStreetMap.

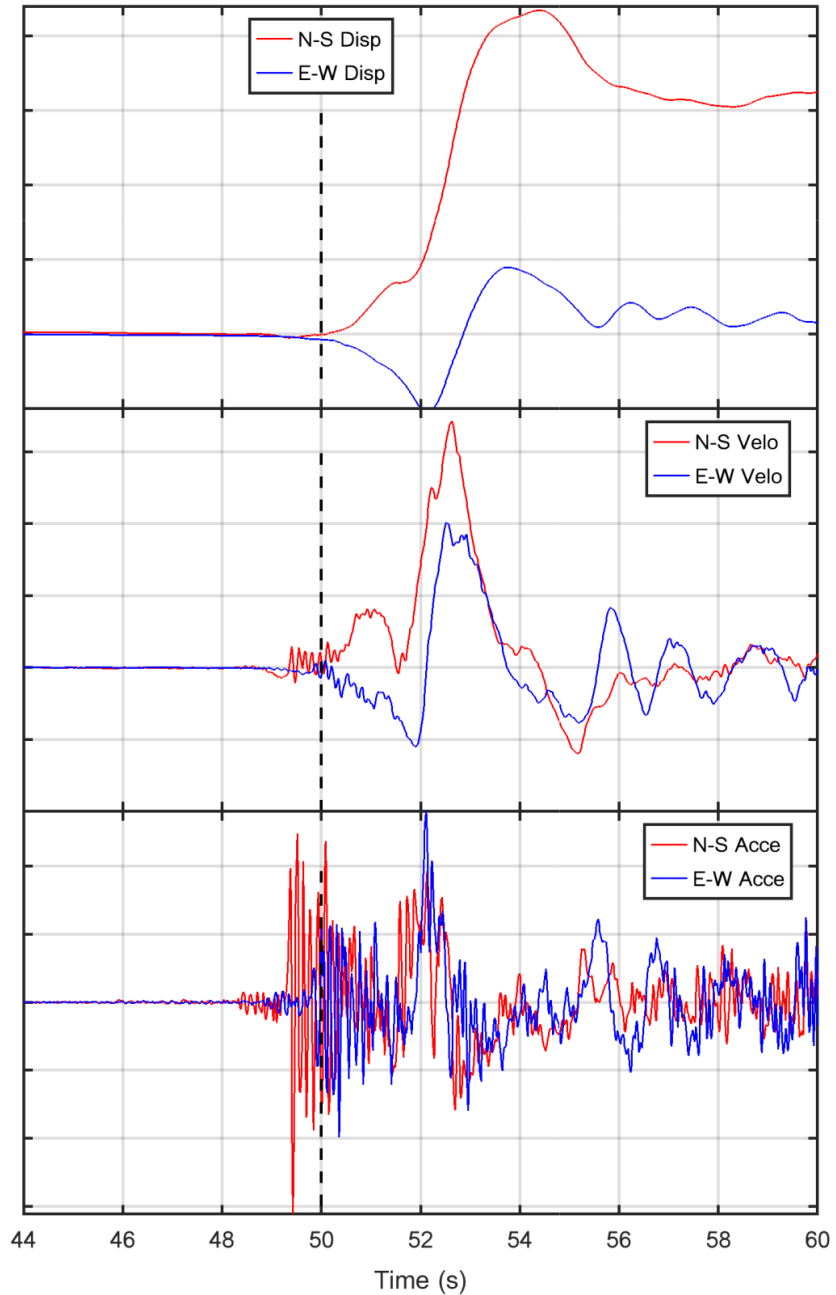


Fig. S29. Zoomed-in view of displacement (top), velocity (middle), and acceleration (bottom) waveforms at GE.NPW. The vertical dashed line marks the picked onset time of ground displacement (50 s).

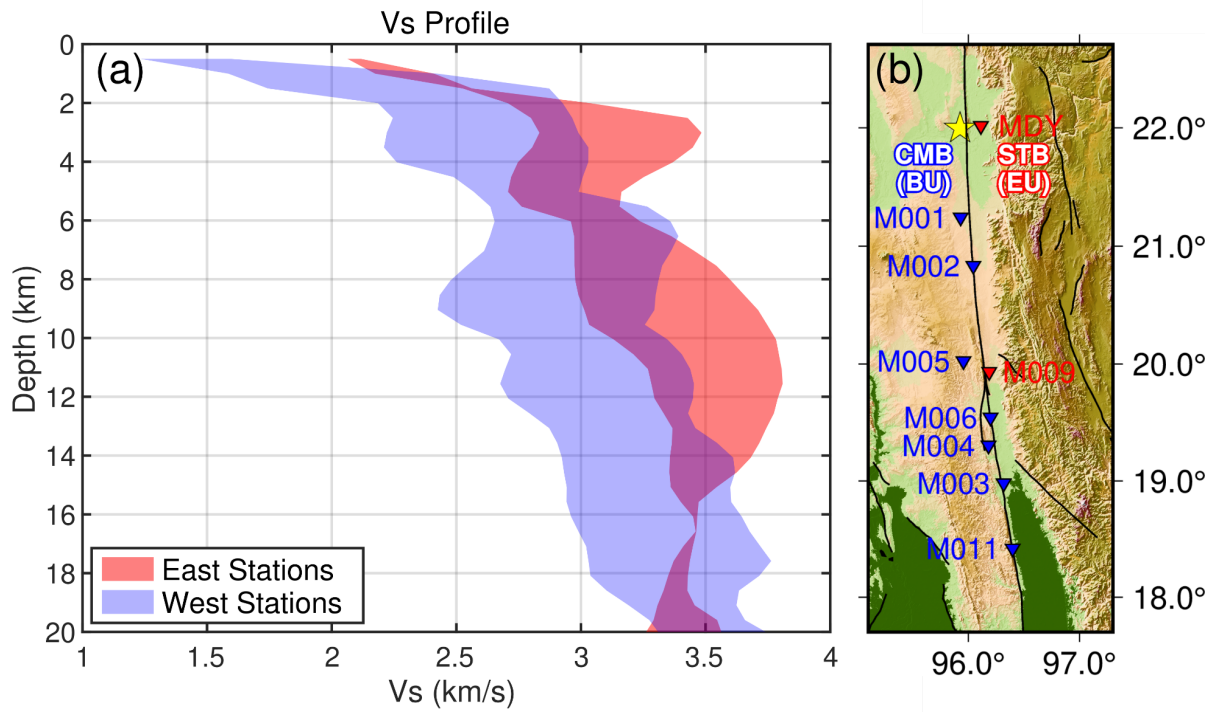


Fig. S30. Bimaterial contrast across the Sagaing Fault. (a) One-dimensional shear wave velocity (V_s) profiles beneath near-fault stations (5). The red shaded area indicates the range (maximum to minimum) of V_s profiles from stations located east of the Sagaing Fault (MDY, M009), while the blue shaded area represents the V_s range for stations on the west side of the fault (M001, M002, M003, M004, M005, M006, M011). (b) Map showing the locations of the stations plotted in (a). Red triangles mark stations on the eastern side of the fault, and blue triangles mark those on the western side. CMB (BU): Central Myanmar Basin in Burma Plate; STB (EU): Shan-Thai Block in Eurasian Plate.

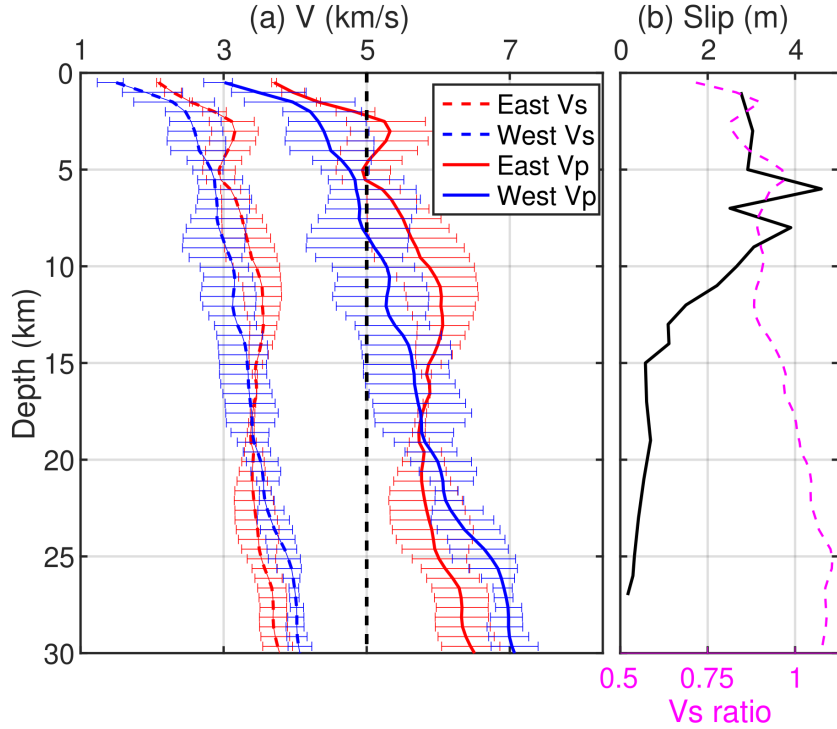


Fig. S31. Vs, Vp, and slip profile as a function of depth. (a) One-dimensional Vs and Vp profiles beneath near-fault stations (5). The red dashed line indicates the average Vs beneath stations located east of the Sagaing Fault (MDY, M009; fig. S30b), with the error bar indicating the range (maximum to minimum). The blue dashed line indicates the average Vs beneath stations located west of the Sagaing Fault (M001, M002, M003, M004, M005, M006, M011; fig. S30b), with the error bar indicating the range (maximum to minimum). Solid red and blue lines denote the same station groupings for Vp profile. The vertical black dashed line denotes the average rupture speed of the south branch, 5 km/s. (b) Depth profile of the average coseismic slip (black line), plotted alongside the Vs ratio (west/east; magenta line) derived from the blue and red dashed lines in panel (a), highlighting the bimaterial contrast across the fault.

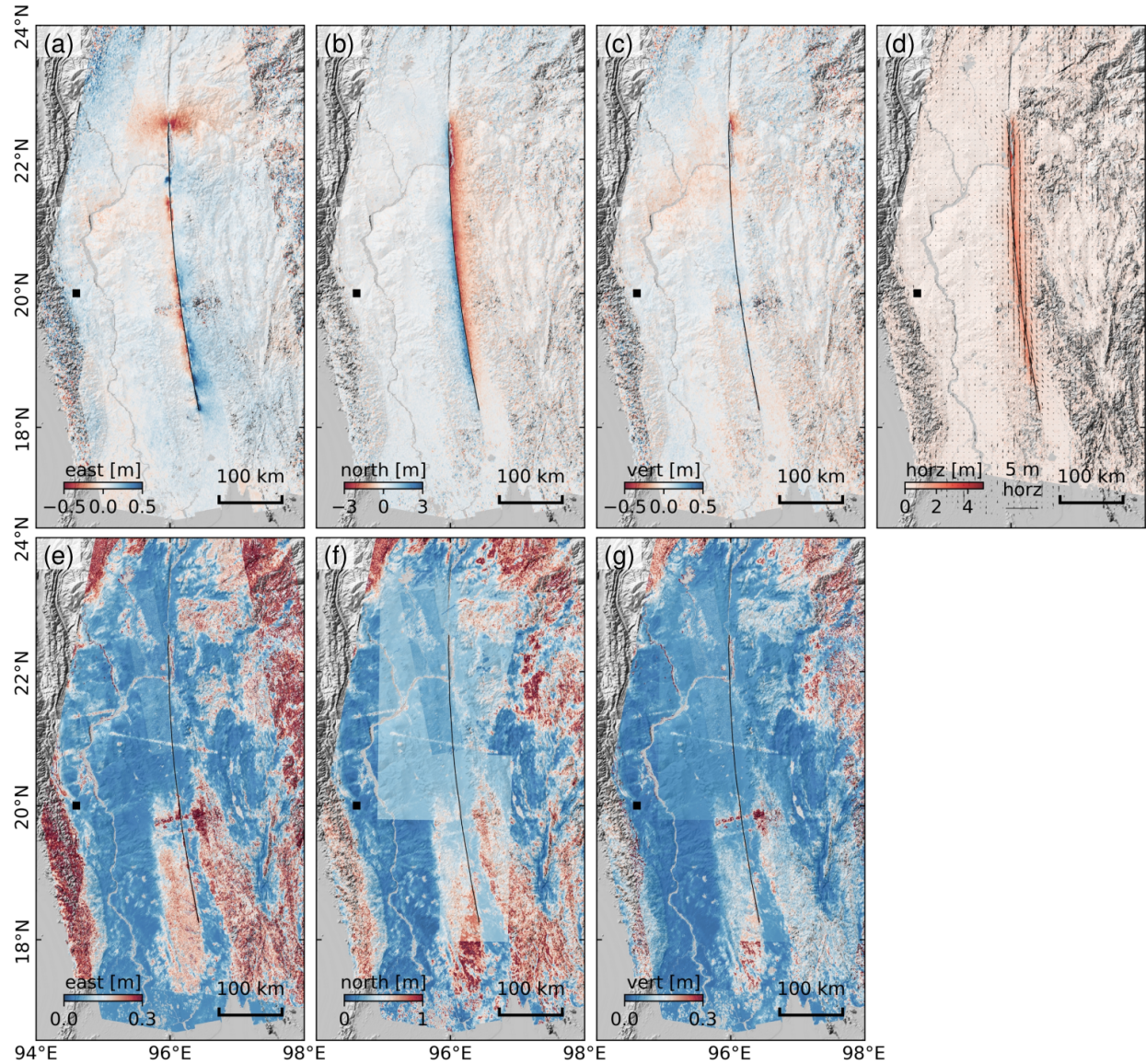


Fig. S32. The 3D ground deformation map inferred from SAR and optical satellite data. (a-c) Ground deformation in the east-west, north-south, and up-down directions, respectively. (d) Horizontal deformation with color representing magnitude and arrows representing magnitude and orientations. (e-g) Standard deviation of the estimated ground deformation in the east-west, north-south, and up-down directions, respectively. Black square: reference point at [N20.0°, E94.6°].

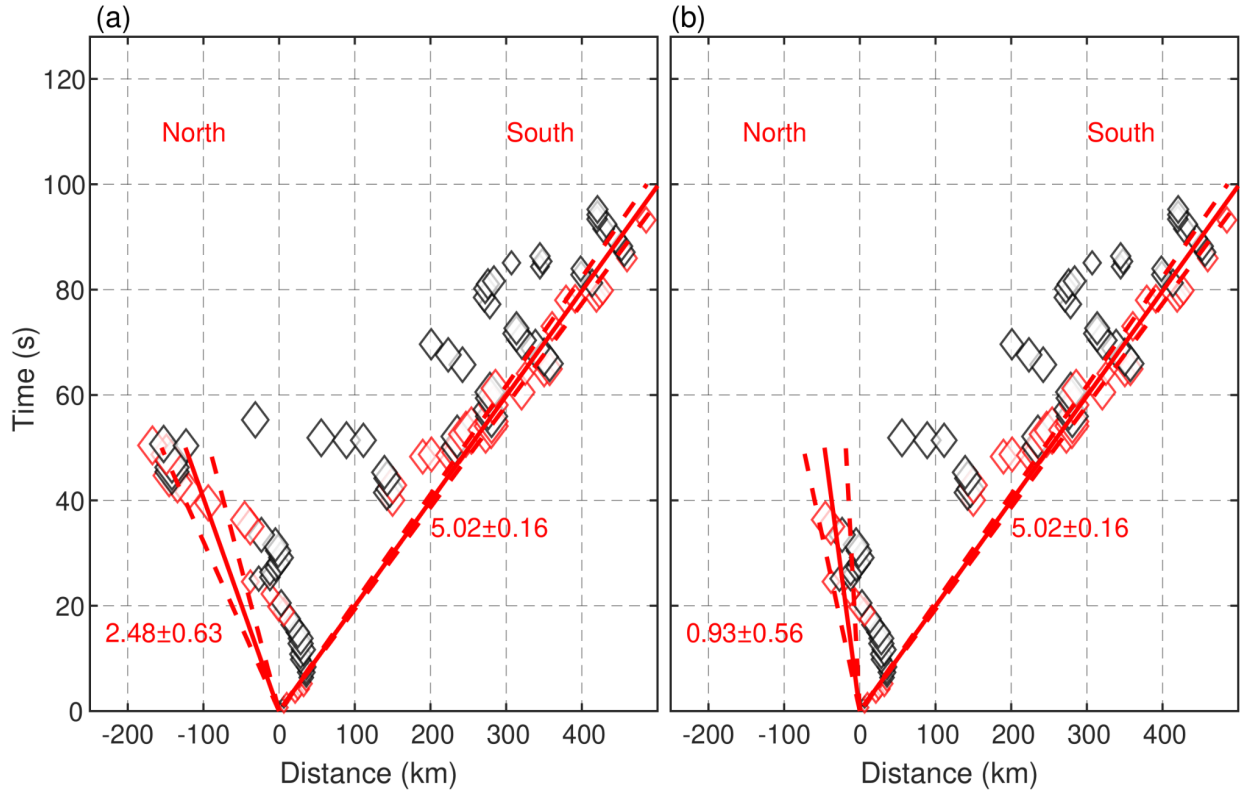


Fig. S33. Rupture speeds measured by the EU array. (a) Estimated northern rupture speed (2.48 km/s) before removing northern radiators after 40 s. (b) Estimated northern rupture speed (0.93 km/s) after removing northern radiators after 40 s.

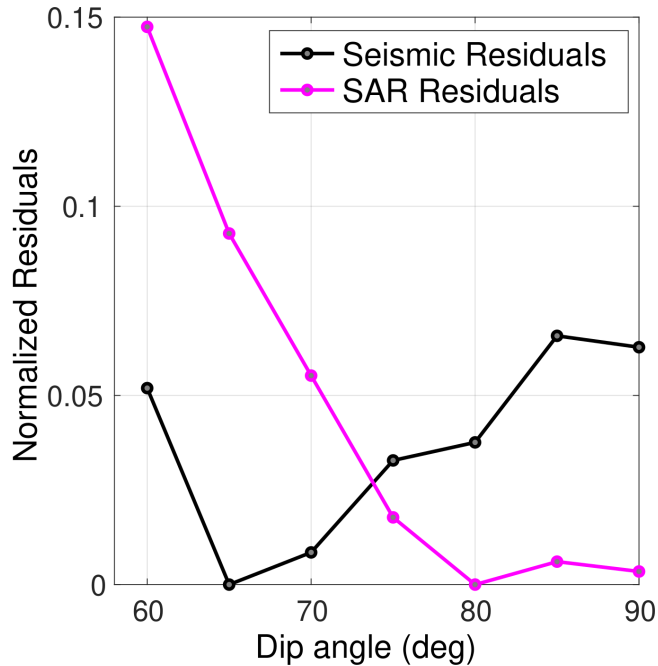


Fig. S34. Normalized residuals ([residual of each inversion - minimum residual of all inversions] / minimum residual of all inversions) versus fault dip angles.

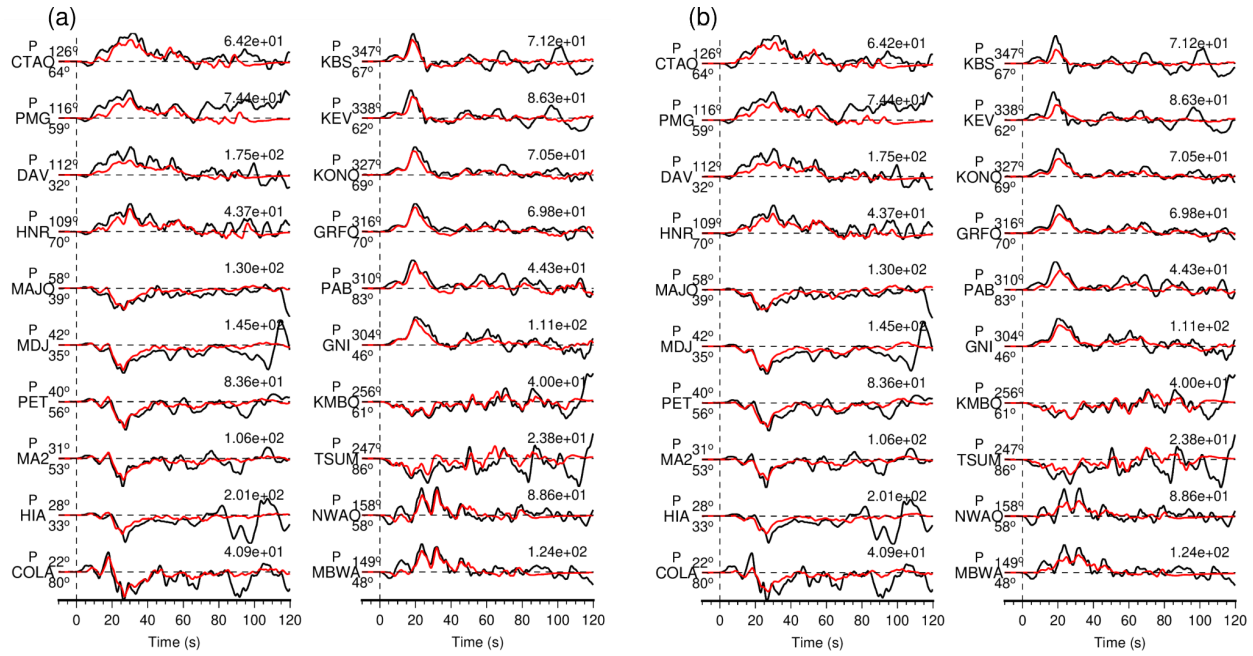
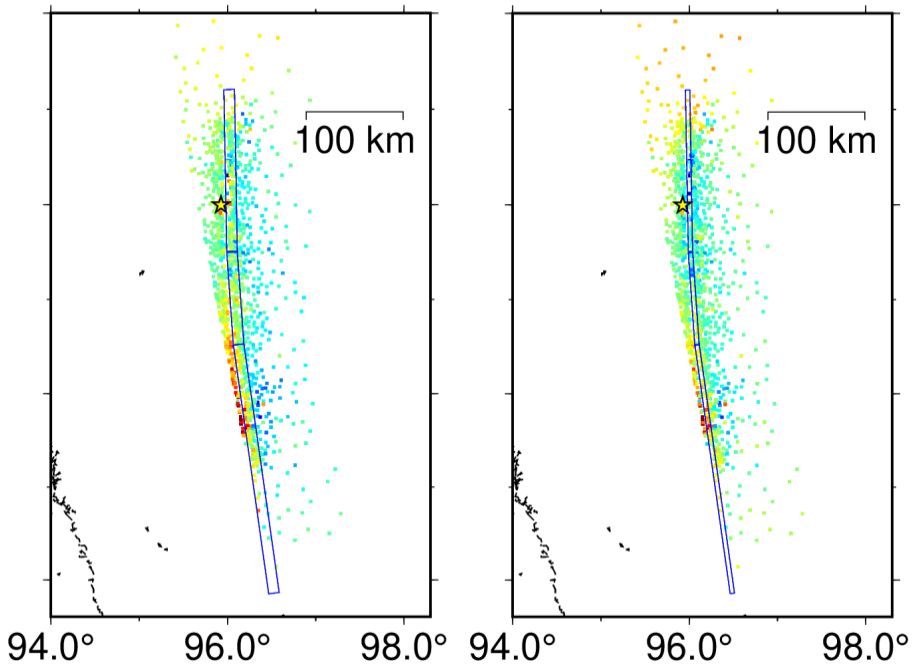
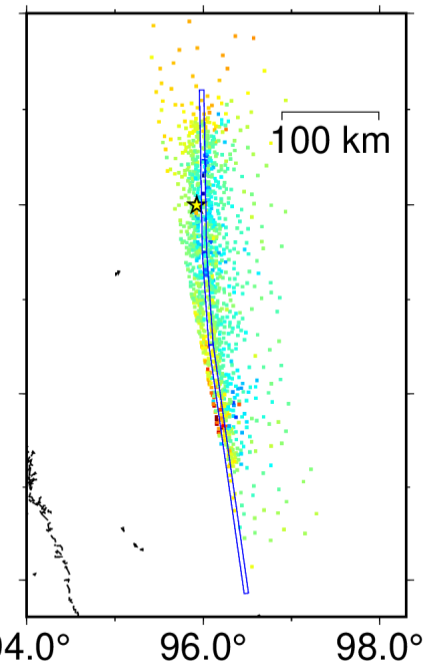


Fig. S35. (a) Teleseismic P fits of the 65°-dip-fault. (b) Teleseismic P fits of the 80°-dip-fault.

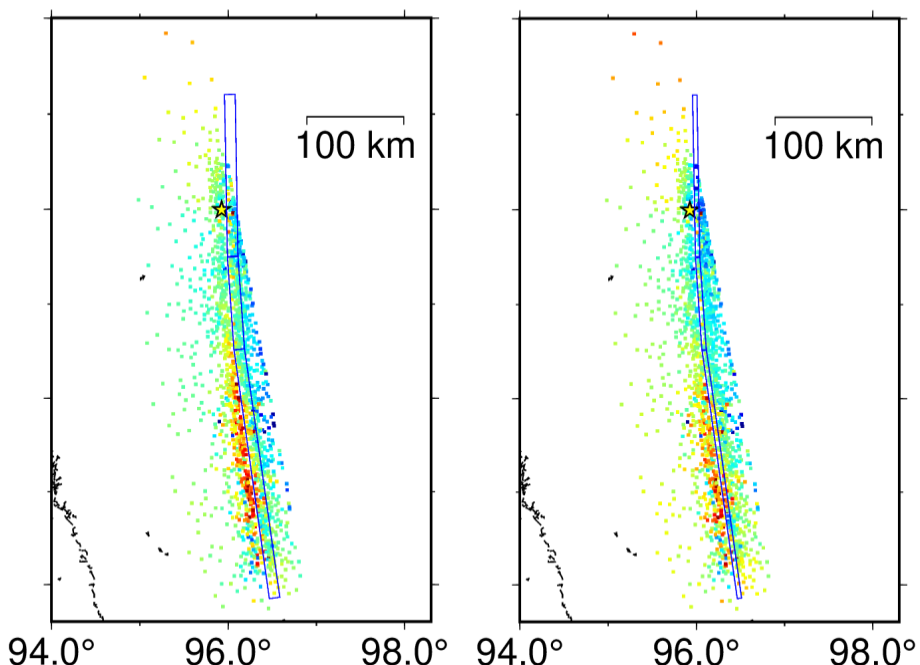
(a) Residuals,A070AZ



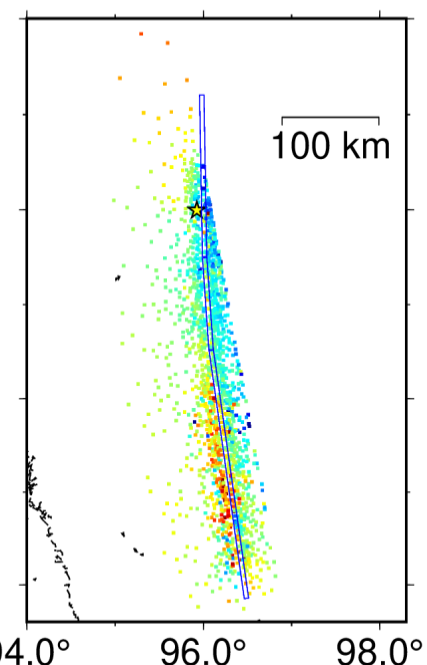
(b) Residuals,A070AZ



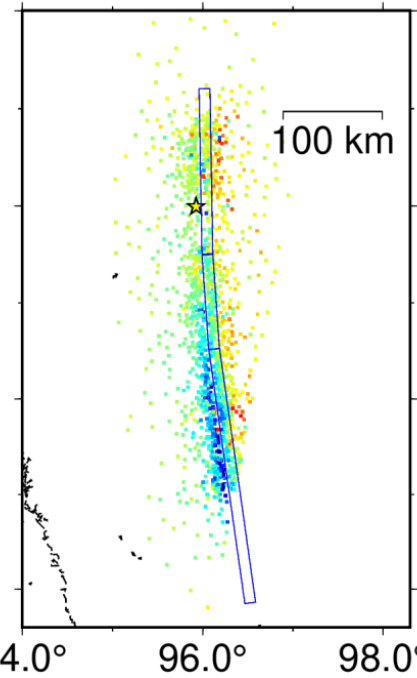
(c) Residuals,A143AZ



(d) Residuals,A143AZ



(e) Residuals,D106AZ



(f) Residuals,D106AZ

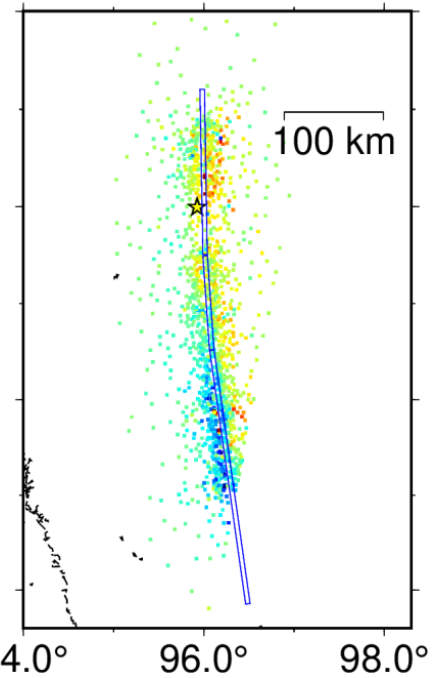


Fig. S36. (a), (c), (e): the residuals of the 65° -dip-fault. (b), (d), (f): the residuals of the 80° -dip-fault.

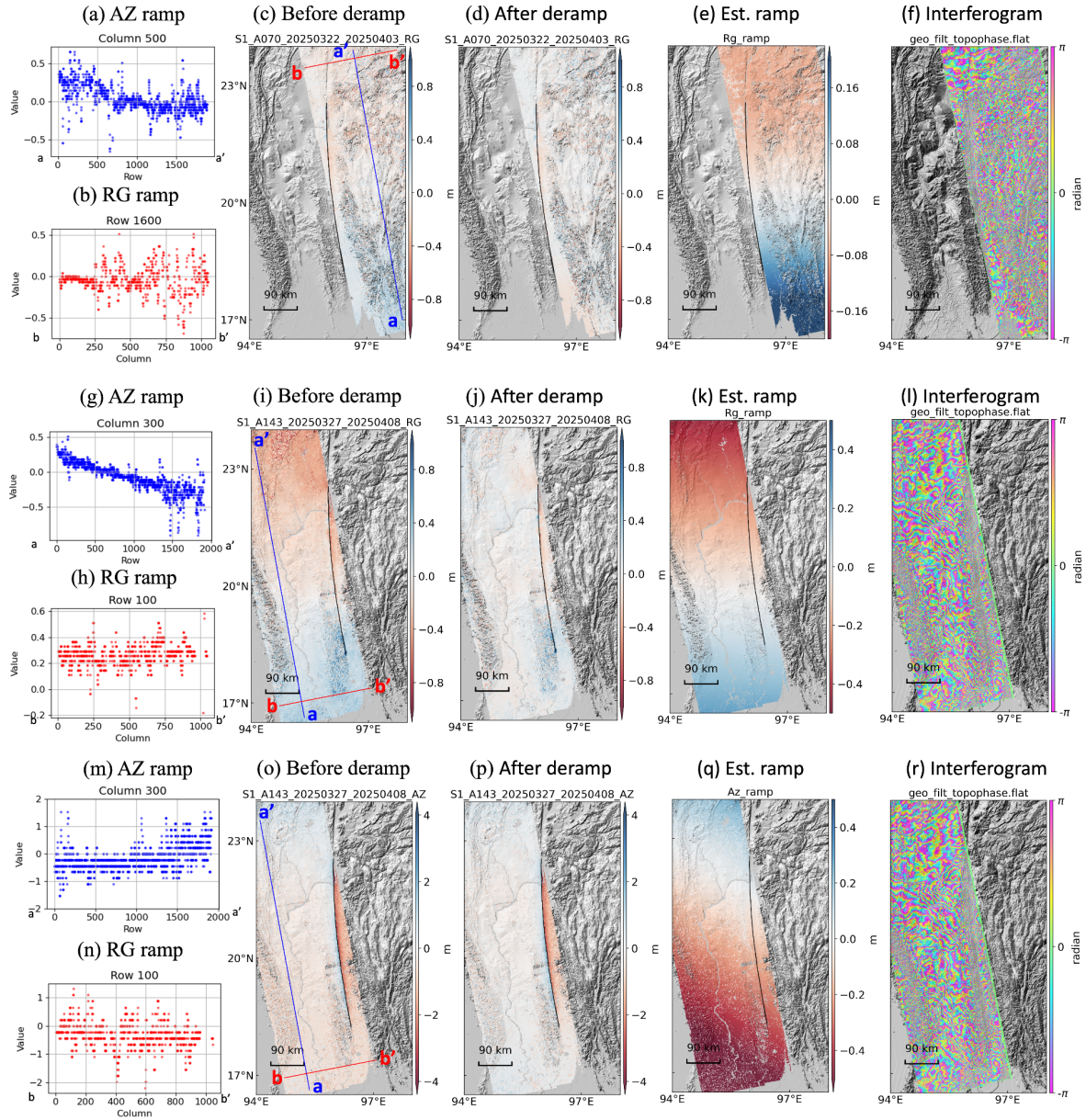


Fig. S37. The impact of ionospheric ramps on Sentinel-1 speckle tracking. (a-b) Profile along the Sentinel-1 ascending track 70 range offset, with profile locations marked in (c). (c-d) offset before and after deramping. (d) estimated quadratic ramp along the azimuth direction. (e) wrapped interferogram. (g-l) Same as (a-f) but for Sentinel-1 ascending track 143 range offsets, with the ramp type as linear along the azimuth direction. (m-r) Same as (a-f) but for Sentinel-1 ascending track 143 azimuth offsets, with the ramp type as linear along both range and azimuth directions.

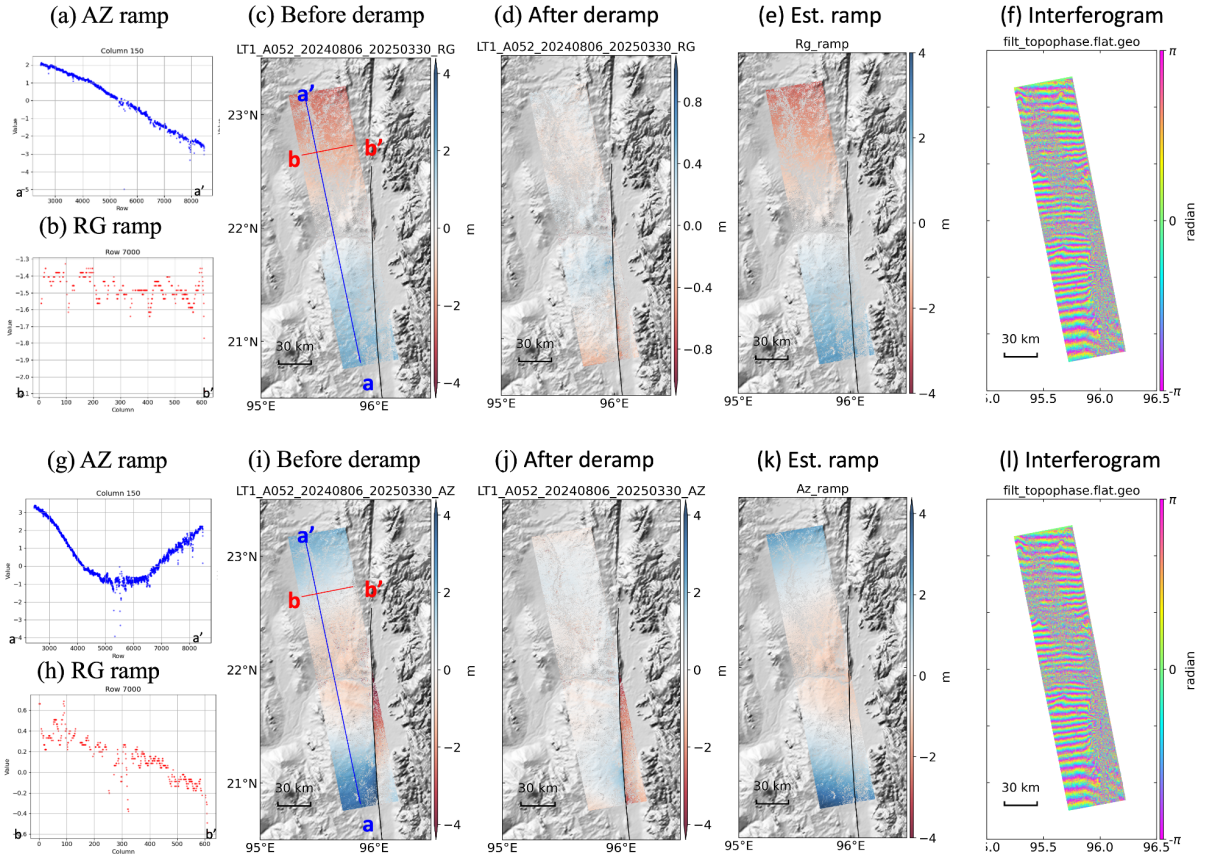
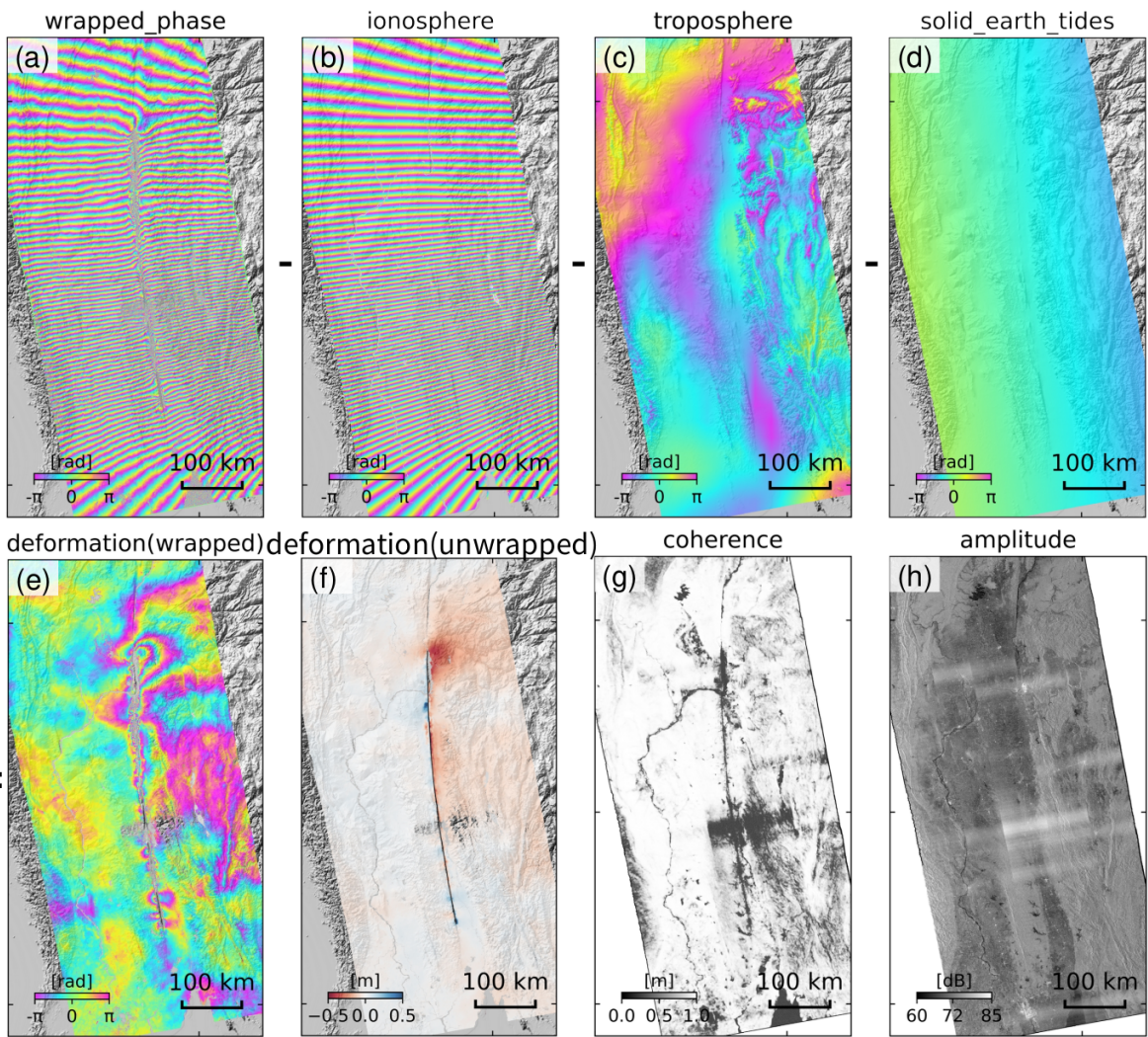


Fig. S38. The impact of ionospheric ramps on LuTan-1 speckle tracking. Same as Fig. S37 but for the LuTan-1 ascending track 52 range (upper panel) and azimuth (lower panel) offsets, respectively. The estimated ramp type for the range offset is linear along the azimuth direction, and for the azimuth offset cubic along the azimuth direction and linear along the range direction.

ALOS2_A152_IFG
20250211_20250408



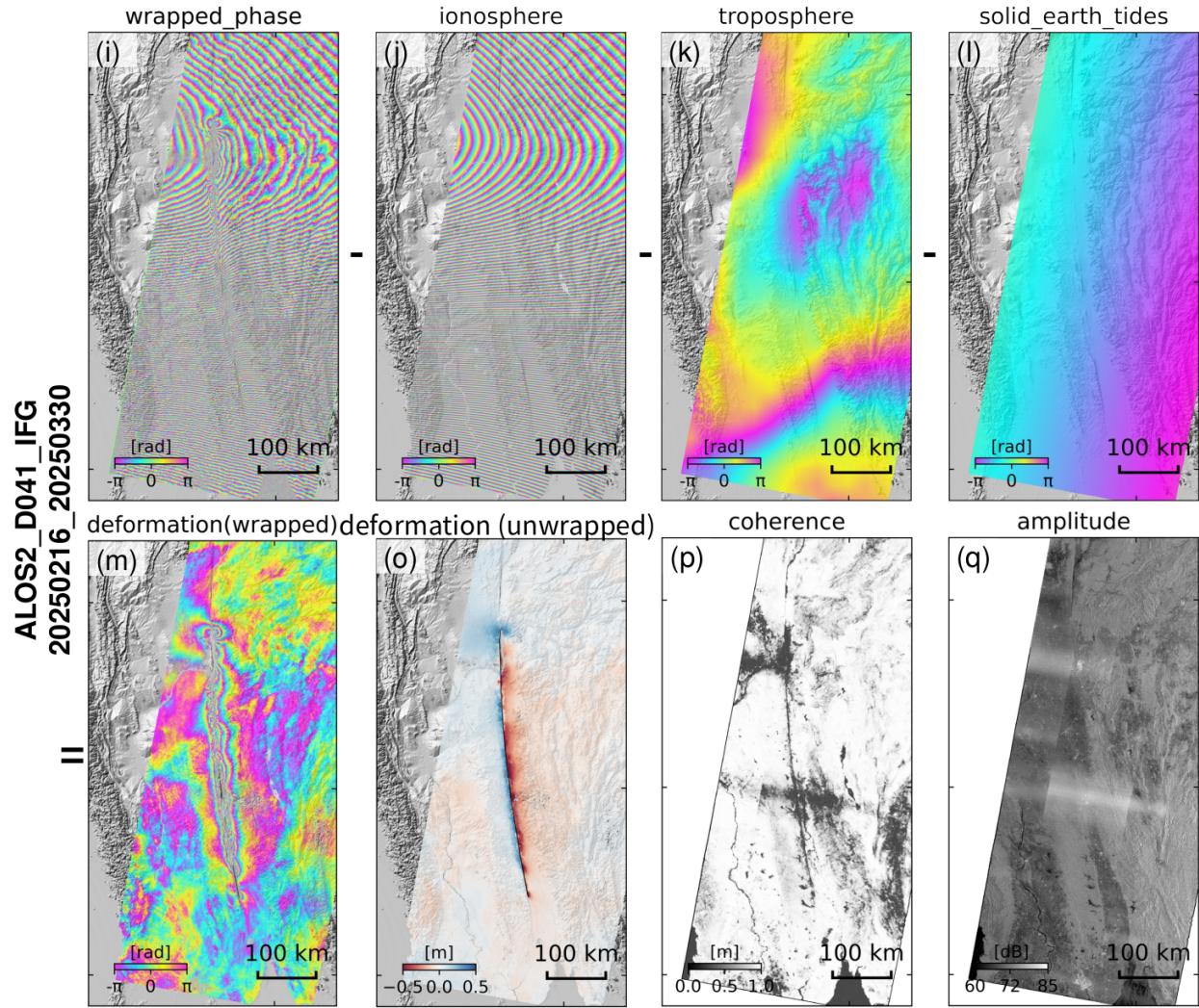
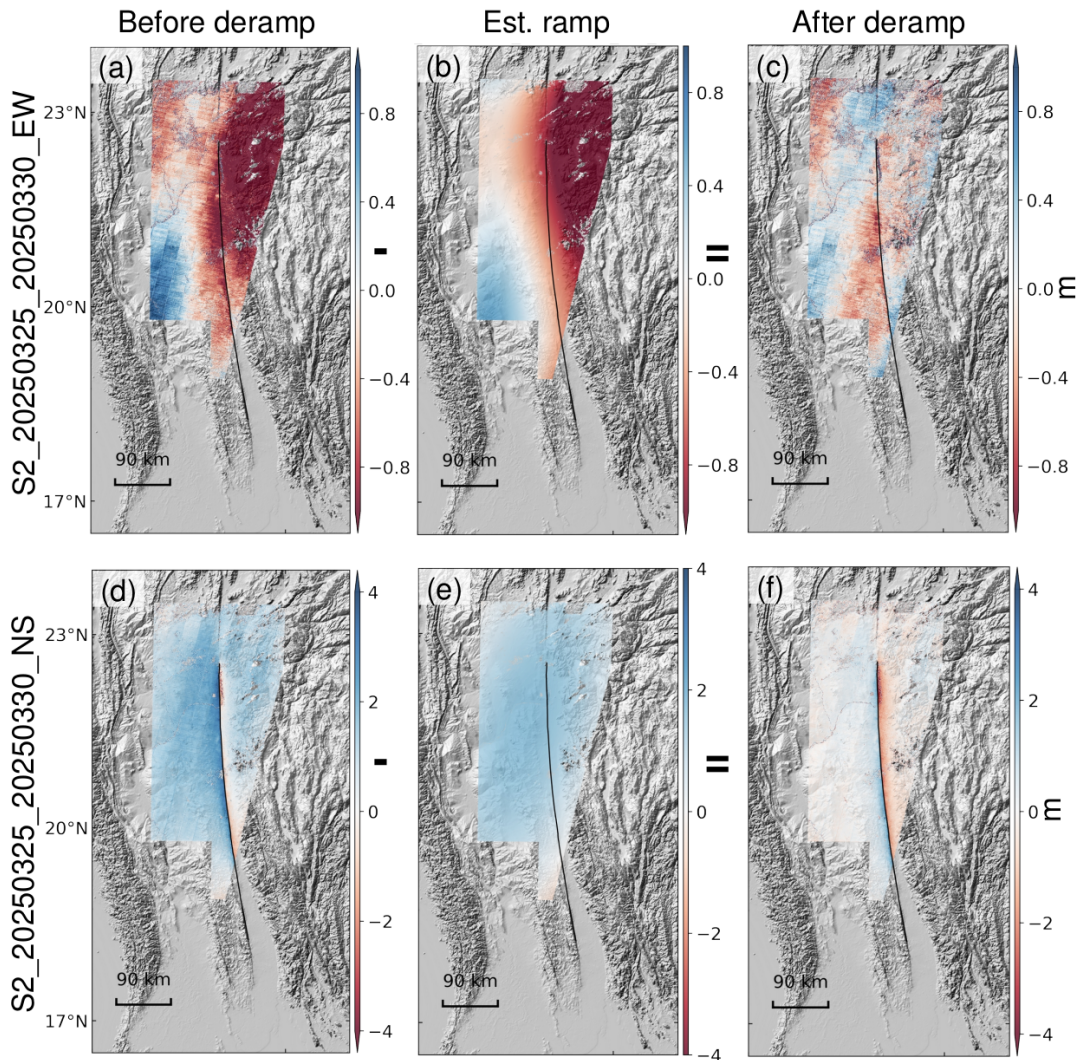


Fig. S39. Phase corrections of ALOS-2 ScanSAR interferograms. (a) ALOS-2 ascending track 152 interferogram from two SLCs acquired between 2025-02-11 and 2025-04-08. (b) Ionospheric delay estimated using the split-spectrum technique. (c) Tropospheric delay estimated from the ERA5 global atmospheric model. (d) Solid Earth tides estimated based on the IERS 2010 convention. (e-f) Estimated displacement after correcting (a) for ionosphere, troposphere and solid Earth tides in (e) wrapped and (f) unwrapped phase, respectively. (g-h) Spatial coherence and amplitude of the interferogram, respectively. (i-q) Same as (a-h) but for the ALOS-2 descending track 41 interferogram from two SLCs acquired between 2025-02-16 and 2025-03-30. Note that the low coherence strikes along the range direction in the spatial coherence and co-located bright strikes in the interferogram amplitude are artifacts from the radio frequency interference, with probable sources on the ground from the ongoing Myanmar civil war.



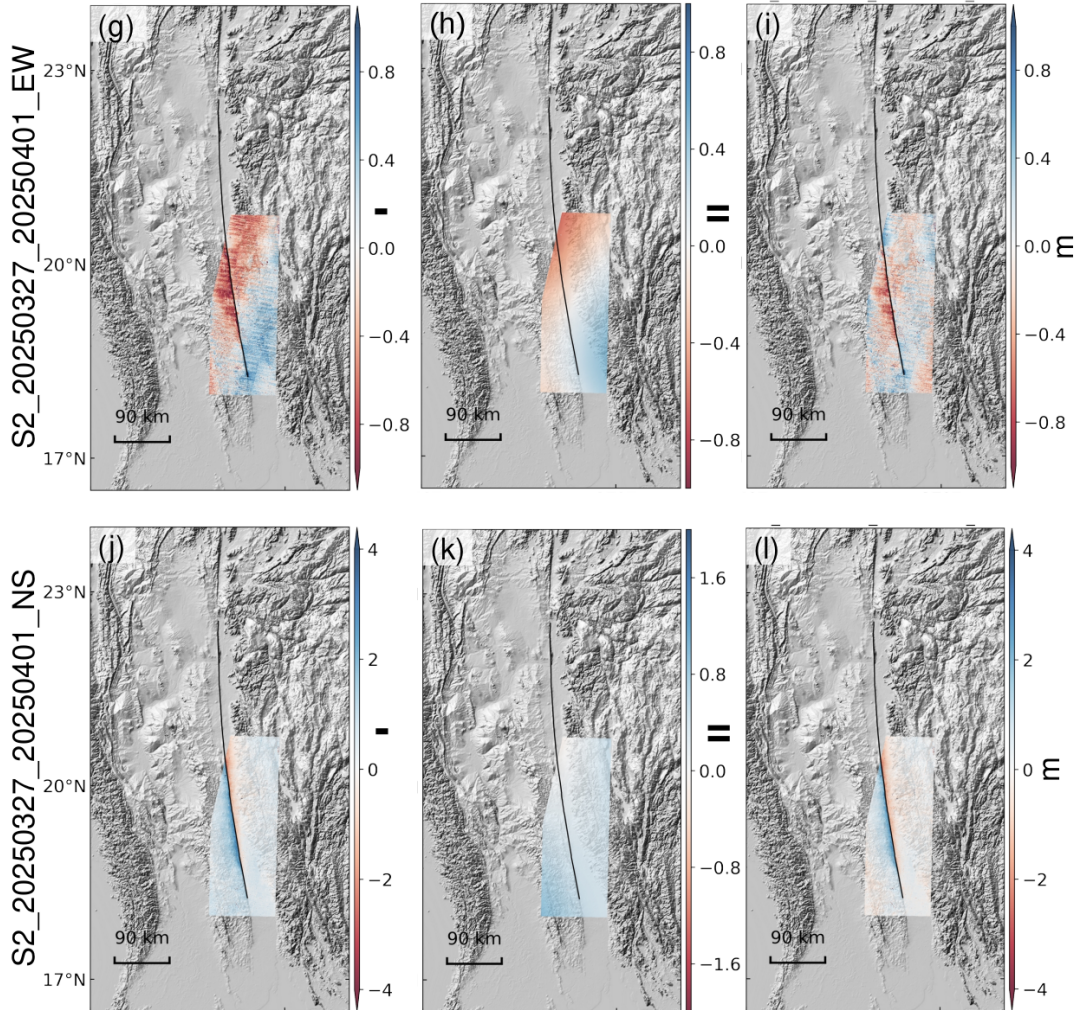


Fig. S40. The impact of ramps on Sentinel-2 dense offsets from cross-correlation. (a) The east-west offsets acquired between 2025-03-25 and 2025-03-30. (b) The estimated quadratic ramp based on (a) far-field observations. (c) Offset after deramping by subtracting (b) from (a). (d-f) Same as (a-c) but for north-south offsets. (g-l) Same as (a-f) but for the east-west and north-south offsets acquired between 2025-03-27 and 2025-04-01. Due to the strong artefacts observed in the east-west offset, we only use the north-south offset for the 3D deformation estimation and joint finite fault inversion.

Table S1. The velocity (Vs) models used in the joint finite fault inversion, adapted from (5).

(a) Vs model used to compute Green's functions for teleseismic broadband P and SH waves, as well as for local strong-motion stations NPW, NGU, and YGN (fig. S22). This Vs model is also adopted in the calculation of Green's functions for static ground deformation.

Depth range (km)	Vp (km/s)	Vs (km/s)	Density (10^3 km/m 3)
0 - 3	4.15	2.42	2.48
3 - 6	4.88	2.90	2.59
6 - 13	5.60	3.31	2.68
13 - 18	5.96	3.50	2.72
18 - 23	6.56	3.81	2.85
23 - 28	6.98	4.02	2.96
28 - 33	7.92	4.51	3.26
33 - 63	8.21	4.67	3.37

(b) Vs model used to compute Green's functions for local strong-motion stations CHTO and KTN (fig. S22).

Depth range (km)	Vp (km/s)	Vs (km/s)	Density (10^3 km/m 3)
0 - 7	5.70	3.36	2.69
7 - 11	6.44	3.75	2.82
11 - 15	6.49	3.77	2.83
15 - 25	5.72	3.37	2.69
25 - 30	5.96	3.50	2.71
30 - 35	7.34	4.21	3.07
35 - 40	8.09	4.60	3.32
40 - 90	8.15	4.63	3.35

Table S2. The empirical Green's Function event used in synthetic BP (EGF 1) and Mach wave searching (EGF 2).

EGF index	Time (UTC)	Mw	Latitude	Longitude	Depth (km)
EGF 1	2023-05-31 11:20:14	5.9	25.105°N	96.232°E	10.0
EGF 2	2025-05-17 15:54:47	5.1	21.420°N	96.056°E	10.0

Table S3. Historical magnitude 7 earthquakes along the Sagaing Fault in the 20th century (2).

Index in Fig. 1A	Year	Magnitude
1	1931	7.6
2	1946	7.3
3	1946	7.7
4	1956	7.1
5	1929	7.0
6	1930	7.3
7	1930	7.2

Table S4. The coordinates of the aftershocks used to calibrate the BP results. The time and coordinates of the aftershocks from the NEIC catalog are shown on the left (accessed on April 1, 2025). The results of the aftershock locations before and after slowness calibration are shown along with their distance errors and root-mean-square error relative to the location in the NEIC catalog. (a) shows the results of the AK array BP, (b) shows the results of the AU array BP, and (c) shows the results of the EU array BP.

(a) AK array BP.

The NEIC catalog			Before calibration			After calibration		
Time	Lat	Lon	Lat	Lon	Distance error (km)	Lat	Lon	Distance error (km)
2025-03-30 07:08:01	22.2	95.94	22.14	95.96	6.98	22.21	95.95	1.52

2025-03-28 07:27:47	22.72	95.86	22.6	95.87	13.38	22.7	95.87	2.45
2025-03-28 07:36:58	22.75	95.88	22.6	95.91	16.96	22.74	95.91	3.27
2025-03-28 16:46:21	20.22	96.14	20.44	96.02	27.48	20.28	96.06	10.68
2025-03-29 09:20:48	19.62	96.01	19.75	96.21	25.44	19.52	96.17	20.12
RMS error (km)					19.58			10.37

(b) AU array BP.

The NEIC catalog			Before calibration			After calibration		
Time	Lat	Lon	Lat	Lon	Distance error (km)	Lat	Lon	Distance error (km)
2025-03-28 12:21:56	22.01	95.97	22.05	95.96	4.57	22.01	95.96	1.03
2025-03-30 07:08:01	22.2	95.94	22.29	95.94	10.01	22.23	95.96	3.92
2025-03-28 07:27:47	22.72	95.86	22.74	95.99	13.52	22.71	95.93	7.27
2025-03-28 07:36:58	22.75	95.88	22.8	95.94	8.29	22.76	95.91	3.27
2025-03-28 16:46:21	20.22	96.14	20.38	95.94	27.41	20.22	95.99	15.65
2025-03-29 09:20:48	19.62	96.01	19.82	96.06	22.85	19.65	96.04	4.58
RMS error (km)					16.56			7.59

(c) EU array BP.

The NEIC catalog			Before calibration			After calibration		
Time	Lat	Lon	Lat	Lon	Distance error (km)	Lat	Lon	Distance error (km)
2025-03-30 07:08:01	22.2	95.94	22.14	95.95	6.75	22.11	95.95	10.06
2025-03-29 09:20:48	19.62	96.01	20.05	96.06	48.09	19.68	96.06	8.48
2025-03-28 06:45:45	19.3	96.29	19.58	96.02	42.08	19.19	96.1	23.39
2018-01-11 18:26:24	18.36	96.08	18.82	96.02	51.53	18.26	96.1	11.31
2018-04-20 22:29:24	18.32	96.16	18.76	96.09	49.47	18.2	96.17	13.38
2012-11-11 01:12:39	22.89	95.85	22.9	95.91	6.2459	22.9	95.87	2.33
2013-09-20 12:24:47	22.91	95.92	22.87	95.91	4.56	22.9	95.91	1.51
2021-07-29 08:39:27	22.88	96.02	22.87	96.06	4.24	22.84	96.02	4.44
RMS error (km)					34.11			11.48

Table S5. The coordinates of the aftershocks used to validate the BP calibration (12). The time and coordinates of the aftershocks from the NEIC catalog are shown on the left (accessed on July 23, 2025). The results of the aftershock locations before and after slowness calibration are shown along with their distance errors and root-mean-square error relative to the location in the NEIC catalog. (a) shows the results of the AK array BP, (b) shows the results of the AU array BP, and (c) shows the results of the EU array BP.

(a) AK array BP.

The NEIC catalog			Before calibration			After calibration		
Time	Lat	Lon	Lat	Lon	Distance error (km)	Lat	Lon	Distance error (km)
2025-07-18 9:30:03	22.69	96.02	22.44	95.91	30.01	22.54	95.91	20.14
2025-05-17 15:54:47	21.40	96.03	21.44	95.95	9.40	21.41	95.98	5.29
2025-04-13 2:24:57	21.19	96.05	21.27	96.10	10.30	21.21	96.02	3.82
2025-04-28 1:27:59	19.34	96.12	19.55	96.10	23.44	19.35	96.13	1.53
RMS error (km)					20.28			10.61

(b) AU array BP.

The NEIC catalog			Before calibration			After calibration		
Time	Lat	Lon	Lat	Lon	Distance error (km)	Lat	Lon	Distance error (km)
2025-07-18 9:30:03	22.69	96.02	22.74	95.98	6.91	22.69	95.96	6.16
2025-05-17 15:54:47	21.40	96.03	21.56	95.96	19.21	21.44	95.99	6.08
2025-04-13 2:24:57	21.19	96.05	21.41	95.89	29.55	21.28	95.99	11.78

RMS error (km)	20.74		8.44
----------------	-------	--	------

(c) EU array BP.

The NEIC catalog			Before calibration			After calibration		
Time	Lat	Lon	Lat	Lon	Distance error (km)	Lat	Lon	Distance error (km)
2025-07-18 9:30:03	22.69	96.02	22.64	96.05	6.36	22.64	96.02	5.56
2025-05-17 15:54:47	21.40	96.03	21.57	95.91	22.62	21.48	95.98	10.29
2025-04-13 2:24:57	21.19	96.05	21.38	95.95	23.53	21.21	96.06	2.45
2025-04-28 1:27:59	19.34	96.12	19.52	96.25	24.22	19.29	96.13	5.66
RMS error (km)					20.57			6.61

Table S6. Synthetic Aperture Radar (SAR) and optical satellite image pairs analyzed.

Sensor (band)	Mode	Pass	Track	Preseismic Date	Postseismic Date	Analyze Method
Sentinel-1 (C-band)	TOPS	Asc	070	2025-03-22	2025-04-03	Speckle tracking
	TOPS	Asc	143	2025-03-27	2025-04-08	Speckle tracking
	TOPS	Dsc	033	2025-03-19	2025-03-31	Speckle tracking
	TOPS	Dsc	106	2025-03-24	2025-04-05	Speckle tracking
LuTan-1 (L-band)	Stripmap	Asc	052	2024-08-06	2025-03-30	Speckle tracking
ALOS-2 (L-band)	ScanSAR	Asc	152	2025-02-11	2025-04-08	InSAR
	ScanSAR	Dsc	041	2025-02-16	2025-03-30	InSAR
Sentinel-2	/	/	/	2025-03-27	2025-04-01	Cross correlation
	/	/	/	2025-03-25	2025-03-30	Cross correlation

Captions for Supplementary Movies

Movie S1. The rupture process resolved by SEBP using the AK array. The white star denotes the epicenter of the mainshock.

Movie S2. The rupture process resolved by SEBP using the AU array. The white star denotes the epicenter of the mainshock.

Movie S3. The rupture process resolved by SEBP using the EU array. The white star denotes the epicenter of the mainshock.

Movie S4. The snapshot showing the rupture propagation resolved by joint FFI.

References and Notes

1. P. Bird, An updated digital model of plate boundaries. *Geochem. Geophys. Geosyst.* **4**, 2001GC000252 (2003). [doi:10.1029/2001GC000252](https://doi.org/10.1029/2001GC000252)
2. Y. Wang, K. Sieh, S. T. Tun, K.-Y. Lai, T. Myint, Active tectonics and earthquake potential of the Myanmar region. *J. Geophys. Res. Solid Earth* **119**, 3767–3822 (2014). [doi:10.1002/2013JB010762](https://doi.org/10.1002/2013JB010762)
3. G. Bertrand, C. Rangin, R. Maury, H. Htun, H. Bellon, J.-P. Guillaud, The Singu basalts (Myanmar): New constraints for the amount of recent offset on the Sagaing Fault. *C. R. Acad. Sci. II* **7**, 479–484 (1998).
4. C. Vigny, A. Socquet, C. Rangin, N. Chamot-Rooke, M. Pubellier, M.-N. Bouin, G. Bertrand, M. Becker, Present-day crustal deformation around Sagaing fault, Myanmar. *J. Geophys. Res.* **108** (B11), 2002JB001999 (2003). [doi:10.1029/2002JB001999](https://doi.org/10.1029/2002JB001999)
5. X. Wang, S. Wei, Y. Wang, P. Maung Maung, J. Hubbard, P. Banerjee, B.-S. Huang, K. Moe Oo, T. Bodin, A. Foster, R. Almeida, A 3-D shear wave velocity model for Myanmar region. *J. Geophys. Res. Solid Earth* **124**, 504–526 (2019). [doi:10.1029/2018JB016622](https://doi.org/10.1029/2018JB016622)
6. Z. Peng, X. Lei, D. Wang, X. Si, P. Mach, Q. Zhong, C. Ding, Y. Deng, M. Qin, S. Miao, Mainshock rupture properties, aftershock activities and remotely triggered seismicity associated with the 2025 Mw 7.7 Sagaing Fault earthquake in Myanmar. *EarthArXiv* X5BQ7D (2025); <https://doi.org/10.31223/X5BQ7D>.
7. L. Meng, A. Zhang, Y. Yagi, Improving back projection imaging with a novel physics-based aftershock calibration approach: A case study of the 2015 Gorkha earthquake. *Geophys. Res. Lett.* **43**, 628–636 (2016). [doi:10.1002/2015GL067034](https://doi.org/10.1002/2015GL067034)
8. C. Ji, D. J. Wald, D. V. Helmberger, Source description of the 1999 Hector Mine, California, Earthquake, Part I: Wavelet domain inversion theory and resolution analysis. *Bull. Seismol. Soc. Am.* **92**, 1192–1207 (2002). [doi:10.1785/0120000916](https://doi.org/10.1785/0120000916)
9. G. Shao, X. Li, C. Ji, T. Maeda, Focal mechanism and slip history of the 2011 Mw 9.1 off the Pacific coast of Tohoku Earthquake, constrained with teleseismic body and surface waves. *Earth Planets Space* **63**, 559–564 (2011). [doi:10.5047/eps.2011.06.028](https://doi.org/10.5047/eps.2011.06.028)
10. S.-H. Yun, K. Hudnut, S. Owen, F. Webb, M. Simons, P. Sacco, E. Gurrola, G. Manipon, C. Liang, E. Fielding, P. Milillo, H. Hua, A. Coletta, Rapid damage mapping for the 2015 Mw 7.8 Gorkha earthquake using synthetic aperture radar data from COSMO–SkyMed and ALOS-2 satellites. *Seismol. Res. Lett.* **86**, 1549–1556 (2015). [doi:10.1785/0220150152](https://doi.org/10.1785/0220150152)
11. Z. E. Ross, B. Idini, Z. Jia, O. L. Stephenson, M. Zhong, X. Wang, Z. Zhan, M. Simons, E. J. Fielding, S.-H. Yun, E. Hauksson, A. W. Moore, Z. Liu, J. Jung, Hierarchical interlocked orthogonal faulting in the 2019 Ridgecrest earthquake sequence. *Science* **366**, 346–351 (2019). [doi:10.1126/science.aaz0109](https://doi.org/10.1126/science.aaz0109) [Medline](#)
12. Materials and methods are available as supplementary materials.
13. L. Xu, Z. Yunjun, C. Ji, L. Meng, E. J. Fielding, R. Zinke, H. Bao, Understanding the rupture kinematics and slip model of the 2021 Mw 7.4 Maduo earthquake: A bilateral event on

bifurcating faults. *J. Geophys. Res. Solid Earth* **128**, e2022JB025936 (2023).
[doi:10.1029/2022JB025936](https://doi.org/10.1029/2022JB025936)

14. D. Melgar, G. P. Hayes, Systematic observations of the slip pulse properties of large earthquake ruptures. *Geophys. Res. Lett.* **44**, 9691–9698 (2017). [doi:10.1002/2017GL074916](https://doi.org/10.1002/2017GL074916)
15. D. Wang, J. Mori, K. Koketsu, Fast rupture propagation for large strike-slip earthquakes. *Earth Planet. Sci. Lett.* **440**, 115–126 (2016). [doi:10.1016/j.epsl.2016.02.022](https://doi.org/10.1016/j.epsl.2016.02.022)
16. L. Ye, T. Lay, K. D. Koper, R. Smalley Jr., L. Rivera, M. G. Bevis, A. F. Zakrajsek, F. N. Teferle, Complementary slip distributions of the August 4, 2003 Mw 7.6 and November 17, 2013 Mw 7.8 South Scotia ridge earthquakes. *Earth Planet. Sci. Lett.* **401**, 215–226 (2014). [doi:10.1016/j.epsl.2014.06.007](https://doi.org/10.1016/j.epsl.2014.06.007)
17. L. Xu, S. Mohanna, L. Meng, C. Ji, J.-P. Ampuero, Z. Yunjun, M. Hasnain, R. Chu, C. Liang, The overall-subshear and multi-segment rupture of the 2023 Mw7.8 Kahramanmaraş, Turkey earthquake in millennia supercycle. *Commun. Earth Environ.* **4**, 379 (2023). [doi:10.1038/s43247-023-01030-x](https://doi.org/10.1038/s43247-023-01030-x)
18. L. T. Aung, S. Wei, S. T. Tun, S. Min, I. M. Watkinson, W. S. B. M. Fadil, L. Feng, S. N. Khaing, M. Thant, T. Aung, P. S. Aung, I. Hermawan, A. J. Meltzner, “The 2012 Mw 6.8 Thabeikkyin earthquake in central Myanmar: A widely felt strong event with unilateral rupture through the Singu basalt on the Sagaing fault.” AGU Fall Meeting, 12 to 16 December 2022, Chicago, IL (AGU, 2022).
19. Y. Yang, C. Xie, B. Tian, Y. Guo, Y. Zhu, S. Bian, Y. Yang, M. Zhang, Y. Ruan, Advanced post-earthquake building damage assessment: SAR coherence time matrix with Vision Transformer. *Int. J. Appl. Earth Obs. Geoinf.* **133**, 104133 (2024).
[doi:10.1016/j.jag.2024.104133](https://doi.org/10.1016/j.jag.2024.104133)
20. S. Xu, J. Dimasaka, D. J. Wald, H. Y. Noh, Seismic multi-hazard and impact estimation via causal inference from satellite imagery. *Nat. Commun.* **13**, 7793 (2022).
[doi:10.1038/s41467-022-35418-8](https://doi.org/10.1038/s41467-022-35418-8) [Medline](#)
21. M. Vallée, E. M. Dunham, Observation of far-field Mach waves generated by the 2001 Koxili supershear earthquake. *Geophys. Res. Lett.* **39**, L05311 (2012).
[doi:10.1029/2011GL050725](https://doi.org/10.1029/2011GL050725)
22. H. Bao, J.-P. Ampuero, L. Meng, E. J. Fielding, C. Liang, C. W. D. Milliner, T. Feng, H. Huang, Early and persistent supershear rupture of the 2018 magnitude 7.5 Palu earthquake. *Nat. Geosci.* **12**, 200–205 (2019). [doi:10.1038/s41561-018-0297-z](https://doi.org/10.1038/s41561-018-0297-z)
23. M. Mello, H. S. Bhat, A. J. Rosakis, Spatiotemporal properties of Sub-Rayleigh and supershear rupture velocity fields: Theory and experiments. *J. Mech. Phys. Solids* **93**, 153–181 (2016). [doi:10.1016/j.jmps.2016.02.031](https://doi.org/10.1016/j.jmps.2016.02.031)
24. V. Rubino, A. J. Rosakis, N. Lapusta, Spatiotemporal properties of sub-Rayleigh and supershear ruptures inferred from full-field dynamic imaging of laboratory experiments. *J. Geophys. Res. Solid Earth* **125**, e2019JB018922 (2020). [doi:10.1029/2019JB018922](https://doi.org/10.1029/2019JB018922)
25. E. M. Dunham, R. J. Archuleta, Evidence for a supershear transient during the 2002 Denali fault earthquake. *Bull. Seismol. Soc. Am.* **94** (6B), S256–S268 (2004).
[doi:10.1785/0120040616](https://doi.org/10.1785/0120040616)

26. H. Bao, L. Xu, L. Meng, J.-P. Ampuero, L. Gao, H. Zhang, Global frequency of oceanic and continental supershear earthquakes. *Nat. Geosci.* **15**, 942–949 (2022). [doi:10.1038/s41561-022-01055-5](https://doi.org/10.1038/s41561-022-01055-5)
27. M. Abdelmeguid, C. Zhao, E. Yalcinkaya, G. Gazetas, A. Elbanna, A. Rosakis, Dynamics of episodic supershear in the 2023 M7.8 Kahramanmaraş/Pazarcık earthquake, revealed by near-field records and computational modeling. *Commun. Earth Environ.* **4**, 456 (2023). [doi:10.1038/s43247-023-01131-7](https://doi.org/10.1038/s43247-023-01131-7)
28. C. Ren, Z. Wang, T. Taymaz, N. Hu, H. Luo, Z. Zhao, H. Yue, X. Song, Z. Shen, H. Xu, J. Geng, W. Zhang, T. Wang, Z. Ge, T. S. Irmak, C. Erman, Y. Zhou, Z. Li, H. Xu, B. Cao, H. Ding, Supershear triggering and cascading fault ruptures of the 2023 Kahramanmaraş, Türkiye, earthquake doublet. *Science* **383**, 305–311 (2024). [doi:10.1126/science.adl1519](https://doi.org/10.1126/science.adl1519) [Medline](#)
29. A. Rosakis, M. Abdelmeguid, A. Elbanna, Near-field evidence for early supershear rupture of the Mw 7.8 Kahramanmaraş earthquake in Turkey. *Nat. Geosci.* **18**, 534–541 (2025). [doi:10.1038/s41561-025-01707-2](https://doi.org/10.1038/s41561-025-01707-2)
30. D. M. Boore, Effect of baseline corrections on displacements and response spectra for several recordings of the 1999 Chi-Chi, Taiwan, earthquake. *Bull. Seismol. Soc. Am.* **91**, 1199–1211 (2001). [doi:10.1785/0120000703](https://doi.org/10.1785/0120000703)
31. B. Delouis, M. van den Ende, J.-P. Ampuero, Kinematic rupture model of the 6 February 2023 Mw 7.8 Türkiye earthquake from a large set of near-source strong-motion records combined with GNSS offsets reveals intermittent supershear rupture. *Bull. Seismol. Soc. Am.* **114**, 726–740 (2023). [doi:10.1785/0120230077](https://doi.org/10.1785/0120230077)
32. S. Yao, H. Yang, Rupture phases reveal geometry-related rupture propagation in a natural earthquake. *Sci. Adv.* **11**, eadq0154 (2025). [doi:10.1126/sciadv.adq0154](https://doi.org/10.1126/sciadv.adq0154) [Medline](#)
33. H. Kanamori, E. E. Brodsky, The physics of earthquakes. *Rep. Prog. Phys.* **67**, 1429–1496 (2004). [doi:10.1088/0034-4885/67/8/R03](https://doi.org/10.1088/0034-4885/67/8/R03)
34. R. Burridge, Admissible speeds for plane-strain self-similar shear cracks with friction but lacking cohesion. *Geophys. J. Int.* **35**, 439–455 (1973). [doi:10.1111/j.1365-246X.1973.tb00608.x](https://doi.org/10.1111/j.1365-246X.1973.tb00608.x)
35. D. J. Andrews, Rupture velocity of plane strain shear cracks. *J. Geophys. Res.* **81**, 5679–5687 (1976). [doi:10.1029/JB081i032p05679](https://doi.org/10.1029/JB081i032p05679)
36. Y. Liu, N. Lapusta, Transition of mode II cracks from sub-Rayleigh to intersonic speeds in the presence of favorable heterogeneity. *J. Mech. Phys. Solids* **56**, 25–50 (2008). [doi:10.1016/j.jmps.2007.06.005](https://doi.org/10.1016/j.jmps.2007.06.005)
37. E. M. Dunham, P. Favreau, J. M. Carlson, A supershear transition mechanism for cracks. *Science* **299**, 1557–1559 (2003). [doi:10.1126/science.1080650](https://doi.org/10.1126/science.1080650) [Medline](#)
38. J. N. Hayek, M. Marchandon, D. Li, L. Pousse-Beltran, J. Hollingsworth, T. Li, A. A. Gabriel, Non-typical supershear rupture: Fault heterogeneity and segmentation govern unilateral supershear and cascading multi-fault rupture in the 2021 Mw 7.4 Maduo earthquake. *Geophys. Res. Lett.* **51**, e2024GL110128 (2024). [doi:10.1029/2024GL110128](https://doi.org/10.1029/2024GL110128)

39. Y. Kaneko, N. Lapusta, Supershear transition due to a free surface in 3-D simulations of spontaneous dynamic rupture on vertical strike-slip faults. *Tectonophysics* **493**, 272–284 (2010). [doi:10.1016/j.tecto.2010.06.015](https://doi.org/10.1016/j.tecto.2010.06.015)
40. L. Bruhat, Z. Fang, E. M. Dunham, Rupture complexity and the supershear transition on rough faults. *J. Geophys. Res. Solid Earth* **121**, 210–224 (2016). [doi:10.1002/2015JB012512](https://doi.org/10.1002/2015JB012512)
41. X. Ma, A. Elbanna, Dynamic rupture propagation on fault planes with explicit representation of short branches. *Earth Planet. Sci. Lett.* **523**, 115702 (2019). [doi:10.1016/j.epsl.2019.07.005](https://doi.org/10.1016/j.epsl.2019.07.005)
42. K. J. Ryan, D. D. Oglesby, Dynamically modeling fault step overs using various friction laws. *J. Geophys. Res. Solid Earth* **119**, 5814–5829 (2014). [doi:10.1002/2014JB011151](https://doi.org/10.1002/2014JB011151)
43. Y. Huang, J. P. Ampuero, D. V. Helmberger, The potential for supershear earthquakes in damaged fault zones—Theory and observations. *Earth Planet. Sci. Lett.* **433**, 109–115 (2016). [doi:10.1016/j.epsl.2015.10.046](https://doi.org/10.1016/j.epsl.2015.10.046)
44. S. Langer, L. Olsen-Kettle, D. Weatherley, Identification of supershear transition mechanisms due to material contrast at bimaterial faults. *Geophys. J. Int.* **190**, 1169–1180 (2012). [doi:10.1111/j.1365-246X.2012.05535.x](https://doi.org/10.1111/j.1365-246X.2012.05535.x)
45. H. Shlomai, J. Fineberg, The structure of slip-pulses and supershear ruptures driving slip in bimaterial friction. *Nat. Commun.* **7**, 11787 (2016). [doi:10.1038/ncomms11787](https://doi.org/10.1038/ncomms11787) [Medline](#)
46. H. Shlomai, M. Adda-Bedia, R. E. Arias, J. Fineberg, Supershear frictional ruptures along bimaterial interfaces. *J. Geophys. Res. Solid Earth* **125**, e2020JB019829 (2020). [doi:10.1029/2020JB019829](https://doi.org/10.1029/2020JB019829)
47. A. Mitchell, The Shan Plateau West of the Salween, *Geological Belts, Plate Boundaries, and Mineral Deposits in Myanmar*, A. Mitchell, Ed. (Elsevier, 2018), pp. 19–76.
48. D. Boore, Determining generic velocity and density models for crustal amplification calculations, with an update of the Boore and Joyner (1997) generic site amplification for graphic site amplification. *Bull. Seismol. Soc. Am.* **106**, 316–320 (2016). [doi:10.1785/0120150229](https://doi.org/10.1785/0120150229)
49. K. Xia, A. J. Rosakis, H. Kanamori, J. R. Rice, Laboratory earthquakes along inhomogeneous faults: Directionality and supershear. *Science* **308**, 681–684 (2005). [doi:10.1126/science.1108193](https://doi.org/10.1126/science.1108193) [Medline](#)
50. Z. Shi, Y. Ben-Zion, Dynamic rupture on a bimaterial interface governed by slip-weakening friction. *Geophys. J. Int.* **165**, 469–484 (2006). [doi:10.1111/j.1365-246X.2006.02853.x](https://doi.org/10.1111/j.1365-246X.2006.02853.x)
51. M. Abdelmeguid, A. Elbanna, Sequences of seismic and aseismic slip on bimaterial faults show dominant rupture asymmetry and potential for elevated seismic hazard. *Earth Planet. Sci. Lett.* **593**, 117648 (2022). [doi:10.1016/j.epsl.2022.117648](https://doi.org/10.1016/j.epsl.2022.117648)
52. D. J. Andrews, Y. Ben-Zion, Wrinkle-like slip pulse on a fault between different materials. *J. Geophys. Res.* **102** (B1), 553–571 (1997). [doi:10.1029/96JB02856](https://doi.org/10.1029/96JB02856)

53. K. Xia, A. J. Rosakis, H. Kanamori, Laboratory earthquakes: The sub-Rayleigh-to-supershear rupture transition. *Science* **303**, 1859–1861 (2004). [doi:10.1126/science.1094022](https://doi.org/10.1126/science.1094022) Medline
54. Z. Zhou, W. Zhu, W. Peng, H. Sun, S. Zhao, X. Fu, Influence of multi-stage volcanic events on the Late Cretaceous-Paleogene reservoirs and its geological significance in the northern Central Myanmar Basin. *J. Oceanol. Limnol.* **42**, 1074–1086 (2024). [doi:10.1007/s00343-023-3143-0](https://doi.org/10.1007/s00343-023-3143-0)
55. E. M. Dunham, J. R. Rice, Earthquake slip between dissimilar poroelastic materials. *J. Geophys. Res.* **113** (B9), 2007JB005405 (2008). [doi:10.1029/2007JB005405](https://doi.org/10.1029/2007JB005405)
56. J. Xu, H. Zhang, X. Chen, Rupture phase diagrams for a planar fault in 3-D full-space and half-space. *Geophys. J. Int.* **202**, 2194–2206 (2015). [doi:10.1093/gji/ggv284](https://doi.org/10.1093/gji/ggv284)
57. H. Weng, J. P. Ampuero, Continuum of earthquake rupture speeds enabled by oblique slip. *Nat. Geosci.* **13**, 817–821 (2020). [doi:10.1038/s41561-020-00654-4](https://doi.org/10.1038/s41561-020-00654-4)
58. M. Bouchon, H. Karabulut, M.-P. Bouin, J. Schmittbuhl, M. Vallée, R. Archuleta, S. Das, F. Renard, D. Marsan, Faulting characteristics of supershear earthquakes. *Tectonophysics* **493**, 244–253 (2010). [doi:10.1016/j.tecto.2010.06.011](https://doi.org/10.1016/j.tecto.2010.06.011)
59. C.-E. Rousseau, A. J. Rosakis, On the influence of fault bends on the growth of sub-Rayleigh and intersonic dynamic shear ruptures. *J. Geophys. Res.* **108** (B9), 2002JB002310 (2003). [doi:10.1029/2002JB002310](https://doi.org/10.1029/2002JB002310)
60. E. L. Templeton, A. Baudet, H. S. Bhat, R. Dmowska, J. R. Rice, A. J. Rosakis, C.-E. Rousseau, Finite element simulations of dynamic shear rupture experiments and dynamic path selection along kinked and branched faults. *J. Geophys. Res.* **114** (B8), 2008JB006174 (2009). [doi:10.1029/2008JB006174](https://doi.org/10.1029/2008JB006174)
61. R. Burns, piyushrpt, Z. Yunjun, B. Marfito, C. Liang, H. Fattahi, E. Fielding, Microwave Remote Sensing Laboratory, G. Manipon, S. Mirzaee, S. Staniewicz, Andy CA6JAU, V. Schut, asolarte, mzzhong, dbekaert, S. S. Sangha, Russell, G. H. X. Shiroma, L. Zhu, shitong01, hbparache, J. H. Kennedy, F. Amelung, bbuzz31/isce2: Buzzanga et al., 2023, (v2.6.3), Zenodo (2023); <https://doi.org/10.5281/zenodo.8157051>.
62. L. Xu, Z. Yunjun, Y. Yang, Y. Wang, C. Hu, Geodetic Deformation, DPM products, and source imaging results in “Bimaterial Effect and Favorable Energy Ratio Enabled Supershear Rupture in the 2025 Mandalay Quake”, Zenodo (2025); <https://doi.org/10.5281/zenodo.17113746>.
63. L. Xu, L. Meng, Codes for Slowness-Enhanced Back-Projection (SEBP), Zenodo (2024); <https://doi.org/10.5281/zenodo.12801968>.
64. U.S. Geological Survey, Earthquake Hazards Program, Advanced National Seismic System (ANSS) Comprehensive Catalog of Earthquake Events and Products: Various (2017); <https://doi.org/10.5066/F7MS3QZH>.
65. G. Ekström, M. Nettles, A. M. Dziewonski, The global CMT project 2004-2010: Centroid-moment tensors for 13,017 earthquakes. *Phys. Earth Planet. Inter.* **200-201**, 1–9 (2012). [doi:10.1016/j.pepi.2012.04.002](https://doi.org/10.1016/j.pepi.2012.04.002)

66. R. Newman, A. Clark, C. Trabant, R. Karstens, A. Hutko, R. Casey, T. Ahern, Wilber 3: A Python-Django Web Application For Acquiring Large-scale Event-oriented Seismic Data, Incorporated Research Institutions for Seismology (2013); <https://ds.iris.edu/wilber3/>.
67. A. Strollo, D. Cambaz, J. Clinton, P. Danecek, C. P. Evangelidis, A. Marmureanu, L. Ottmöller, H. Pedersen, R. Sleeman, K. Stammler, D. Armbruster, J. Bienkowski, K. Boukouras, P. L. Evans, M. Fares, C. Neagoe, S. Heimers, A. Heinloo, M. Hoffmann, P. Kaestli, V. Lauciani, J. Michalek, E. Odon Muhire, M. Ozer, L. Palangeanu, C. Pardo, J. Quinteros, M. Quintiliani, J. Antonio Jara-Salvador, J. Schaeffer, A. Schloemer, N. Triantafyllis, EIDA: The European Integrated Data Archive and Service Infrastructure within ORFEUS. *Seismol. Res. Lett.* **92**, 1788–1795 (2021). [doi:10.1785/0220200413](https://doi.org/10.1785/0220200413)
68. GEOFON Data Centre, GEOFON Seismic Network (GFZ Helmholtz Centre for Geosciences, 1993). <https://doi.org/10.14470/TR560404>.
69. M. Beyreuther, R. Barsch, L. Krischer, T. Megies, Y. Behr, J. Wassermann, ObsPy: A Python Toolbox for Seismology. *Seismol. Res. Lett.* **81**, 530–533 (2010). [doi:10.1785/gssrl.81.3.530](https://doi.org/10.1785/gssrl.81.3.530)
70. WorldPop, WorldPop Global Project Population Data; <https://hub.worldpop.org/>.
71. U.S. Geological Survey, Earthquake Hazards Program; <https://earthquake.usgs.gov/earthquakes/eventpage/us7000pn9s/ground-failure/about>.
72. Changguang Satellite, Jilin-1 Repository; <https://www.jl1mall.com/resrepo/>.
73. D. Gansu, *RSC: Comparative Analysis Data Before and After the Myanmar Earthquake on March 28, 2025* (National Tibetan Plateau / Third Pole Environment Data Center, 2025), [10.11888/RemoteSen.tpdc.302320](https://doi.org/10.11888/RemoteSen.tpdc.302320).
74. P. Wessel, W. H. F. Smith, New, improved version of generic mapping tools released. *Eos* **79**, 579 (1998). [doi:10.1029/98EO00426](https://doi.org/10.1029/98EO00426)
75. R. B. Lohman, W. D. Barnhart, Evaluation of earthquake triggering during the 2005-2008 earthquake sequence on Qeshm Island, Iran. *J. Geophys. Res. Solid Earth* **115**, 12413 (2010).
76. M. Ishii, P. M. Shearer, H. Houston, J. E. Vidale, Extent, duration and speed of the 2004 Sumatra-Andaman earthquake imaged by the Hi-Net array. *Nature* **435**, 933–936 (2005). [doi:10.1038/nature03675](https://doi.org/10.1038/nature03675) [Medline](#)
77. E. Kiser, M. Ishii, Back-projection imaging of earthquakes. *Annu. Rev. Earth Planet. Sci.* **45**, 271–299 (2017). [doi:10.1146/annurev-earth-063016-015801](https://doi.org/10.1146/annurev-earth-063016-015801)
78. L. Meng, A. Inbal, J. P. Ampuero, A window into the complexity of the dynamic rupture of the 2011 Mw 9 Tohoku-Oki earthquake. *Geophys. Res. Lett.* **38**, L00G07 (2011). [doi:10.1029/2011GL048118](https://doi.org/10.1029/2011GL048118)
79. A. Zhang, “Theories and applications of enhanced earthquake back-projection imaging. dissertation,” thesis, University of California (2019).
80. M. Ishii, High-frequency rupture properties of the Mw 9.0 off the Pacific coast of Tohoku Earthquake. *Earth Planets Space* **63**, 18 (2011). [doi:10.5047/eps.2011.07.009](https://doi.org/10.5047/eps.2011.07.009)

81. C. Ji, D. V. Helmberger, D. J. Wald, K.-F. Ma, Slip history and dynamic implications of the 1999 Chi-Chi, Taiwan, earthquake. *J. Geophys. Res.* **108** (B9), 2002JB001764 (2003). [doi:10.1029/2002JB001764](https://doi.org/10.1029/2002JB001764)
82. L. Zhu, L. A. Rivera, A note on the dynamic and static displacements from a point source in multilayered media. *Geophys. J. Int.* **148**, 619–627 (2002). [doi:10.1046/j.1365-246X.2002.01610.x](https://doi.org/10.1046/j.1365-246X.2002.01610.x)
83. T. M. Brocher, Empirical relations between elastic wave speeds and density in the Earth's crust. *Bull. Seismol. Soc. Am.* **95**, 2081–2092 (2005). [doi:10.1785/0120050077](https://doi.org/10.1785/0120050077)
84. G. H. F. Gardner, L. W. Gardner, A. R. Gregory, Formation velocity and density—The diagnostic basics for stratigraphic traps. *Geophysics* **39**, 770–780 (1974). [doi:10.1190/1.1440465](https://doi.org/10.1190/1.1440465)
85. E. H. Yoffe, The moving Griffith crack. *Lond. Edinb. Dublin Philos. Mag. J. Sci.* **42**, 739–750 (1951). [doi:10.1080/14786445108561302](https://doi.org/10.1080/14786445108561302)
86. E. Tinti, E. Fukuyama, A. Piatanesi, M. Cocco, A kinematic source-time function compatible with earthquake dynamics. *Bull. Seismol. Soc. Am.* **95**, 1211–1223 (2005). [doi:10.1785/0120040177](https://doi.org/10.1785/0120040177)
87. T. Zhou, L. Meng, A. Zhang, J.-P. Ampuero, Seismic waveform-coherence controlled by earthquake source dimensions. *J. Geophys. Res. Solid Earth* **127**, e2021JB023458 (2022). [doi:10.1029/2021JB023458](https://doi.org/10.1029/2021JB023458)
88. P. A. Rosen, E. Gurrola, G. F. Sacco, H. Zebker, The InSAR scientific computing environment, Proceedings of EUSAR 2012, 23 to 26 April 2012, Nuremberg, Germany (2012).
89. H. Fattah, P. Agram, M. Simons, A network-based enhanced spectral diversity approach for TOPS time-series analysis. *IEEE Trans. Geosci. Remote Sens.* **55**, 777–786 (2017). [doi:10.1109/TGRS.2016.2614925](https://doi.org/10.1109/TGRS.2016.2614925)
90. N. Yagüe-Martínez, P. Prats-Iraola, F. Rodríguez González, R. Brćic, R. Shau, D. Geudtner, M. Eineder, R. Bamler, Interferometric processing of Sentinel-1 TOPS data. *IEEE Trans. Geosci. Remote Sens.* **54**, 2220–2234 (2016). [doi:10.1109/TGRS.2015.2497902](https://doi.org/10.1109/TGRS.2015.2497902)
91. Z. Yunjun, H. Fattah, X. Pi, P. Rosen, M. Simons, P. Agram, Y. Aoki, Range geolocation accuracy of C-/L-band SAR and its implications for operational stack coregistration. *IEEE Trans. Geosci. Remote Sens.* **60**, 5227219 (2022). [doi:10.1109/TGRS.2022.3168509](https://doi.org/10.1109/TGRS.2022.3168509)
92. J.-H. Chong, B. Oryan, L. Shen, M. S. Steckler, E. O. Lindsey, Interseismic uplift of anticlines above the Rakhine-Bangladesh megathrust from ALOS-2 InSAR. *J. Geophys. Res. Solid Earth* **130**, e2024JB030003 (2025). [doi:10.1029/2024JB030003](https://doi.org/10.1029/2024JB030003)
93. R. Wang, K. Liu, D. Liu, N. Ou, H. Yue, Y. Chen, LuTan-1: An innovative L-band space-borne bistatic interferometric synthetic aperture radar mission. *IEEE Geosci. Remote Sens. Mag.* **13**, 58–78 (2024). [doi:10.1109/MGRS.2024.3478761](https://doi.org/10.1109/MGRS.2024.3478761)
94. H. Fattah, M. Simons, P. Agram, InSAR time-series estimation of the ionospheric phase delay: An extension of the split range-spectrum technique. *IEEE Trans. Geosci. Remote Sens.* **55**, 5984–5996 (2017). [doi:10.1109/TGRS.2017.2718566](https://doi.org/10.1109/TGRS.2017.2718566)

95. C. Liang, E. J. Fielding, Interferometry With ALOS-2 Full-Aperture ScanSAR Data. *IEEE Trans. Geosci. Remote Sens.* **55**, 2739–2750 (2017). [doi:10.1109/TGRS.2017.2653190](https://doi.org/10.1109/TGRS.2017.2653190)
96. C. W. Chen, H. A. Zebker, Two-dimensional phase unwrapping with use of statistical models for cost functions in nonlinear optimization. *J. Opt. Soc. Am. A Opt. Image Sci. Vis.* **18**, 338–351 (2001). [doi:10.1364/JOSAA.18.000338](https://doi.org/10.1364/JOSAA.18.000338) Medline
97. C. Liang, Z. Liu, E. J. Fielding, R. Bürgmann, InSAR Time Series Analysis of L-Band Wide-Swath SAR Data Acquired by ALOS-2. *IEEE Trans. Geosci. Remote Sens.* **56**, 4492–4506 (2018). [doi:10.1109/TGRS.2018.2821150](https://doi.org/10.1109/TGRS.2018.2821150)
98. H. Hersbach, B. Bell, P. Berrisford, S. Hirahara, A. Horányi, J. Muñoz-Sabater, J. Nicolas, C. Peubey, R. Radu, D. Schepers, A. Simmons, C. Soci, S. Abdalla, X. Abellan, G. Balsamo, P. Bechtold, G. Biavati, J. Bidlot, M. Bonavita, G. De Chiara, P. Dahlgren, D. Dee, M. Diamantakis, R. Dragani, J. Flemming, R. Forbes, M. Fuentes, A. Geer, L. Haimberger, S. Healy, R. J. Hogan, E. Hólm, M. Janisková, S. Keeley, P. Laloyaux, P. Lopez, C. Lupu, G. Radnoti, P. de Rosnay, I. Rozum, F. Vamborg, S. Villaume, J.-N. Thépaut, The ERA5 global reanalysis. *Q. J. R. Meteorol. Soc.* **146**, 1999–2049 (2020). [doi:10.1002/qj.3803](https://doi.org/10.1002/qj.3803)
99. R. Jolivet, R. Grandin, C. Lasserre, M. P. Doin, G. Peltzer, Systematic InSAR tropospheric phase delay corrections from global meteorological reanalysis data. *Geophys. Res. Lett.* **38**, L17311 (2011). [doi:10.1029/2011GL048757](https://doi.org/10.1029/2011GL048757)
100. G. Petit, B. Luzum, IERS Technical Note No. 36 (2010); <https://iers-conventions.obspm.fr/content/tn36.pdf>.
101. N. G. Reitman, Y. Wang, Y.-T. Kuo, C. Hanagan, A. E. Hatem, C. B. DuRoss, W. D. Barnhart, H. Z. Yin, R. W. Briggs, J. A. Thompson Jobe, S. R. Nicovich, E. M. Lynch, J. Powell, R. G. Schmitt, Remote surface rupture observations for the M7.7 2025 Mandalay, Burma (Myanmar) earthquake, USGS (2025); <https://doi.org/10.5066/P1RYMWCK>.
102. S. Aati, C. Milliner, J.-P. Avouac, A new approach for 2-D and 3-D precise measurements of ground deformation from optimized registration and correlation of optical images and ICA-based filtering of image geometry artifacts. *Remote Sens. Environ.* **277**, 113038 (2022). [doi:10.1016/j.rse.2022.113038](https://doi.org/10.1016/j.rse.2022.113038)
103. Y. Fialko, M. Simons, D. Agnew, The complete (3-D) surface displacement field in the epicentral area of the 1999 MW7.1 Hector Mine Earthquake, California, from space geodetic observations. *Geophys. Res. Lett.* **28**, 3063–3066 (2001). [doi:10.1029/2001GL013174](https://doi.org/10.1029/2001GL013174)
104. E. J. Fielding, Z. Liu, O. L. Stephenson, M. Zhong, C. Liang, A. Moore, S.-H. Yun, M. Simons, Surface Deformation Related to the 2019 Mw 7.1 and 6.4 Ridgecrest Earthquakes in California from GPS, SAR Interferometry, and SAR Pixel Offsets. *Seismol. Res. Lett.* **XX**, 1–12 (2020). [doi:10.1785/0220190302](https://doi.org/10.1785/0220190302)
105. Z. Yunjun, H. Fattahi, F. Amelung, Small Baseline InSAR Time Series Analysis: Unwrapping Error Correction and Noise Reduction. *Comput. Geosci.* **133**, 104331 (2019). [doi:10.1016/j.cageo.2019.104331](https://doi.org/10.1016/j.cageo.2019.104331)

106. G. A. Arciniegas, W. Bijker, N. Kerle, V. A. Tolpekin, Coherence- and amplitude-based analysis of seismogenic damage in Bam, Iran, using ENVISAT ASAR data. *IEEE Trans. Geosci. Remote Sens.* **45**, 1571–1581 (2007). [doi:10.1109/TGRS.2006.883149](https://doi.org/10.1109/TGRS.2006.883149)
107. H. Weng, J.-P. Ampuero, The dynamics of elongated earthquake ruptures. *J. Geophys. Res. Solid Earth* **124**, 8584–8610 (2019). [doi:10.1029/2019JB017684](https://doi.org/10.1029/2019JB017684)
108. H. Weng, The dynamics of fast and slow earthquake ruptures in viscoelastic materials. *J. Geophys. Res. Solid Earth* **130**, e2024JB030663 (2025). [doi:10.1029/2024JB030663](https://doi.org/10.1029/2024JB030663)
109. J. R. Rice, Heating and weakening of faults during earthquake slip. *J. Geophys. Res.* **111** (B5), B05311 (2006). [doi:10.1029/2005JB004006](https://doi.org/10.1029/2005JB004006)
110. R. C. Viesca, D. I. Garagash, Ubiquitous weakening of faults due to thermal pressurization. *Nat. Geosci.* **8**, 875–879 (2015). [doi:10.1038/ngeo2554](https://doi.org/10.1038/ngeo2554)
111. *Earthquakes: Radiated Energy and the Physics of Faulting*, R. Abercrombie, A. McGarr, G. Di Toro, H. Kanamori, Eds. (AGU, 2006), pp. 283–293; <https://doi.org/10.1029/170GM02>.
112. H. Weng, H. Yang, Constraining frictional properties on fault by dynamic rupture simulations and near-field observations. *J. Geophys. Res. Solid Earth* **123**, 6658–6670 (2018). [doi:10.1029/2017JB015414](https://doi.org/10.1029/2017JB015414)
113. F. Gallovič, L. Valentová, J. P. Ampuero, A. A. Gabriel, Bayesian dynamic finite-fault inversion: 1. Method and synthetic test. *J. Geophys. Res. Solid Earth* **124**, 6949–6969 (2019). [doi:10.1029/2019JB017510](https://doi.org/10.1029/2019JB017510)
114. S. Nielsen, E. Spagnuolo, M. Violay, S. Smith, G. Di Toro, A. Bistacchi, G: Fracture energy, friction and dissipation in earthquakes. *J. Seismol.* **20**, 1187–1205 (2016). [doi:10.1007/s10950-016-9560-1](https://doi.org/10.1007/s10950-016-9560-1) [Medline](#)
115. E. Tinti, M. Cocco, E. Fukuyama, A. Piatanesi, Dependence of slip weakening distance (D_c) on final slip during dynamic rupture of earthquakes. *Geophys. J. Int.* **177**, 1205–1220 (2009). [doi:10.1111/j.1365-246X.2009.04143.x](https://doi.org/10.1111/j.1365-246X.2009.04143.x)
116. D. J. Andrews, Rupture dynamics with energy loss outside the slip zone. *J. Geophys. Res.* **110** (B1), 2004JB003191 (2005). [doi:10.1029/2004JB003191](https://doi.org/10.1029/2004JB003191)
117. A. A. Gabriel, J. P. Ampuero, L. A. Dalguer, P. M. Mai, Source properties of dynamic rupture pulses with off-fault plasticity. *J. Geophys. Res. Solid Earth* **118**, 4117–4126 (2013). [doi:10.1002/jgrb.50213](https://doi.org/10.1002/jgrb.50213)
118. J.-P. Ampuero, A. M. Rubin, Earthquake nucleation on rate and state faults – Aging and slip laws. *J. Geophys. Res.* **113** (B1), 2007JB005082 (2008). [doi:10.1029/2007JB005082](https://doi.org/10.1029/2007JB005082)